

AMERICAN UNIVERSITY OF BEIRUT

SEISMIC COLLAPSE ASSESSMENT OF MID-RISE
REINFORCED CONCRETE BUILDINGS IN BEIRUT

by

AHMAD AL LABBAN

A thesis
submitted in partial fulfillment of the requirements
for the degree of Master of Engineering
to the Department of Civil & Environmental Engineering
of the Faculty of Engineering and Architecture
at the American University of Beirut

Beirut, Lebanon
September 2019

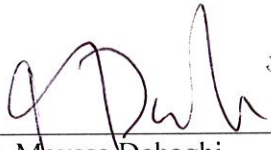
AMERICAN UNIVERSITY OF BEIRUT

SEISMIC COLLAPSE ASSESSMENT OF MID-RISE
REINFORCED CONCRETE BUILDINGS IN BEIRUT

by

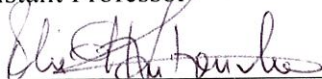
AHMAD AL LABBAN

Approved by:



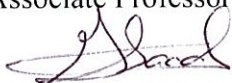
Dr. Mayssa Dabaghi,
Civil and Environmental Engineering
Assistant Professor

Advisor



Dr. Elie Hantouche,
Civil and Environmental Engineering
Associate Professor

Member of Committee



Dr. George Saad,
Civil and Environmental Engineering
Associate Professor

Member of Committee

Date of thesis/dissertation defense: September 05, 2019

AMERICAN UNIVERSITY OF BEIRUT

THESIS, DISSERTATION, PROJECT RELEASE FORM

Student Name: Al Labban Ahmad Mohamed
Last First Middle

Master's Thesis Dissertation Master's Project Doctoral


I authorize the American University of Beirut to: (a) reproduce hard or electronic copies of my thesis, dissertation, or project; (b) include such copies in the archives and digital repositories of the University; and (c) make freely available such copies to third parties for research or educational purposes.

I authorize the American University of Beirut, to: (a) reproduce hard or electronic copies of it; (b) include such copies in the archives and digital repositories of the University; and (c) make freely available such copies to third parties for research or educational purposes

after : **One ---- year from the date of submission of my thesis, dissertation, or project.**

Two years from the date of submission of my thesis, dissertation, or project.

Three ---- years from the date of submission of my thesis, dissertation, or project.

 13/11/2019
Signature Date

ACKNOWLEDGMENTS

I would like to express my sincere gratitude to my advisor Dr. Mayssa Dabaghi for her continuous support on my Master's study and related research, for her cooperation, motivation, and great knowledge she shared with me. To my committee members, Drs. Elie Hantouche and George Saad for their continuous support, advice, and insightful comments that greatly assisted the research. For Dr. Amer El Souri for his generous and continuous support and for providing his experimental data. I thank all my professors at the Faculty of Engineering at the American University of Beirut. I thank my fellow friends for the sleepless nights we worked together before deadlines, for their feedback and encouragement, and for sharing the lab with you. Finally, I would like to thank my family: my parents, my brother, and my sister, for their never-ending support and encouragement.

AN ABSTRACT OF THE THESIS OF

Ahmad Al Labban for Master of Engineering
Major: Civil Engineering

Title: Seismic collapse assessment of mid-rise reinforced concrete buildings in Beirut

Lebanon lies in an area that has been struck by several strong earthquakes and is thus classified as a region of moderate seismicity. Such large magnitude earthquakes, although rare, could result in considerable human and financial losses. Seismic regulations started being enforced in 2005, but prior to that most buildings were designed to resist gravity loads only, with little or no resistance to laterals loads. In addition, most of the construction sector suffered from poor design provisions and material quality during the Lebanese civil war (1975 – 1990). Therefore, it is important to assess the seismic performance of the buildings in Beirut and Lebanon.

The objective of this study is to quantify the probability of collapse of some representative mid-rise reinforced concrete buildings if strong shaking occurs. This is achieved by compiling information necessary to develop detailed designs of such gravity load designed buildings. Mathematical structural models are developed using Open System for Earthquake Engineering Simulation (OpenSees) and a new joint model is calibrated to fit the joint types under study. Then, the structures are subjected to a set of systematically scaled ground motions from the FEMA P695 Far Field set. After using the analysis results to fit fragility curves for each building, the probability of collapse under the maximum considered earthquake is determined.

The results of this study indicate that the building stock in Beirut has a high probability of collapse, greatly exceeding the limits set by FEMA P695. The results also indicate that joints, mainly exterior and corner ones, sustain significant damage and eventually lead to collapse. In addition, recommended locations of retrofits are proposed for each building. The results indicate the importance of spreading public awareness about the seismic vulnerability of the buildings stock in Beirut. It also constitutes an important step towards performing damage and loss analysis, enabling stakeholders and owners to choose between repairing or replacing non-ductile buildings.

CONTENTS

AKNOWLEDGMENTS.....	v
ABSTRACT.....	vi
ILLUSTRATIONS.....	x
TABLES.....	xiii

Chapter

I. INTRODUCTION AND RESEARCH OBJECTIVES.....	1
A. Motivation & Background.....	1
B. Literature Review.....	3
C. Objective & Methodology.....	7
D. Organization of Thesis.....	9
II. BUILDING DESCRIPTION AND DESIGN.....	11
A. Building Description.....	11
B. Building Design.....	12
C. Building Particularities and Seismic Deficiencies.....	17
III. STRUCTURAL MODELING.....	18
A. Structural Model Configuration.....	18
B. Frame Elements Model.....	19
1. Lumped Plastic Hinge Models.....	20
2. Shear and Axial Springs:.....	23
3. Modeling Parameters:.....	28
C. Joint Model.....	31
D. Mass and Damping:.....	33
IV. JOINT MODEL FOR WIDE BEAM-COLUMN ELEMENTS.....	36
A. Literature Review:.....	36
B. Joint Models:.....	38
1. Celik and Ellingwood:.....	38
2. De Risi, Ricci:.....	42
3. Park and Mosalam:.....	44

4. Elsouri and Harajli:	47
C. Proposed Joint Model:	49
1. Cracking:.....	50
2. Yielding:	50
3. Ultimate:	51
4. Residual:	52
5. Calibrated vs Actual Response:	53
V. NONLINEAR STRUCTURAL ANALYSIS, FRAGILITY ANALYSIS, AND COLLAPSE PERFORMANCE ASSESSMENT: METHODOLOGY	58
A. Analytical Modeling	58
B. Non-Linear Pushover Analysis	59
C. Non-Linear Incremental Dynamic Analysis	61
D. Fragility Analysis & Performance Evaluation.....	64
VI. NONLINEAR STRUCTURAL ANALYSIS, FRAGILITY ANALYSIS, AND COLLAPSE PERFORMANCE ASSESSMENT: RESULTS	68
A. Seismic Hazard at the Site	68
B. Non-Linear Analysis Results.....	69
C. Performance Evaluation with Total Uncertainty	77
D. Individual Frame Analysis.....	79
VII. DAMAGE ASSESSMENT AND RETROFITTING RECOMMENDATIONS	87
A. Collapse Mechanisms of the Studied Non-Ductile Reinforced Concrete Buildings	87
B. Retrofitting Recommendations	90
VIII. SUMMARY, CONCLUSIONS, AND RECOMMENDATIONS	94
A. Summary and Conclusions:	94
B. Limitations and Recommendation for Future Work:.....	96
BIBLIOGRAPHY	99

Appendix

A. DESCRIPTION AND DESIGN OF THE BUILDINGS	103
A. Design Assumptions:	103
1. Applied Loads:	103
2. Material Properties:.....	104
3. Design and Strength Requirements:.....	104
B. BUILDINGS MODEL PARAMETERS	107
C. STRUCTURAL ANALYSIS RESULTS	111

ILLUSTRATIONS

Figure	Page
1. Faults within Lebanon - Huijer <i>et al.</i> [1]	2
2. Ground floor plan of 8-story building (column dimensions vary in upper levels) ...	12
3. Modeling approaches for flexural and flexural-shear modes - Sattar and Liel [14].	20
4. Backbone curve of the moment rotation relation of rotational springs - Ibarra <i>et al.</i> [28].....	21
5. Determination of the degrading slope, Kdeg - Elwood [7], Sattar and Liel [14]	26
6. Joint scissors model - Alath [39]	31
7. Hysteretic pinching material - Lowes and Altoontash [42].....	32
8. Joint free body diagram for interior joint - Celik and Ellingwood [4]	39
9. Joint steel layout from database - Celik and Ellingwood [4].....	40
10. Exterior joint layout - De Risi <i>et al.</i> [5].....	43
11. Corner joints layout - Park and Mosalam [41]	46
12. Wide beam-column element configurations - Elsouiri and Harajli [3].....	48
13. Yield rotation value versus beam to column aspect ratio	51
14. Ultimate rotation versus beam to column aspect ratio.....	52
15. Exterior joint model for displacement control analysis.....	54
16. Calibrated vs actual response of Exterior Joint -Frame 1	55
17. Calibrated vs actual response of Exterior Joint -Frame 2.....	55
18. Calibrated vs actual response of Interior Joint -Frame 1	56
19. Calibrated vs actual response of Interior Joint -Frame 2	56
20. OpenSees model of the 8-story building.....	59
21. Idealized pushover curve of base shear versus roof displacement - FEMA P-695 methodology [17].....	60
22. Incremental dynamic analysis - Vamvatsikos and Cornell [18].....	63
23. Collapse fragility curve - FEMA P-695 methodology [17].....	65
24. Collapse Fragility for RTR and Total Uncertainty - FEMA P-695 methodology [17]	67

25. Pushover analysis results of 4-, 8-, and 12-story buildings	70
26. MIDA results of the 8-story building	71
27. Maximum IDR at each floor for one ground motion scaled to different intensity levels	73
28. Empirical and fitted fragility function for the 8-story building	74
29. Fitted fragility curves for the 4-, 8-, and 12-story buildings and probability of collapse (horizontal lines) under MCE spectral intensity (vertical lines).....	76
30. Fitted fragility curves under record to record (thin lines) and total uncertainty (thick lines) for the 4-, 8-, and 12-story buildings and probability of collapse accounting for total uncertainty (horizontal lines) under MCE spectral intensity (vertical lines)	78
31. Pushover analysis of the individual and combined frame models of the 8-story building: (a) un-normalized; (b) normalized by their seismic weight.	81
32. Median MIDA curves for the combined, exterior, and interior frame models of the 8-story building.....	82
33. Maximum IDR ratio for the combined, exterior, and interior frame models of the 8-story building for one ground motion at the exterior frame collapse $S_a(T)=0.3g$	84
34. Fitted collapse fragility curves for the exterior, interior, and combined frames	86
35. Damage Patterns in the 4-story building at collapse – Yield (Blue) & Ultimate (Red)	88
36. Damage patterns in the 8-story building at collapse – Yield (Blue) & Ultimate (Red)	89
37. Damage patterns in the 12-story building at collapse – Yield (Blue) & Ultimate (Red)	90
38. Recommended jacketing locations for the 4-story building	91
39. Recommended jacketing locations for the 8-story building	92
40. Recommended jacketing locations for the 12-story building	93
41. MIDA results of the 4-story building	111
42. MIDA results of the 8-story exterior frame	112
43. MIDA results of the 8-story interior frame.....	112

44. MIDA results of the 12-story building	113
45. Empirical and fitted fragility function for the 4-story building	113
46. Empirical and fitted fragility function for the 8-story exterior frame.....	114
47. Empirical and fitted fragility function for the 8-story interior frame	114
48. Empirical and fitted fragility function for the 12-story building	115

TABLES

Table	Page
1. Column reinforcement for the exterior frame of the 8-story building	15
2. Column reinforcement for the interior frame of the 8-story building.....	15
3. Exterior beam reinforcement for all buildings.....	16
4. Interior beam reinforcement for all buildings.....	17
5. 8-Story building exterior frame column modeling parameters.....	28
6. 8-Story building interior frame column modeling parameters	29
7. Exterior beams modeling parameters	29
8. Interior beams modeling parameters.....	30
9. Equations to convert joint shear stress to moment and strain to rotation	38
10. Joint model parameters - Celik and Ellingwood [4]	41
11. Exterior joint model parameters - De Risi <i>et al.</i> [5]	44
12. Joint model parameters -Park and Mosalam [41]	47
13. Experimental joint rotation results - Elsouri and Harajli [3]	49
14. Proposed joint model rotation parameters	53
15. Proposed joint model moments.....	53
16. Proposed hysteric pinching parameters	54
17. Building height, fundamental periods, spectral intensity at MCE earthquake, and seismic weight.....	68
18. Pushover analysis parameters of all buildings.....	69
19. Fitted fragility curves parameters for the 4-, 8-, and 12-story buildings	74
20. MCE spectral intensity, fitted median and standard deviation, and collapse probability at MCE for the record to record (RTR) and total (TOT) uncertainty for the 4-, 8-, and 12-story buildings.....	76
21. Pushover analysis parameters of individual and combined frame models of the 8- story building.....	80

22. MCE spectral intensity, fitted median and standard deviation, and collapse probability for the record to record (RTR) and total (TOT) uncertainty for combined and individual frames.....	84
23. Column Reinforcement for the 4-Story Building	103
24. Column Reinforcement for the 12-Story Building	104
25. 4-Story Building Exterior Frame Column Modeling Parameters	106
26. 4-Story Building Interior Frame Column Modeling Parameters	106
27. 12-Story Building Exterior Frame Column Modeling Parameters	107
28. 12-Story Building Interior Frame Column Modeling Parameters	107

CHAPTER I

INTRODUCTION AND RESEARCH OBJECTIVES

A. Motivation & Background

In the past millennia, the Eastern Mediterranean region, which includes countries such as Lebanon, Syria, and Jordan, has been struck by several strong earthquakes. Based on historical events, earthquakes with magnitude 7 and above struck the coastal cities of Lebanon and caused large-scale destruction and high death tolls [1]. Lebanon lies over an estimated 1000 km fault system spreading from the Red Sea to the Taurus Mountains in southern Turkey. The main active faults that lie within Lebanon, as shown in Figure 1, are the Yammouneh, Rachaya, Serghaya, Roum, and the newly discovered Mount Lebanon Thrust fault. Therefore, Lebanon is classified as a seismic prone country.

Despite being an area of moderate seismicity, most of the buildings in Beirut were designed to resist gravity loads only, with little or no consideration to lateral resistance. Consequently, most of these buildings are expected to behave in a non-ductile manner when subjected to strong ground shaking. This is especially true for the structures built during the Lebanese civil war (1975-1990) when the construction industry suffered from poor design provisions and lack of material quality control [2].



Figure 1: Faults within Lebanon - Huijer *et al.* [1]

Prior to 2005, most of the buildings in Beirut were gravity load designed (GLD) without considering earthquake effects. In addition to the lack of a seismic design code, the common design and construction practices in 1970-1990 lead to structural deficiencies that are of main concern during an earthquake event [2, 3]. These deficiencies include the following:

- Slender Columns: To provide more space, columns are designed as wide elements with cross-section depth equal to 2-3 times the width such that they are hidden within the infill walls. This might lead to slender columns with early plastic hinge formation in case of severe ground shaking.
- Heavy Infill Walls: Due to the weight of infill walls, large inertia forces are created in the event of strong ground shaking. Also, these walls are usually discontinued at

the ground level, which is used for commercial shops or parking garages. Therefore, a soft-story mechanism at the ground floor is expected due to its relatively smaller stiffness compared to the upper floors.

- **Problematic Reinforcing Details:** Poor seismic performance is expected due to typical reinforcement detailing in GLD concrete frames. Such deficiencies include little or no transverse reinforcement in the beam-column joint, minimum transverse or shear reinforcement in columns, column longitudinal bars spliced directly above floor level, and beam bottom bars having short development length.
- **Plain Shear Walls:** The conventional practice in Lebanon was to build the elevator shaft and/or staircase as plain reinforced concrete walls. In case of an earthquake event, the highly rigid walls will attract most of the inertia forces. These walls are expected to fail as they are not designed to resist large lateral forces and displacement demands. This may lead to the partial or total collapse of the building. This study focuses on RC frame buildings; shear walls are not considered herein.

B. Literature Review

The performance of old reinforced concrete frames has been a topic of interest in recent years. Celik and Ellingwood [4] assessed old RC frames that are representative of buildings in the United States with a focus on joint response. Joints of such frames lack transverse reinforcements and are expected to undergo large shear deformations that will affect the seismic response. Thus, equations that relate the joint shear stress to moment and joint shear strain to rotation were derived. The proposed equations, along with experimental

data from previous literature, were used to define the backbone of the moment-rotation relation assigned to the joint spring. It was found that accounting for joint flexibility increased the roof drift but decreased the maximum inter-story drift ratio when compared to the same frame with rigid joints. However, fiber elements were used to model the frame, and no axial and shear springs were used to capture axial and shear strength degradation. De Risi *et al.* [5] assessed non-ductile reinforced concrete buildings in Italy. Experimental tests on unreinforced exterior joints were carried out and used to calibrate the parameters that define the joint model. Although lumped plastic rotational springs were used to model the structure, the model did not include axial and shear springs. Also, post-processing of the analysis results for non-simulated collapse modes was used.

Galanis and Moehle [6] assessed old RC frames that represent the buildings stock in the United States. The building designs were varied to achieve different ratios of column to beam nominal moment strength, $\Sigma M_{nc}/\Sigma M_{nb}$, and column shear demand to initial shear strength, V_p/V_n . The study indicated that the probability of collapse increases as V_p/V_n increases and decreases when $\Sigma M_{nc}/\Sigma M_{nb}$ increases. A lumped plastic hinge approach was used to model the frame elements. To capture shear and axial strength degradation, a modified version of the limit state material model proposed by Elwood [7] was used, and shear and axial springs were added when $V_p/V_n > 0.7$. However, joints were modeled as rigid. Sattar and Liel [8] assessed old concrete frames with different configurations of infill walls. Experimental testing and structural analysis were used to define and characterize the behavior of the wall using a strut and tie mechanism. Cyclic and dynamic tests of frames with infill walls showed that such frames are susceptible to shear failure. Therefore, lumped

plastic hinge models with axial and shear springs were included in all columns regardless of their V_p/V_n ratio. Also, joint flexibility was not accounted for, and joints were modeled as rigid.

Baradaran Shoraka [9] focused on the global lateral and gravity load collapse of non-ductile reinforced concrete frames. The primary mode of failure of the buildings they studied was the loss of gravity load-carrying capacity in columns. To address some of the limitations of the [7] shear limit curve model and the inability of previous models to capture the post-peak shear behavior properly, Baradaran Shoraka and Elwood [10] developed a new shear model capable of capturing pre-peak, failure, and post-peak shear response of non-ductile reinforced concrete columns. To capture the slab-column interaction and axial strength degradation after punching failure, a series of axial, shear, and moment springs were used at the slab-column interface. A lumped plasticity approach with axial and shear springs were used to model the buildings. Also, joint flexibility was included by using rotational springs.

Suwal [11] evaluated the non-linear parameters of ASCE 41-13 by comparing the response of an existing building and its mathematical model to the Northridge 1994 earthquake. The building was a seven-story structure with a perimeter frame and a flat slab. To represent both structural systems, the perimeter and the interior frames were modeled and connected by rigid links. The frames were modeled using the lumped plasticity approach and the springs were assigned ASCE 41-13 non-linear parameters. No axial and shear springs were used, and joints were considered rigid. Results indicated that the interaction between the two frames had a significant effect on the total response of the

building and hinge formation pattern. Results also indicated that ASCE 41 beam parameters are conservative and thus lead to a weak-beam strong-column behavior. As a result, the simulated damage was found to be inconsistent with the observed one.

El-Khoury and Harajli [2] assessed buildings that are representative of the building stock in Beirut. These buildings are characterized by wide beam-column frame elements. Following ACI 318-95 provisions, the buildings were designed to resist gravity loads only, without considering lateral forces. 3-dimensional linear elastic models were created using E-tabs, and only response spectrum dynamic analyses using peak ground accelerations of 0.15g, 0.2g, and 0.3g were conducted. Their study indicated that structural member sizes violate the dimensional limitations required for regions of high seismic risk. All columns satisfied flexural strength requirements, except for the edge columns under high seismic risk. Beams did not satisfy flexural strength requirements resulting in a strong-column weak-beam design. On the other hand, beams and most columns satisfied shear strength requirements.

From the above literature, models of frame buildings that are capable of capturing the flexural, shear, and axial responses of frame elements and the shear response of joints have been developed for use in seismic collapse assessment studies. However, most of these models only consider a single frame in the analysis. Moreover, none of the buildings assessed in past non-linear time-history analysis studies have wide beam-column frame elements. In fact, El-Khoury and Harajli [2] only conducted linear elastic analysis under equivalent static loads.

In this study, we assess the RC buildings already studied by El-Khoury and Harajli [2]. The novelty of this study is that buildings with wide beam-column elements, representative of the buildings in Beirut, are assessed using non-linear dynamic analysis methods. A non-linear structural model of the interior and exterior frames is created. Lumped plastic hinges along with axial and shear springs are used to model the frame elements. Joint flexibility is accounted for by using rotational springs. However, empirical joint spring models have not been developed for joints of wide beam and column elements, which are typical of the studied buildings. Therefore, new joint model parameters and predictive relations are fitted using the experimental database of unreinforced wide beam-column joints developed by Elsoury and Harajli [3]. The new relations are compared with joint models available in the literature.

C. Objective & Methodology

The aim of this study is to assess the seismic collapse performance of older mid-rise gravity-load-designed reinforced concrete frames buildings in Beirut using non-linear dynamic analysis. This is achieved by (1) compiling information necessary to develop detailed designs of such structures, (2) developing mathematical structural models, and (3) subjecting the structures to a set of systematically scaled ground motions from the FEMA P695 Far Field set and calculating the probability of collapse as a function of ground motion intensity.

The study focuses on the building stock in Beirut as it is a highly dense area. Information about the building inventory in Beirut (e.g., age, structural system, height, etc.) and about the typical design practices used in Beirut in 1970-1990 (before the introduction of seismic regulations) is obtained from Salameh *et al.* [12]'s database and from interviews with practicing construction and structural engineers. It was difficult to obtain design drawings of actual existing buildings in Beirut, and thus the hypothetical 8- and 12-story RC frame buildings studied by El-Khoury and Harajli [2] are also used in this study. El-Khoury and Harajli [2] only provide detailed design information for the ground floors of their buildings, which were designed according to the ACI 318-95 code provisions under the ultimate gravity load combination only. In this study, the same provisions are used to develop detailed designs of the upper levels of the 8- and 12-story buildings and of all the levels of a 4-story building with a similar floor plan.

For each building, a non-linear structural analysis model is created using the Open System for Earthquake Engineering Simulation (OpenSees) developed by McKenna *et al.* [13]. Following Sattar and Liel [14], global lateral or gravity collapse is assumed to be the predominant mode of failure of the frame buildings, considered when subjected to a strong seismic excitation. The model developed must be capable of adequately representing the response of the beam-column elements and their connections including strength and stiffness degradation, especially at large deformations [15]. Also, the non-linear solution algorithm must be robust enough to converge at each time-step until the collapse limit state is reached [16].

The seismic performance of the representative buildings is assessed by following a methodology similar to that proposed in FEMA [17]. Non-linear pushover analysis is used to estimate the shear strength and ductility capacity and verify the structural model. Non-linear incremental dynamic analysis (IDA), proposed by Vamvatsikos and Cornell [18], is then conducted using the FEMA P-695 Far Field ground motion set. Fragility curves that describe the probability of collapse as a function of ground motion intensity are derived from the results of the IDA by fitting a lognormal cumulative distribution function defined by the median and lognormal standard deviation. Finally, the probability of collapse at a ground motion intensity corresponding to the maximum considered earthquake (MCE) is used as criterion to assess whether or not the seismic performance of a building is acceptable.

D. Organization of Thesis

Chapter 1 in this report presents a general background of this research and includes a literature review of previous related work. Also, this chapter lays out the main objective and the methodology to be followed. Chapter 2 describes the building used in this study and the design procedure followed. Chapter 3 presents the non-linear methodology followed for numerical simulation using the OpenSees software. A new joint model fitted to the experimental results of unreinforced wide beam-column joints is presented in Chapter 4. Chapter 5 explains the methodology followed for non-linear structural analysis, fragility analysis, and collapse performance assessment. The analysis results, collapse fragility curves, and assessment results obtained are then presented and discussed in Chapter 6.

Then, Chapter 7 examines the location of damage concentration of the buildings under study and proposes some retrofitting recommendations. Finally, Chapter 8 concludes with a summary of this study and its outcomes and conclusions, and provides recommendations for future work.

CHAPTER II

BUILDING DESCRIPTION AND DESIGN

A. Building Description

As mentioned previously, the buildings assessed in this study are hypothetical 4-, 8-, and 12-story GLD RC buildings representative of structures built in Beirut in 1970-1990. They are located at a class D site in Beirut. The structural system is composed of reinforced concrete beam and column elements and of a one-way ribbed slab. The designs are based on the hypothetical building designs previously developed by El-Khoury and Harajli [2]. Following El-Khoury and Harajli [2] and the ACI 318-95 code provisions [19], and based on the information collected from Salameh *et al.* [12]'s database and from interviews with practicing engineers, the building designs are developed. The height of all floors and for all buildings is 3.2 m. Figure 2 shows the plan of the ground floor of the 8-story building. All buildings have similar plan dimensions and configuration; only columns sizes vary.

In the 1970-1990s, the typical practice in Lebanon was to conceal the columns within the infill-walls by using cross-sectional depths equal as to 2-3 times the widths. In fact, common column sizes are 20 by 50 to 80 cm, 30 by 80 to 120 cm, and 40 by 100 to 140 cm. Following this common practice, the columns of the studied buildings are narrow and have a large aspect ratio greater than or equal to 2.5 in order to hide them within infill-walls.

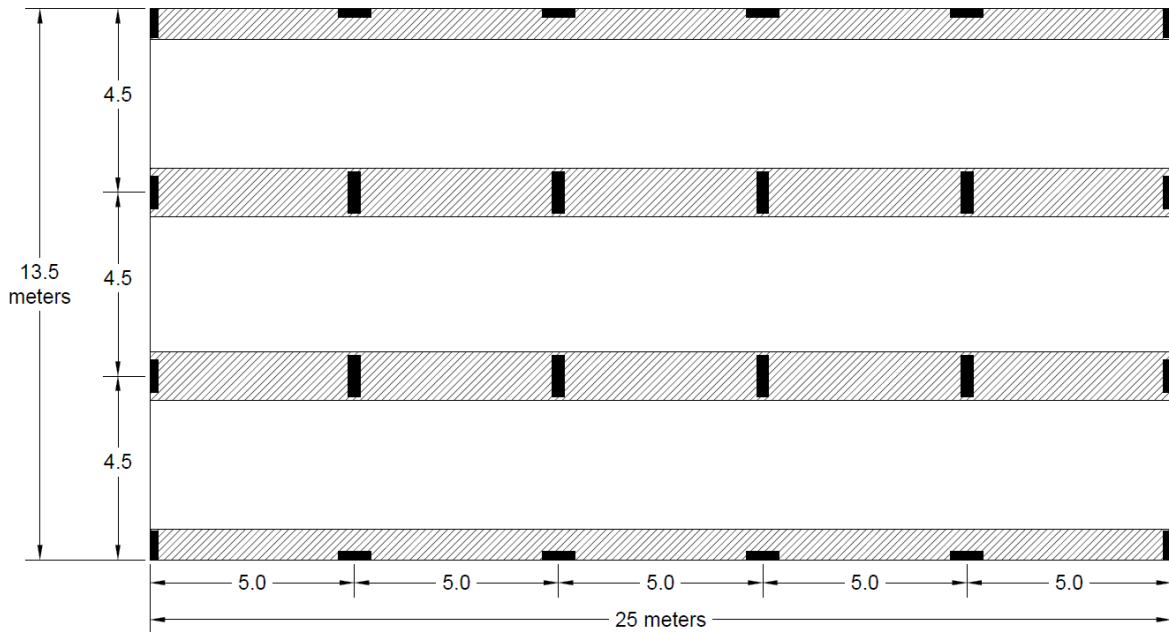


Figure 2: Ground floor plan of 8-story building (column dimensions vary in upper levels)

The beams, which span in the longitudinal direction, are wide and concealed within the slab, as shown in Figure 2. The configuration and the dimensions of the beam and column elements are taken from El-Khoury and Harajli [2]. Below the ground level, the building has basement walls acting as rigid retaining walls. The design of these walls is not considered herein.

B. Building Design

As mentioned before, the buildings are designed to resist gravity loads only, with no consideration for lateral loads. The floor system of the building consists of a 24 cm thick one-way ribbed slab that is supported by wide concealed beams [3]. The top concrete slab thickness is taken as 9 cm, and the ribs span in the short (transverse) direction with a width

of 15 cm and spacing of 55 cm [3]. The structural system also includes four reinforced concrete frames spanning in the longitudinal direction [3]. As shown in Figure 2, the buildings are symmetric in both the longitudinal and transverse directions. Material properties selected are consistent with typical construction practices in Lebanon at the time. Namely, concrete is assumed to have a nominal strength of $f'_c = 17.6 \text{ MPa}$ with a modulus of Elasticity $E_c = 19720 \text{ MPa}$, and steel is assumed to have a nominal yield stress of $f_y = 420 \text{ MPa}$.

The buildings are designed to resist the ACI 318-95 [19] ultimate load combination $1.4DL + 1.7LL$. Superimposed dead loads (SDL) and live loads (LL) are uniformly distributed over the area and determined from ACI 318-95 [19]. SDL consists of infill walls and tiling and is assigned a value of 3.5 KN/m^2 , and the weight of the slab is assumed as 4.1 KN/m^2 . The LL is selected to represent residential loading and is assigned a value of 2.0 KN/m^2 . Therefore, the ultimate load (W_u) distributed over an area is:

$$W_u = 1.4DL + 1.7LL = 14.04 \text{ KN/m}^2 \quad (1)$$

Gravity loads are assigned to the exterior and interior frames based on their tributary areas:

$$W_{u,Exterior} = W_u \times 2.25 = 31.59 \text{ KN/m},$$

$$W_{u,Interior} = W_u \times 4.5 = 63.18 \text{ KN/m}.$$

Additionally, the own weight of beams and columns is accounted for and calculated by assuming γ_c as 25 KN/m^3 . Structural analysis is then conducted to calculate the axial loads (P_u) carried by the columns.

Columns are designed to resist gravity loads only. According to ACI 318-95 [19], the nominal compressive strength (P_n) of columns with rectangular ties is:

$$P_n = 0.8[0.85f'_c(A_g - A_s) + f_y A_s] \quad (2)$$

where A_g is the gross sectional area of the column and A_s is the area of longitudinal steel reinforcement.

A minimum reinforcement ratio of 1% is used for the preliminary design and is increased to achieve the axial strength requirement of $\phi P_n \geq P_u$, where $\phi = 0.7$ is the strength reduction factor. The longitudinal reinforcement is then modified to obtain a symmetrical section. This reinforcement is spliced at each level at a distance of 50 to 60 cm above the floor level. Due to the lack of lateral forces in the analysis, minimum shear reinforcement is used in all columns. Following ACI 318-95 [19], the minimum area of shear reinforcements expressed in metric system is calculated as:

$$A_v = 0.34b_w s / f_y \quad (3)$$

where A_v is the area of shear reinforcement, b_w is the web width, and s is the spacing of shear reinforcement. Following typical Lebanese design practice at the time, column flexural strength requirements are ignored in the analysis and design procedures. Column dimensions, design axial loads, longitudinal reinforcement, and transverse reinforcement in the longitudinal direction are shown in Table 1 for the 8-story building. Similar tables for the 4- and 12-story buildings as well as drawings of typical cross-sections are presented in Appendix A.

Table 1: Column reinforcement for the exterior frame of the 8-story building

Exterior Columns of Exterior Frame							
Floor	Depth (mm)	Width (mm)	P_u (KN)	Main Reinf.	ρ (%)	Shear Reinf. (mm)	ρ_{sh} (%)
1	200	700	748	8T20	1.77	4T8@200	0.14
2	200	700	654	8T20	1.77	4T8@200	0.14
3	200	700	560	8T20	1.77	4T8@200	0.14
4	200	700	467	8T20	1.77	4T8@200	0.14
5	200	600	373	8T16	1.33	4T8@200	0.17
6	200	600	280	8T16	1.33	4T8@200	0.17
7	200	600	186	8T16	1.33	4T8@200	0.17
8	200	600	93	8T16	1.33	4T8@200	0.17
Interior Columns of Exterior Frame							
Floor	Depth (mm)	Width (mm)	P_u (KN)	Main Reinf.	ρ (%)	Shear Reinf. (mm)	ρ_{sh} (%)
1	800	200	1768	8T22	1.94	2T8@200	0.25
2	800	200	1547	8T22	1.94	2T8@200	0.25
3	800	200	1326	8T20	1.55	2T8@200	0.25
4	800	200	1104	8T20	1.55	2T8@200	0.25
5	700	200	883	8T16	1.14	2T8@200	0.25
6	700	200	662	8T16	1.14	2T8@200	0.25
7	700	200	441	8T16	1.14	2T8@200	0.25
8	700	200	221	8T16	1.14	2T8@200	0.25

Table 2: Column reinforcement for the interior frame of the 8-story building

Exterior Columns of Interior Frame							
Floor	Depth (mm)	Width (mm)	P_u (KN)	Main Reinf.	ρ (%)	Shear Reinf. (mm)	ρ_{sh} (%)
1	200	800	1768	8T22	1.94	4T8@200	0.12
2	200	800	1547	8T22	1.94	4T8@200	0.12
3	200	800	1326	8T20	1.55	4T8@200	0.12
4	200	800	1104	8T20	1.55	4T8@200	0.12
5	200	700	883	8T16	1.14	4T8@200	0.14
6	200	700	662	8T16	1.14	4T8@200	0.14
7	200	700	441	8T16	1.14	4T8@200	0.14
8	200	700	221	8T16	1.14	4T8@200	0.14
Interior Columns of Interior Frame							
Floor	Depth (mm)	Width (mm)	P_u (KN)	Main Reinf.	ρ (%)	Shear Reinf. (mm)	ρ_{sh} (%)
1	300	1000	3435	12T22	1.55	6T8@250	0.12
2	300	1000	3004	12T22	1.55	6T8@250	0.12

3	300	1000	2573	12T20	1.24	6T8@250	0.12
4	300	1000	2141	12T20	1.24	6T8@250	0.12
5	250	700	1710	8T20	1.42	4T8@200	0.11
6	250	700	1283	8T20	1.42	4T8@200	0.11
7	250	700	855	8T20	1.42	4T8@200	0.11
8	250	700	428	8T20	1.42	4T8@200	0.11

$$\rho = A_s/A_g \text{ and } \rho_{sh} = A_{sh}/bs$$

Beams and ribs are designed using ACI moment coefficients and their reinforcement is obtained from El-Khoury and Harajli [2]. Continuous longitudinal reinforcement is used throughout the beams. The necessary reinforcement is calculated at critical sections, namely at the supports and mid-span. Then, bottom bars are cut off at the supports and top bars are cutoff at mid-span. As for transverse reinforcement, minimum shear reinforcement governs; 6 mm bars with a spacing of 10 cm and 20 cm are used in the exterior and interior beams, respectively. Beam dimensions and longitudinal and transverse reinforcement for the exterior and interior beams are shown in Table 3 and Table 4, respectively. Note that the beams are identical at all levels and in all three buildings. Typical beam cross-sections are presented in Appendix A.

Table 3: Exterior beam reinforcement for all buildings

Beam Span	Dimensions (mm)	Longitudinal Reinforcement		ρ (%)		Shear Reinf. (mm)	ρ_{sh} (%)
		Top	Bottom	Top	Bot		
1	240x750	5T14	5T14	0.5	0.5	4T6@200	0.075
2	240x750	6T16	5T14	0.8	0.5	4T6@200	0.075
3	240x750	5T16	5T14	0.7	0.5	4T6@200	0.075
4	240x750	6T16	5T14	0.8	0.5	4T6@200	0.075
5	240x750	5T14	5T14	0.5	0.5	4T6@200	0.075

Table 4: Interior beam reinforcement for all buildings

Beam Span	Dimensions (mm)	Main Reinf.		ρ (%)		Shear Reinf. (mm)	ρ_{sh} (%)
		Top	Bottom	Top	Bot		
1	240x1200	5T20	8T16	0.65	0.66	4T6@100	0.093
2	240x1200	8T20	7T16	1.04	0.58	4T6@100	0.093
3	240x1200	7T20	7T16	0.91	0.58	4T6@100	0.093
4	240x1200	8T20	7T16	1.04	0.58	4T6@100	0.093
5	240x1200	5T20	8T16	0.65	0.66	4T6@100	0.093

C. Building Particularities and Seismic Deficiencies

Because the buildings are designed to resist gravity loads only and follow design and construction practices typical in Lebanon in the 1970-1990s, the buildings have seismic deficiencies that can be of main concern if strong ground shaking occurs. The seismic deficiencies of the buildings considered in this study are identified next.

First of all, the buildings lack properly designed and detailed lateral force resisting systems, such as shear walls, core walls, and/or moment-resisting frames. Consequently, the RC frames will resist all of the lateral forces in the longitudinal direction when strong ground shaking occurs. However, the beams, columns, and joints of these frames are not confined and detailed for ductile response (e.g., minimum shear reinforcement is used in the beam and column elements, there is no transverse reinforcement in the joints, the location of lap splices in columns is improper, and the development lengths for beams are short). Additionally, some of the joint dimensions do not meet current code requirements. Moreover, the materials used have relatively low strength for resisting earthquake-induced forces. Therefore, the frames are expected to have poor seismic performance.

CHAPTER III

STRUCTURAL MODELING

A. Structural Model Configuration

Structures are expected to respond in the non-linear range in the event of strong ground shaking. Since the building configurations are regular and symmetric, torsional effects on collapse capacity can be neglected [20] and each building can be represented by a planar two-dimensional (2D) model [21, 22]. In this study, 2D non-linear models of the studied structures are developed with OpenSees in the longitudinal direction only. Phenomenological (or lumped plasticity) models, which use non-linear concentrated springs to represent element force-deformation relations, are used for their ability to capture post-peak strength and stiffness degradation [23].

The interior and exterior frames have different column orientations, carry different loads, and thus are expected to have distinct responses. Consequently, both frames are modeled and connected by rigid links that represent the slab in the transverse direction [24]. Due to the rigidity of the basement walls, the columns are modeled as fixed at the ground level. The model used in this study accounts for the weight but not for the stiffness contribution of the non-structural infill walls. P-delta effects due to the effective gravity loads carried by the columns are accounted for; they are applied directly on the gravity frames.

B. Frame Elements Model

The structural model must be capable of capturing all the important modes of collapse until failure. For a concrete frame designed for ductile response, capturing the flexural response and failure is usually sufficient. However, for an old reinforced concrete frame, the lack of seismic detailing may result in column shear failure and loss of gravity load carrying capacity. While axial, shear, and flexural modes must be included in the analysis, no single model that is capable of capturing all of them exists, and thus post processing of the analysis results is required [16].

Each column is simulated as a purely flexural or flexure-shear element depending on its V_p/V_n ratio. V_p is the shear demand due to the development of column moment strength M_n [25],

$$V_p = \frac{M_{n,top} + M_{n,bot}}{L}, \quad (4)$$

where M_n is the column moment strength and L is the column length, and V_n is the initial nominal shear strength of the column calculated based on ASCE 41 [26] as follows:

$$V_n = \frac{A_v f_{yt} d}{s} + \lambda_c \left(\frac{0.5 \sqrt{f'_c}}{a/d} \right) \sqrt{\left(1 + \frac{P}{0.5 \sqrt{f'_c} A_g} \right)} 0.8 A_g \quad (MPa). \quad (5)$$

In the above equation, A_v is the area of shear reinforcement, f_{yt} is the transverse steel strength, d is the column effective depth, s is the spacing of transverse reinforcement, $\lambda_c = 1$ for normal weight concrete, f'_c is the concrete compressive strength, a is the shear span taken as $L/2$, where L is the column length, P is the axial force, A_g is the column gross section area.

1. Lumped Plastic Hinge Models

Columns with $V_p/V_n < 0.7$ and beams are assumed to be dominated by flexure and are modeled with the lumped plastic hinge approach proposed by Ibarra and Krawinkler [27]. As shown in Figure 3 (left), each element is modeled using a linear elastic element with a zero-length rotational spring at each end. The linear elastic element is assigned properties that are similar to the gross-sectional properties along with stiffness modification factors that are introduced later in this chapter.

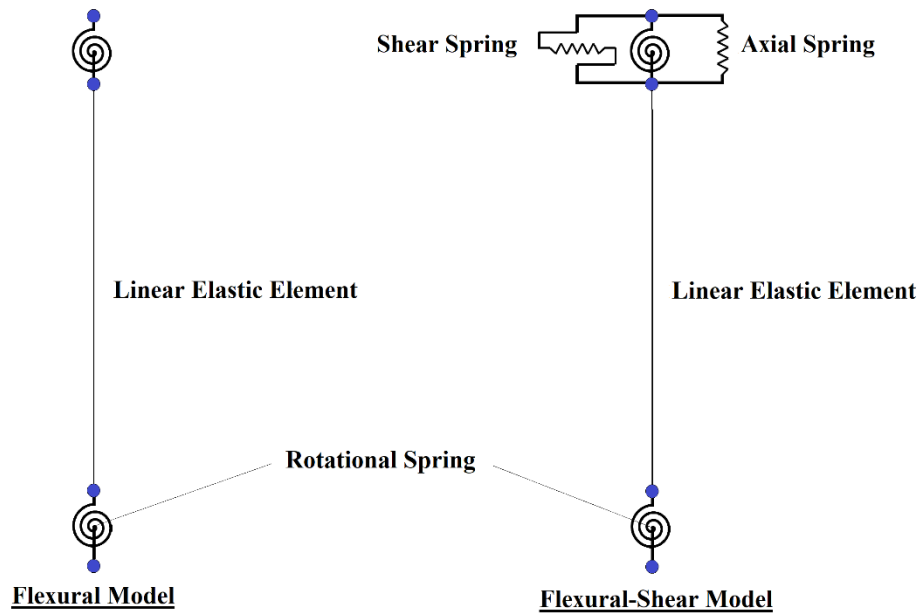


Figure 3: Modeling approaches for flexural and flexural-shear modes - Sattar and Liel [14]

The rotational springs are assigned a moment-rotation relation proposed by Ibarra *et al.* [28]. The backbone curve of this relation is shown in Figure 4 and is defined by five parameters: yield moment (M_y), capping moment (M_c), elastic stiffness ($K_s = EI_{stf}$), plastic rotational capacity ($\theta_{cap,pl}$), and post capping rotational capacity (θ_{pc}). The hysteretic response requires the definition of two additional model parameters, the

normalized energy dissipation capacity (λ) and an exponent term (c) describing how damage accumulation changes the cyclic deterioration rate.

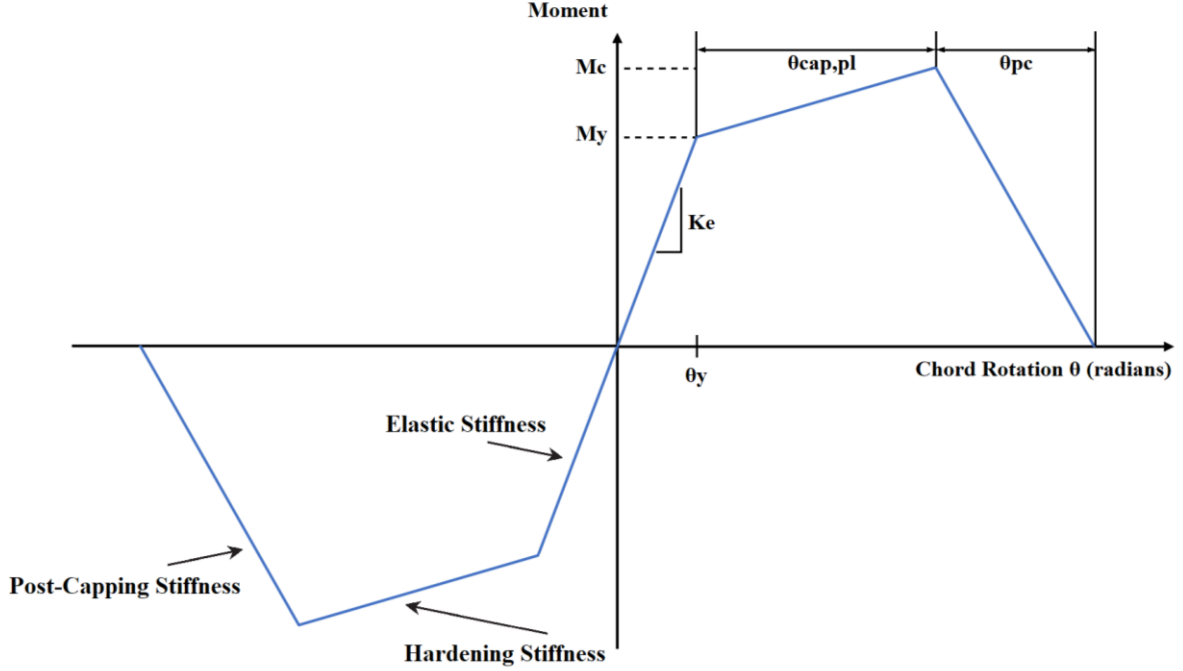


Figure 4: Backbone curve of the moment rotation relation of rotational springs - Ibarra *et al.* [28]

B. Haselton *et al.* [29] used the PEER Structural Performance Database [30], which contains hundreds of monotonic and cyclic tests of RC beam-columns, to develop empirical predictive equations for the seven model parameters as functions of several design parameters such as geometry, reinforcement details, material strength, and axial load ratio. Their proposed predictive equations are

$$\frac{EI_{stf}}{EI_g} = 0.77(0.1 + \nu)^{0.8} \left(\frac{L_s}{H}\right)^{0.43} \quad (6)$$

$$\theta_{cap,pl} = 0.12(1 + 0.55a_{sl})(0.16)^\nu(0.02 + 40\rho_{sh})^{0.43}(0.54)^{0.01c_{units}f'_c}(0.66)^{0.15s_n}(2.27)^{10.0\rho} \quad (7)$$

$$\theta_{pc} = (0.76)(0.031)^\nu(0.02 + 40\rho_{sh})^{1.02} \leq 0.10 \quad (8)$$

$$M_c/M_y = 1.13 \quad (9)$$

$$\lambda = (170.7)(0.27)^v(0.10)^{s/d} \quad (10)$$

$$c = 1.0 \quad (11)$$

where E is the modulus of elasticity of concrete, I_g is the gross moment of inertia, I_{stf} is the effective cross-sectional moment of inertia through 40% yield, $v = P/A_g f'_c$ is the axial load ratio, L_s is the shear span being the distance between element end and point of inflection, H is the height of the cross section (measured parallel to the transverse load), s is the spacing of transverse reinforcement at the hinge region, d is the effective depth of the section, ρ_{sh} is the ratio of transverse reinforcement at the hinge region, a_{sl} is assigned as 0 if slip is not possible or 1 if slip is possible, c_{units} is defined as a conversion constant being 1.0 if units are MPa and 6.9 if units are ksi , s_n is the rebar buckling coefficient given as $s/d_b \sqrt{c_{units} f_y / 100}$, and ρ is the total ratio of longitudinal reinforcement in columns and of tension reinforcement in beams. M_y is calculated using the equations proposed by Panagiotakos and Fardis [31].

The calibrated equations (6) to (11) are based on 255 columns failing in flexural or flexural-shear modes. Sattar and Liel [14] utilized the same functional forms but recalibrated these equations to only include the 220 columns failing in flexure. Since these recalibrated equations are not published, the recalibrated equations provided in Galanis [25], which are based on an earlier version of the predictive equations [32], are used in this study:

$$\theta_{cap,pl} = 0.13(1 + 0.55a_{sl})(0.16)^v(0.02 + 40\rho_{sh})^{0.55}(0.99412)^{f'_c} \quad (12)$$

$$\theta_{pc} = (1.13)(0.018)^v(0.02 + 40\rho_{sh})^{1.14} \leq 0.10 \quad (13)$$

$$\lambda = (189)(0.23)^v(0.10)^{s/d} \quad (14)$$

Thus, in this study, equations (12) to (14) are used in place of equations (7), (8) and (10).

2. Shear and Axial Springs:

Columns with $V_p/V_n > 0.7$ may fail in shear, either before or after flexural yielding. These failure modes are denoted as shear and flexure-shear modes, respectively. To capture these failure modes, such columns are modeled with the combined shear and flexure-shear model [7]. As shown in Figure 3 (right), shear and axial springs are added to the rotational spring at the top end of each column to model shear and axial strength degradation. The rotational springs are defined as in the previous section. The shear and axial springs are each defined by a bi-linear force deformation relation, with a linear elastic loading branch followed by a linear degrading branch when shear or axial failure is initiated. The initiation of shear and axial failure is captured using the limit state uniaxial material model developed by Elwood [7].

Elwood and Moehle [33] used the results of 50 tests of RC columns yielding in flexure before failing in shear to calibrate a shear limit curve that defines the displacement at which shear failure occurs. The drift ratio at shear failure Δ_s/L is predicted as a function of several factors including transverse reinforcement ratio and axial load:

$$\frac{\Delta_s}{L} = \frac{3}{100} + 4\rho'' - \frac{1}{40} \frac{v_s}{\sqrt{f'_c}} - \frac{1}{40} \frac{P}{A_g f'_c} \geq \frac{1}{100} \quad (15)$$

where ρ'' is the shear reinforcement ratio, and v_s is the nominal shear stress V/bd . This limit curve is implemented in the OpenSees uniaxial material class.

Another shear limit curve that defines the force at which shear failure occurs should be considered in addition to equation (15), to capture the brittle shear failure mode occurring before flexural yielding [6, 14]. This limit curve is based on the shear strength equation proposed by Sezen and Moehle [34]

$$VF = k \left[\frac{A_v f_{yt} d}{s} + \lambda_c \left(\frac{0.5 \sqrt{f'_c}}{a/d} \right) \sqrt{\left(1 + \frac{P}{0.5 \sqrt{f'_c} A_g} \right) 0.8 A_g} \right] (MPa), \quad (16)$$

where k is a factor that degrades with displacement ductility μ_T ; $k = 1.0$ if $\mu_T \leq 2.0$, $k = 0.7$ if $\mu_T \geq 6.0$, and is linearly interpolated for values in between. This equation however is not implemented in the OpenSees uniaxial material class and is not used herein. Work is ongoing by several researchers to improve the shear spring models and limit curves.

Figure 5 shows the force-deformation relations of the shear spring (a), the beam-column element (b), and the combined shear spring beam-column element (c). As shown in Figure 5(a), before shear failure initiates, the shear spring is assigned a linear force-deformation relation with a slope equal the shear stiffness of the un-cracked column cross-section [35]:

$$K_{shear} = \frac{G A_{ev}}{L} \quad (17)$$

where G is the shear modulus of elasticity calculated as $E/2(1 + \nu_p)$, where ν_p is the poisson ratio taken as 0.15 for concrete, A_{ev} is the effective shear area calculated as $5/6 A_g$, and L is the column length. As shown in Figure 5(c), the total column displacement response consists of contributions from both shear deformations (Figure 5(a)) and flexural deformations (Figure 5(b)). When the total column response reaches one of the predefined

shear limit curves, the backbone of the shear spring enters the degrading phase, with a slope equal to the degrading stiffness K_{deg} . As a result, the column unloads with a slope K_{deg}^t reflecting shear strength degradation.

Similarly, Elwood [7] used the limit state uniaxial material model to model axial failure, which is assumed to result from sliding along a critical shear inclined crack and thus to occur after shear failure. Elwood and Moehle [36] developed a model of the axial limit curve that defines the displacement at which the onset of axial failure occurs. The axial limit curve is defined as:

$$\left(\frac{\Delta}{L}\right)_{axial} = \frac{4}{100} \times \frac{1 + (\tan \theta)^2}{\tan \theta + P(s/A_{st}f_{yt}d_c \tan \theta)}, \quad (18)$$

where $(\Delta/L)_{axial}$ is the drift ratio at axial failure, A_{st} is the area of transverse reinforcement, f_{yt} is the transverse reinforcement yield strength, and θ is the crack angle measured from the horizontal and assumed to be 65° .

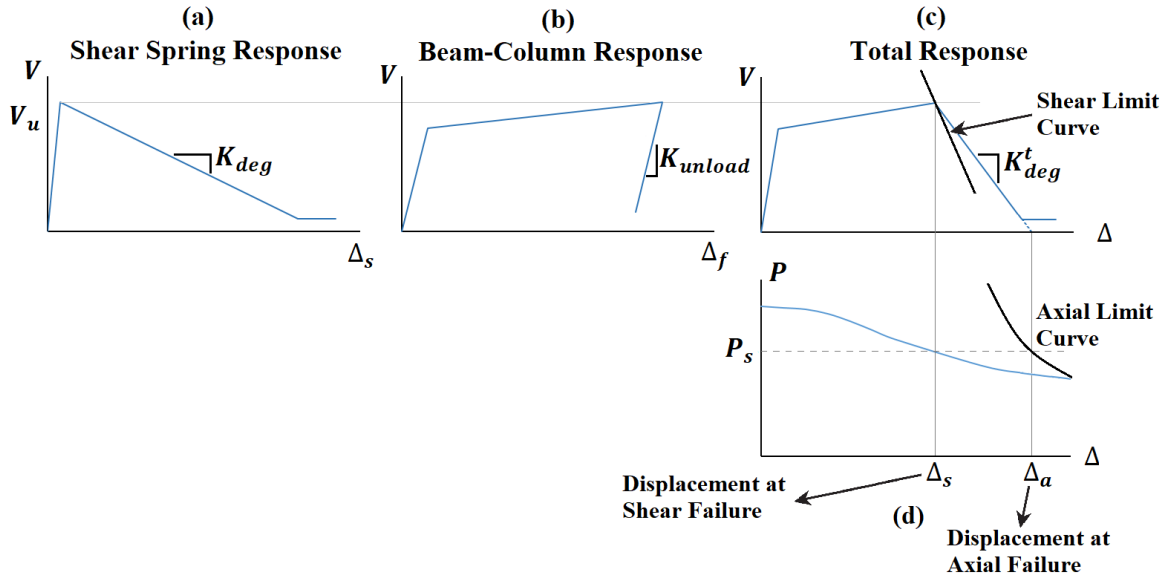


Figure 5: Determination of the degrading slope, K_{deg} - Elwood [7], Sattar and Liel [14]

Experimental studies have shown that axial failure occurs when the shear strength degrades to approximately zero [37]. Therefore, the degrading slope of the total shear response, K_{deg}^t , can be determined using [7]:

$$K_{deg}^t = \frac{V_u}{\Delta_a - \Delta_s}, \quad (19)$$

where V_u is the ultimate shear capacity of the column, Δ_s is the displacement at shear failure calculated from Equation 18, and Δ_a is the displacement at axial failure calculated from Equation 19 for the axial load at shear failure, P_s , which may be different from the axial load P_a at which axial failure is eventually detected.

Because the shear spring and the elastic beam-column element are connected in series, the shear spring degrading stiffness K_{deg} can then be calculated as follows:

$$K_{deg} = \left(\frac{1}{K_{deg}^t} - \frac{1}{K_{unloading}} \right)^{-1}, \quad (20)$$

where $K_{unloading}$ is the unloading stiffness of the beam-column element and depends on the boundary conditions (e.g., $K_{unloading}$ is $12EI/L^3$ for a beam-column element with fixed ends).

To ensure that no axial flexibility is added to the response of the beam-column element, the axial spring is assigned an initial spring stiffness

$$K_{axial} = 100E_c A_g / L \quad (21)$$

Moreover, the axial spring degrading stiffness $K_{deg,a}$ is calculated following Kakavand [38]:

$$K_{deg,a} = 0.02 \frac{E_c A_g}{L}, \quad (22)$$

The shear and axial springs are implemented in OpenSees using zero-length elements. They are assigned uniaxial materials with hysteretic response defined using the *LimitStateMaterial* command developed by Elwood. The *LimitCurve* command, also developed by Elwood, is used to assign the limit curves to the shear and axial uniaxial materials. It is important to note that the axial and shear limit curves are defined in OpenSees using US Customary units (and the system of units is not taken as input to these functions). Therefore, OpenSees models that make use of these limit curves must be defined in US customary units (they cannot be defined in metric SI units).

3. Modeling Parameters:

Following ASCE 41-13 [17, 22], modeling parameters calculated should represent median load values of the structure. Consequently, the gravity loads used for structural analysis are:

$$W = 1.0DL + 0.25LL \quad (23)$$

The resulting initial column axial loads are provided in Tables 5 and 6. Based on these expected loads and on the design details of the columns and beams (from Tables 1 to 4), the modeling parameters of the rotational springs are calculated using equations (12 to 14) with expected material properties $f'_c = 17.6 \text{ MPa}$ and $f_y = 480 \text{ MPa}$. Note that slip is assumed to occur and a_{sl} is taken as 1 in equation 12. The calculated model parameters of the rotational springs are shown in Table 5 and Table 6 for columns and in Table 7 and Table 8 for beams. Tables 5 and 6 also list the ratio V_p/V_n calculated for each column using equations 4 and 5. For columns with $V_p/V_n \geq 0.7$, shear and axial springs are introduced, and conservative first estimates of the drifts at shear and axial failure are calculated using equations 15 and 18 and assuming that $V = V_n$ and that P is the initial axial load. The modeling parameters of the 4-story and 12-story building columns are shown in Appendix B.

Table 5: 8-Story building exterior frame column modeling parameters

Shear/Axial Springs							
Floor	Type	$P/A_g f'_c$	$M_y \text{ (KN.m)}$	V_p/V_n	EI_{stf}/EI_g	Δ_s/L	Δ_a/L
1	Interior	0.35	603	1.03	0.55	0.0108	0.047
2	Interior	0.31	606	1.07	0.51	0.0125	0.050
3	Interior	0.26	550	1.00	0.47	0.0142	0.054
4	Interior	0.22	525	0.98	0.42	0.0159	0.059

5	Interior	0.20	322	0.71	0.42	0.0180	0.061		
6	Interior	0.15	291	0.77	0.36	0.0200	0.068		
Flexural Springs									
Floor	Type	$P/A_g f'_c$	M_y (KN.m)	V_p/V_n	EI_{stf}/EI_g	M_c/M_y	$\theta_{cap,pl}$	θ_{pc}	λ
1	Exterior	0.21	83	0.54	0.75	1.13	0.0298	0.0255	7
2	Exterior	0.19	82	0.55	0.7	1.13	0.0314	0.0285	8
3	Exterior	0.16	82	0.55	0.65	1.13	0.033	0.0318	8
4	Exterior	0.13	82	0.56	0.59	1.13	0.0347	0.0355	8
5	Exterior	0.12	58	0.41	0.57	1.13	0.0377	0.0422	9
6	Exterior	0.09	54	0.39	0.51	1.13	0.0399	0.0479	9
7	Exterior	0.06	49	0.36	0.44	1.13	0.0423	0.0543	10
	Interior	0.10	260	0.43	0.35	1.13	0.0471	0.0675	81
8	Exterior	0.03	44	0.33	0.37	1.13	0.0488	0.0616	10
	Interior	0.05	228	0.39	0.35	1.13	0.0517	0.0827	87

Table 6: 8-Story building interior frame column modeling parameters

Shear/Axial Springs									
Floor	Type	$P/A_g f'_c$	M_y (KN.m)	V_p/V_n	EI_{stf}/EI_g	Δ_s/L	Δ_a/L		
1	Interior	0.36	307	0.74	0.80	0.0182	0.0265		
2	Interior	0.31	306	0.76	0.78	0.0195	0.0293		
3	Interior	0.26	285	0.72	0.71	0.0208	0.0327		
4	Interior	0.22	283	0.74	0.64	0.022	0.0371		
Flexural Springs									
Floor	Type	$P/A_g f'_c$	M_y (KN.m)	V_p/V_n	EI_{stf}/EI_g	M_c/M_y	$\theta_{cap,pl}$	θ_{pc}	λ
1	Exterior	0.34	98	0.58	0.80	1.13	0.022	0.014	6
2	Exterior	0.30	97	0.58	0.80	1.13	0.024	0.016	6
3	Exterior	0.25	92	0.56	0.80	1.13	0.026	0.019	7
4	Exterior	0.21	91	0.57	0.75	1.13	0.028	0.023	7
5	Exterior	0.19	74	0.48	0.71	1.13	0.031	0.028	8
	Interior	0.30	136	0.59	0.80	1.13	0.026	0.018	13
6	Exterior	0.14	66	0.44	0.61	1.13	0.034	0.034	8
	Interior	0.22	134	0.61	0.70	1.13	0.029	0.025	15
7	Exterior	0.09	58	0.40	0.51	1.13	0.037	0.041	9
	Interior	0.15	123	0.59	0.57	1.13	0.034	0.033	16
8	Exterior	0.04	49	0.35	0.41	1.13	0.041	0.05	10
	Interior	0.07	103	0.52	0.42	1.13	0.039	0.045	18

Table 7: Exterior beams modeling parameters

Rotational Spring at the Left Side								
Beam Span	M_{y+} (KN.m)	M_{y-} (KN.m)	EI_{stf}/EI_g	M_c/M_y	$\theta_{cap,pl+}$	$\theta_{cap,pl-}$	θ_{pc}	λ
1	67.4	67.4	0.35	1.13	0.035	0.035	0.037	19
2	67.1	102.5	0.35	1.13	0.039	0.032	0.037	19
3	67.2	86.1	0.35	1.13	0.037	0.033	0.037	19
4	67.1	102.5	0.35	1.13	0.039	0.032	0.037	19
5	67.3	67.4	0.35	1.13	0.035	0.035	0.037	19
Rotational Spring at the Right Side								
Beam Span	M_{y+} (KN.m)	M_{y-} (KN.m)	EI_{stf}/EI_g	M_c/M_y	$\theta_{cap,pl+}$	$\theta_{cap,pl-}$	θ_{pc}	λ
1	102.5	67.1	0.35	1.13	0.032	0.039	0.037	19
2	86.1	67.2	0.35	1.13	0.033	0.037	0.037	19
3	86.1	67.2	0.35	1.13	0.033	0.037	0.037	19
4	102.5	67.18	0.35	1.13	0.032	0.039	0.037	19
5	67.4	67.4	0.35	1.13	0.035	0.035	0.037	19

Table 8: Interior beams modeling parameters

Rotational Spring at the Left Side								
Beam Span	M_{y+} (KN.m)	M_{y-} (KN.m)	EI_{stf}/EI_g	M_c/M_y	$\theta_{cap,pl+}$	$\theta_{cap,pl-}$	θ_{pc}	λ
1	137	131.9	0.35	1.13	0.037	0.037	0.043	60
2	120.7	206.8	0.35	1.13	0.042	0.033	0.043	60
3	120.7	182.1	0.35	1.13	0.041	0.034	0.043	60
4	120.5	182.1	0.35	1.13	0.041	0.034	0.043	60
5	137.5	206.7	0.35	1.13	0.034	0.027	0.028	19
Rotational Spring at the Right Side								
Beam Span	M_{y+} (KN.m)	M_{y-} (KN.m)	EI_{stf}/EI_g	M_c/M_y	$\theta_{cap,pl+}$	$\theta_{cap,pl-}$	θ_{pc}	λ
1	206.7	137	0.35	1.13	0.037	0.037	0.043	60
2	182.1	120.7	0.35	1.13	0.033	0.042	0.043	60
3	182.1	120.7	0.35	1.13	0.034	0.041	0.043	60
4	206.8	120.5	0.35	1.13	0.034	0.041	0.043	60
5	131.9	137.5	0.35	1.13	0.034	0.041	0.043	60

C. Joint Model

Joints of GLDRC frames lack transverse reinforcements and thus are expected to undergo large shear deformations when subjected to seismic loads. Several researchers have proposed analytical models for beam-column joints. The scissors approach proposed by Alath [39] is used in this study because it correlates well with experimental results on unreinforced beam column joints [40]. As illustrated in Figure 6, the scissors approach is composed of a single rotational spring located at the center of the joint and of rigid links representing the finite size of the joint.

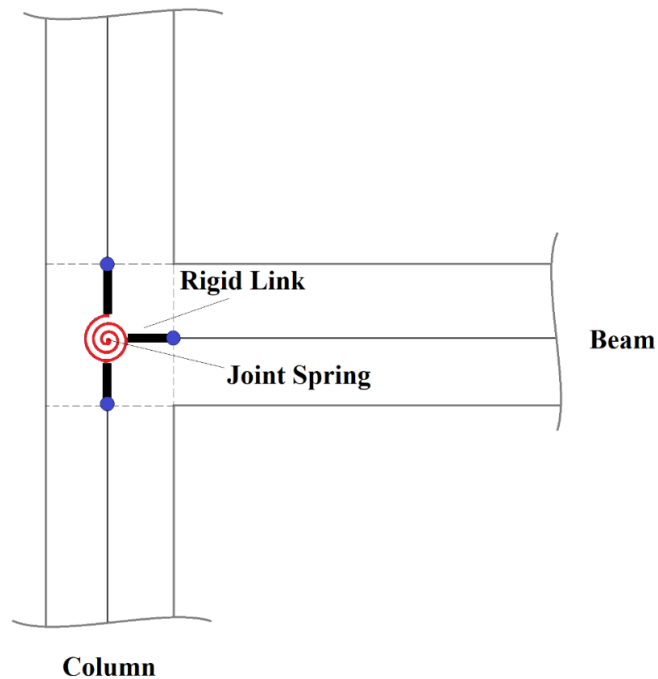


Figure 6: Joint scissors model - Alath [39]

Experimental tests conducted on unreinforced beam-column joints have shown hysteretic response with pinching behavior. Strength and stiffness degradation are ignored in existing joint models because they have been found to have an insignificant effect on

structural collapse [41]. First, a backbone such as the one shown in Figure 7 is used to define the behavior of the joint.

In this study, and following Lowes and Altoontash [42], the backbone of the joint spring is defined using four points identified as cracking, yielding, ultimate and residual. The hysteretic pinching response is defined by three parameters, $rDisp$ which defines the ratio of the deformation at which reloading occurs to the maximum or minimum historic deformation demand, $fForce$ which defines the ratio of the force at which reloading begins to the force corresponding to the maximum or minimum historic deformation demand, and $uForce$ which defines the ratio of the strength developed upon unloading from a negative load to the maximum strength developed under monotonic loading.

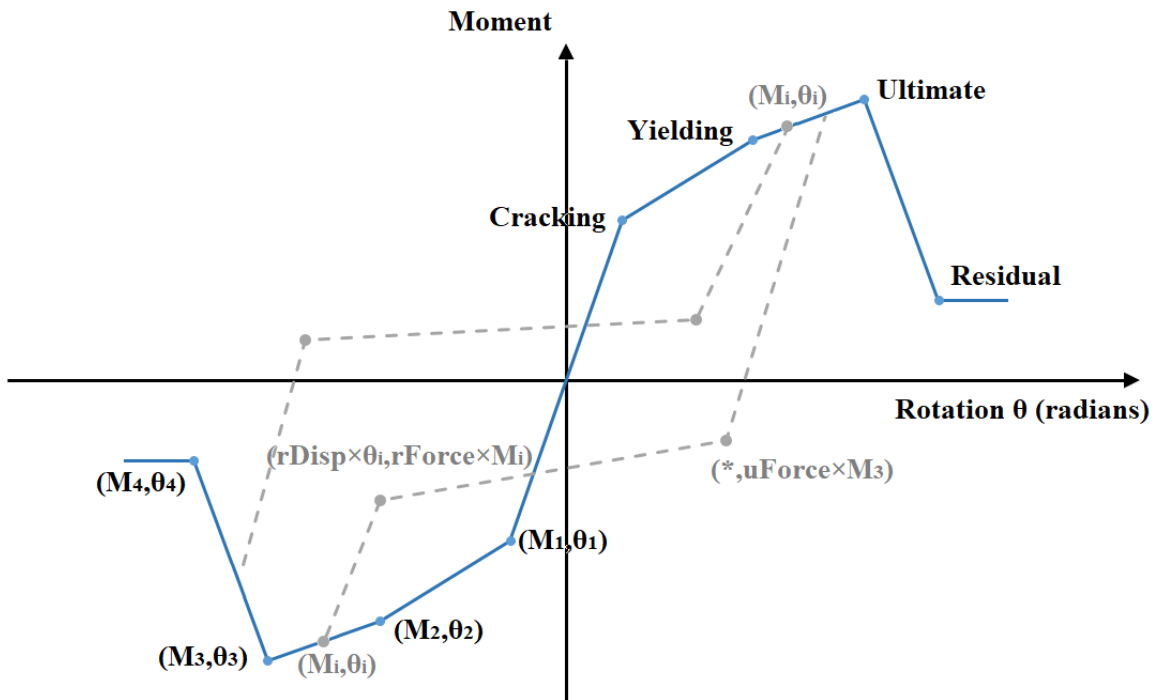


Figure 7: Hysteretic pinching material - Lowes and Altoontash [42]

Several researchers calibrated the joint spring model parameters to experimental results from unreinforced beam-column joints. However, these calibrated parameters greatly depend on the experimental joint dimensions and details, and none of the proposed models were for unreinforced wide beam-column joints such as the joints of the studied building. Therefore, the experimental results on unreinforced wide beam-column joints by Elsouri and Harajli [3] are used to calibrate a new joint model. The proposed joint model, along with other previous models, are investigated in detail in the next chapter.

D. Mass and Damping:

The mass sources considered in the model are the dead load and 0.25 times the live load. These seismic masses are lumped at the beam ends and assigned to the lateral degrees of freedom. Negligible mass sources are assigned to the other degrees of freedom to avoid a sparse mass matrix and numerical stability issues [16, 25].

As for damping, mass and stiffness proportional Rayleigh damping is used, whereby the viscous damping matrix $[C]$ is defined as:

$$[C] = \alpha[M] + \beta[K], \quad (24)$$

where $[M]$ is the mass matrix, $[K]$ is the stiffness matrix, α is the mass proportional factor, and β is the stiffness proportional factor.

Several approaches are used in literature for damping assignments. Elwood and Moehle [43] used mass-proportional damping with equivalent viscous damping of 2%. They did not use stiffness-proportional damping because the sudden change in the response

of the axial and shear springs at failure resulted in large damping forces at the node connecting the beam-column element and the spring. Sattar and Liel [14] assigned Rayleigh with equivalent viscous damping value of 2% to the first and third modes. However, they assigned damping only to the elastic frame elements. Galanis [25] used mass and stiffness proportional Rayleigh damping, and assumed $\zeta = 2\%$ for the first and third mode. The latter approach for damping assignments is followed.

The stiffness matrix used to define Rayleigh damping can be defined as the initial stiffness matrix, the current or tangent stiffness matrix, or the committed stiffness matrix defined as the matrix converted at the last analysis step.

Ibarra and Krawinkler [27] discarded the use of the current stiffness matrix because it is not yet clear how to use the tangent stiffness formulation when non-linear elements have a negative slope. Also, the use of the tangent stiffness matrix may lead to potential unbalance of forces. If the initial stiffness is used, the change in stiffness of non-linear elements may cause spurious damping moments at the joints and thus violation of static equilibrium. Therefore, to satisfy static and dynamic equilibrium, the use of the initial stiffness was suggested by Ibarra and Krawinkler [27], but with two conditions: first, to assign zero stiffness proportional damping to plastic hinges, and second, to model rotational springs with an initial stiffness several times larger than that of the beam-column element.

Following Ibarra and Krawinkler [27], the initial stiffness is used to define Rayleigh damping in this study. OpenSees does not apply stiffness proportional damping to zero-length elements and thus the first condition is met. To satisfy the second condition, the initial stiffness of the rotational springs is set as $K_{spring} = nK_{elastic}$, where n is a stiffness

modification factor assumed equal to 10 [27], and $K_{elastic}$ is the rotational stiffness of the linear-elastic element. Since the model of each beam-column element is composed of two non-linear rotational springs and an elastic element, then the total rotational stiffness $K_{beam-column}$ of the beam-column element is defined as:

$$K_{beam-column} = \frac{1}{1/K_{elastic} + 1/K_{spring}} = \frac{K_{elastic} \times K_{spring}}{K_{elastic} + K_{spring}}, \quad (25)$$

$$K_{elastic} = \frac{n+1}{n} K_{beam-column}, \text{ and } K_{spring} = (n+1) K_{beam-column}, \quad (26)$$

where $K_{beam-column} = 6EI/L$ for fixed-fixed boundary conditions. Note that, to compensate for the lack of stiffness proportional damping provided by the non-linear rotational springs, the stiffness proportional damping factor assigned to the elastic elements is modified to [27]:

$$\beta_{mod} = \left(\frac{n+1}{n}\right) \beta. \quad (27)$$

CHAPTER IV

JOINT MODEL FOR WIDE BEAM-COLUMN ELEMENTS

A. Literature Review:

Many of the buildings in Beirut are designed to resist gravity loads only, with little or no consideration to lateral resistance. The lack of seismic design and detailing leads to the use of minimum shear reinforcement in beam and column elements and to the absence of transverse reinforcement in joints. Usually, seismically designed/detailed joints can be assumed to be rigid and to maintain their orthogonality during an event of severe ground shaking. However, the lack of transverse reinforcement in joints can cause significant shear deformations that increase the inter-story drift. Therefore, it is important to consider joint flexibility in the seismic analysis of old non-ductile reinforced concrete frames.

Several researchers have proposed joint models that represent the behavior of unreinforced joints. Celik and Ellingwood [4] derived equations that relate the joint shear stress to moment and joint shear strain to rotation. The proposed equations, along with joint rotation results from previous literature, were used to define the backbone curve for the joint spring. De Risi *et al.* [5] conducted experimental tests on unreinforced exterior beam-column joints. The results of their experiments, along with results from previous literature on similar joint types, were used to recalibrate the model parameters for exterior joints. Then, to assess an old non-ductile frame, the joint parameters that they calibrated were used

for exterior joints, and those derived by Celik and Ellingwood [4] were used for interior joints.

Park and Mosalam [41] also proposed a joint model for unreinforced beam-column joints. An experimental database of 62 tests on unreinforced beam column joints was used to calibrate an empirical relation for joint shear strength. Experimental tests on four corner joints were conducted and the results were used to formulate empirical relations that define the backbone of corner and exterior joints. For interior joints, the presence of beams on both side provides more confinement, and thus the joint confinement factors provided by ASCE [26] were used to define the backbone for interior and roof interior joints.

The joint model parameters proposed by Celik and Ellingwood [4] and De Risi *et al.* [5] highly depend on experimental data and do not take into consideration important factors such as the joint aspect ratio. Although Park and Mosalam [41] provided equations that depend on design parameters, the database that they used is limited to square or rectangular columns with joint aspect ratio ≤ 2.0 .

Li and Kulkarni [44] studied the behavior of wide beam-column joints, but transverse reinforcements in the joint area was provided. Quintero-Febres and Wight [45] and LaFave and Wight [46] studied unreinforced beam column joints. However, the studied joints had square or rectangular columns attached to wide beams. Elsouri and Harajli [3] conducted experimental tests on unreinforced wide beam-column joints that are typical of construction in Lebanon. Joints failed prematurely, and beam-columns elements did not reach their flexural capacity. Using the same beam-column assembly, and by satisfying design and reinforcement details requirements of ACI 318-08 [47], joints showed an

improved seismic behavior mainly by delaying joint shear failure. Damaged joints were then repaired and strengthened by epoxy injection into major cracks and using carbon fiber reinforced polymers. Given the procedure was performed with minimum labor and material cost, the performance of the damaged joints greatly improved.

Due to the lack of a model that represents the cyclic response of wide unreinforced beam-column joints, the experimental data of Elsouri and Harajli [3] is used to calibrate a new model for the backbone curve of a joint spring representative of joints typical of pre-1990s Lebanese design and construction practice.

B. Joint Models:

1. Celik and Ellingwood:

Celik and Ellingwood [4] used equilibrium of forces from the joint free body diagram, as shown in Figure 8 for an interior joint, to derive relations that relate the joint shear stress to moment and joint shear strain to rotation. Formulations that include all possible joint configurations were also derived and are shown in Table 9.

Table 9: Equations to convert joint shear stress to moment and strain to rotation

Joint Configuration	Interior & Exterior Joints	Interior & Exterior Top Floor Joints
Joint Moment	$M_j = \tau_{jh} A_{jh} \frac{1}{\lambda}$	$M_j = \tau_{jh} A_{jh} \frac{1}{\lambda'}$
Joint Rotation	$\theta_j = \gamma_j$	

where, $\lambda = (1 - b_j/L_b)/jd - 1/L_c$, $\lambda' = (1 - b_j/L_b)/jd - 2/L_c$, τ_{jh} is the joint shear stress, A_{jh} is the joint area in the horizontal plane, b_j is the joint panel width, L_b is the total length of left and right beams, L_c is the total length of top and bottom columns, jd is the beam, moment arm, θ_j is the spring rotation, and γ_j is the shear strain.

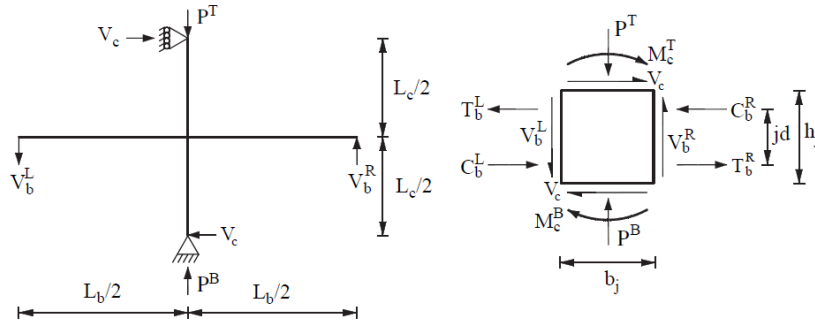


Figure 8: Joint free body diagram for interior joint - Celik and Ellingwood [4]

Experimental results from previous literature were used to properly calibrate the model. The database consisted of seven interior and six exterior joints that lacked transverse reinforcements. Some of these joints are illustrated in Figure 9. The development length of beam bottom bars was varied and extended a distance of 150 mm and 360 mm into joints. Moreover, beam bottom bars in exterior joints were hooked with a 180° hook. The rotation values reported at (1) cracking, (2) yielding, (3) ultimate and (4) residual strength were used to define the four abscissa points of the backbone curve shown in Figure 7 and fall within the following ranges: (1): 0.0001 – 0.0013, (2): 0.002 – 0.010, (3): 0.01 – 0.03, and (4): 0.03 – 0.10 radians.

The cracking and residual shear stresses are assumed equal and determined from the equation proposed by Uzumeri [48]

$$\overline{(\tau_{cr})} = 0.29 \sqrt{1 + 0.29(P/A_{jh})}; (MPa) \quad (28)$$

where $\overline{(\tau_{cr})}$ is the cracking shear stress τ_{cr} normalized by $\sqrt{f'_c}$, P is the axial load (positive in compression), and A_{jh} is the joint area.

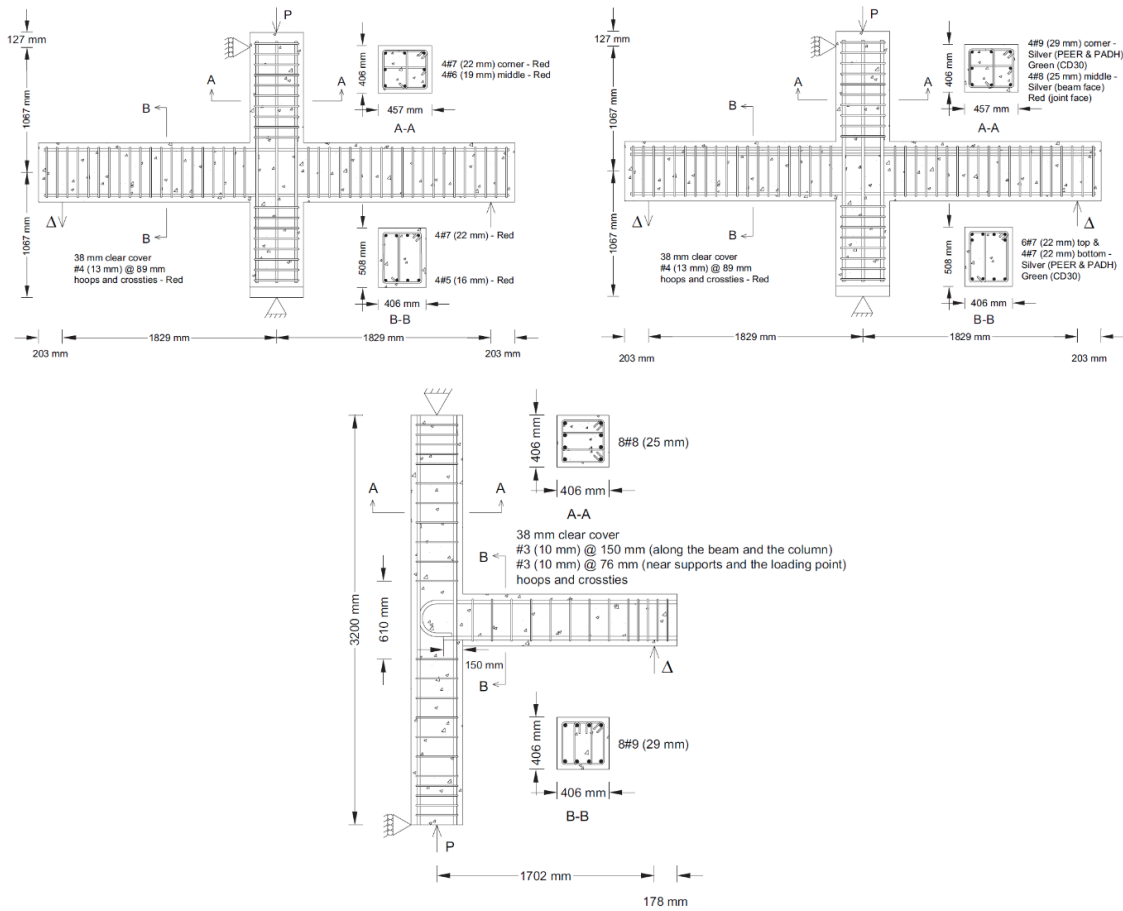


Figure 9: Joint steel layout from database - Celik and Ellingwood [4]

The shear stress is used together with the equations in Table 9 to calculate the cracking and residual moments. The joint yield and ultimate moment strengths are based on the minimum of the yield and ultimate moment strengths of all sections connecting to the

joint, respectively. However, they should not exceed the joint shear strength normalized by $\sqrt{f'_c}$, $(\overline{\tau_{jh}})_{max}$, estimated from experimental data, and which falls in the following ranges: 0.42-0.62 \sqrt{MPa} and 0.83-1.00 \sqrt{MPa} for the positive and negative backbone of the exterior joint, respectively, and 0.75-1.00 \sqrt{MPa} for the interior joint.

The fact that bottom beam bars were provided with a short embedment length lead to a reduced moment capacity. To account for such deficiency, the beam yield moment is reduced by a factor α . Using the experimental database from previous literature, Celik and Ellingwood [4] reported that α varies between 0.4 and 0.7. However, Hoffman *et al.* [49] assumed α as the ratio between the actual and the required development length as per ACI 318-89. Therefore, the moment transferred through the joint when the beams and columns reach their yield and ultimate capacity is:

$$(M_j)_{y,u} = \min \left[\frac{(M_c^T)_{y,u} + (M_c^B)_{y,u}}{\eta_c}, \frac{(\alpha M_B^+)_{y,u} + (M_B^-)_{y,u}}{\eta_B}, M((\overline{\tau_{jh}})_{max}) \right] \quad (29)$$

for interior joints,

$$(M_j)_{y,u} = \min \left[\frac{(M_c^T)_{y,u} + (M_c^B)_{y,u}}{\eta_c}, \frac{(\alpha M_B^+)_{y,u}}{\eta_B}, M((\overline{\tau_{jh}})_{max}) \right] \quad (30)$$

for the positive backbone of exterior joints, and

$$(M_j)_{y,u} = \min \left[\frac{(M_c^T)_{y,u} + (M_c^B)_{y,u}}{\eta_c}, \frac{(M_B^-)_{y,u}}{\eta_B}, M((\overline{\tau_{jh}})_{max}) \right] \quad (31)$$

for the negative backbone of exterior joints, where $\eta_c = 1 - h_j/L_c$ and $\eta_B = 1 - b_j/L_b$.

Table 10: Joint model parameters - Celik and Ellingwood [4]

Backbone Point	Cracking	Yield	Ultimate	Residual
Stress	$(\overline{\tau}_{jh})_{cr}$	$(\overline{\tau}_{jh})_{max}$	$(\overline{\tau}_{jh})_{max}$	$(\overline{\tau}_{jh})_r$
Moment	M_{cr}	$M_{y,C}, M_{y,B}, M((\overline{\tau}_{jh})_{max})^*$	$M_{u,C}, M_{u,B}, M((\overline{\tau}_{jh})_{max})^*$	M_r
Rotation (rad)	0.0001-0.0013	0.0020-0.01	0.01-0.03	0.03-0.1

*: Minimum

The joint model parameters as summarized in Table 10. Note that the additional rotation due to beam bar slip is not included. The parameters used for defining the hysteretic behavior were defined as:

$$uForce = -0.10 \quad (32)$$

$$rForce = rDisp = 0.15 \quad (33)$$

2. De Risi, Ricci:

De Risi *et al.* [5] performed experimental cyclic tests on two exterior unreinforced joints designed to represent old buildings in Italy and illustrated in Figure 10. Beam bottom and top bars were bent with a 90° hook with a length of 20 cm. The results of the conducted experiments and previous tests on joints with similar features were used to define the joint model parameters.

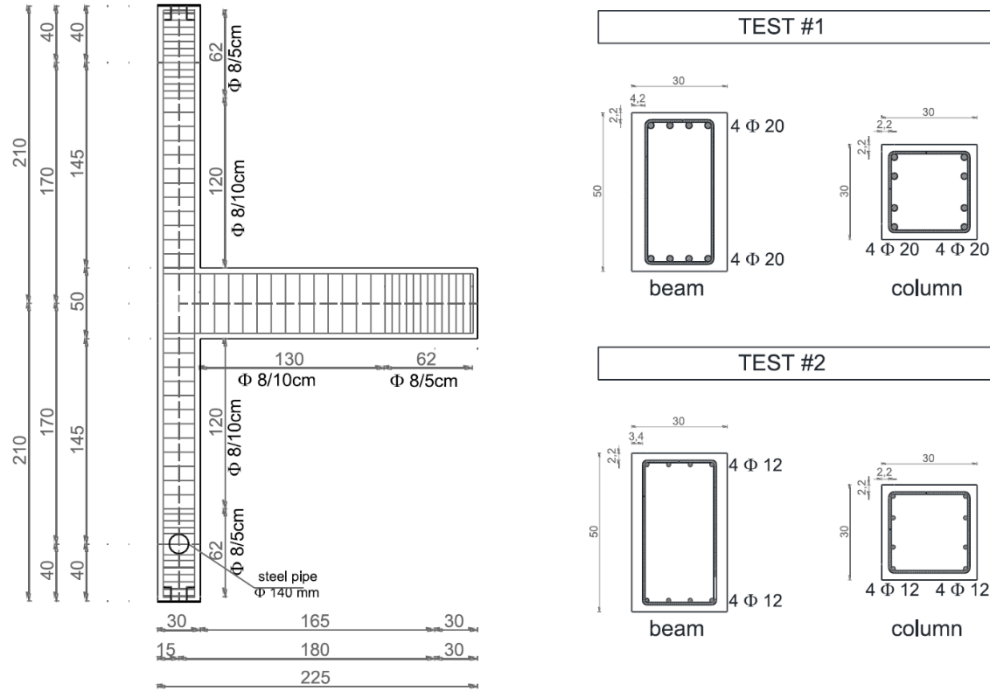


Figure 10: Exterior joint layout - De Risi *et al.* [5]

The ordinates of the backbone curve are defined in a similar manner to Celik and Ellingwood [4]. However, the shear strength for exterior and interior joints is calculated from the equations proposed by Jeon *et al.* [50] and defined as:

$$\ln(\tau_{j,max}) = -0.81 + 0.46 \ln(f'_c) + 0.5 \ln(\tau_d) + 0.68 \ln(JP) + 0.62 \ln(TB) - 0.52 \ln\left(\frac{h_b}{h_c}\right) + 0.08 \ln(M_R) + 0.14 \ln(\theta), \quad (34)$$

where τ_d is the design joint shear stress demand, JP is the in-plane geometry factor ($JP = 1$ for interior joints and 0.75 for exterior joints), TB is the out-of-plane factor ($TB = 1.25$ for transverse beams and 1.0 for no or one transverse beam), h_b/h_c is beam to column depth ratio, M_R is column to beam flexural strength ratio, and θ is the ratio of intermediate column reinforcement strength to design joint shear demand.

The abscissa values are based on mean values of the experiments and are defined as: (1): 0.0004, (2): 0.0017 (3): 0.0049, and (4): 0.0441 radians. Note that these rotational values do not include beam bar slip.

Table 11: Exterior joint model parameters - De Risi *et al.* [5]

Backbone Point	Cracking	Yield	Ultimate	Residual
Stress	$(\bar{\tau}_{jh})_{cr}$	$(0.85\bar{\tau}_{jh})_{max}, \bar{\tau}_{col}^y, \bar{\tau}_{beam}^y *$	$(\bar{\tau}_{jh})_{max}, \bar{\tau}_{col}^u, \bar{\tau}_{beam}^u *$	$0.43(\bar{\tau}_{jh})_{max}$
Moment	M_{cr}	$M_{y,C}, M_{y,B}, M((\bar{\tau}_{jh})_{max}) *$	$M_{u,C}, M_{u,B}, M((\bar{\tau}_{jh})_{max}) *$	M_r
Rotation (rad)	0.0004	0.0017	0.0049	0.0441

*: Minimum

The model parameters used to define the hysteretic response were calibrated as:

$$uForce = -0.22 \quad (35)$$

$$rForce = 0.23 \quad (36)$$

$$rDisp = -0.22 \quad (37)$$

3. Park and Mosalam:

Park and Mosalam [41] used an experimental database of 62 tests on exterior and corner unreinforced joints to calibrate an empirical equation that predicts the joint shear strength. They found that shear strength depends mainly on the joint aspect ratio, beam longitudinal reinforcement ratio, and concrete strength. The proposed equation was then modified to include the confinement effect provided by elements surrounding the joints (i.e., an interior joint is confined by two beams and two columns):

$$V_n = k \left[\Gamma * 12\sqrt{f'_c} b_j h_c \frac{\cos(\theta)}{\cos(\pi/4)} \right] \text{ (psi) and } \theta = \tan^{-1}(h_b/h_c) \quad (38)$$

$$k = 0.4 + 0.6 \left(\frac{SI_j - X_1}{X_2 - X_1} \right) \leq 1.0, X_1 = \Gamma * 4 \frac{\cos\theta}{\cos(\pi/4)}, X_2 = \Gamma * 12 \frac{\cos\theta}{\cos(\pi/4)} \quad (39)$$

$$SI_j = \left(\frac{A_s f_y}{b_j h_c \sqrt{f'_c}} \right) \left(1 - 0.85 \frac{h_b}{H} \right) \quad (40)$$

where, h_b is the beam height, h_c is the column height, b_j is the joint effective width defined as $b_j = (b_b + b_c)/2$, f'_c is concrete compressive strength, H is the distance between the upper and bottom column inflection points, A_s is the beam tensile reinforcement area, f_y is the yield stress, Γ is strength ratio factor, and k is a strength factor that account for beam longitudinal reinforcement ratio.

Four tests on unreinforced beam-column joints illustrated in Figure 11 were conducted. The two varied test parameters were the joint aspect ratio and beam longitudinal reinforcement ratio. The results showed that the shear strength increases with the increase in beam reinforcement ratio and decreases with the increase in joint aspect ratio. It was also observed that the deformation at the beam-joint interface depends on the joint aspect ratio only. Moreover, the rotation at the column-joint interface is negligible due to the strong column/weak beam configuration.

The unloading and reloading parameters used to define the hysteric pinching response were selected as:

$$uForce = 0.05 \quad (41)$$

$$rForce = 0.25 \quad (42)$$

$$rDisp = 0.5 \quad (43)$$

Note that Park and Mosalam [41] defined the ordinates of the joint backbone curve differently than Celik and Ellingwood [4] and De Risi *et al.* [5]. First the maximum moment that the joint can withstand, M_n , is computed and assigned to the ultimate point, point (3). Then reduction factors λ_1 , λ_2 and λ_4 which were fitted from experimental data are multiplied by M_n and assigned to the 1st (M_1), 2nd (M_2), and 4th (M_4) points.

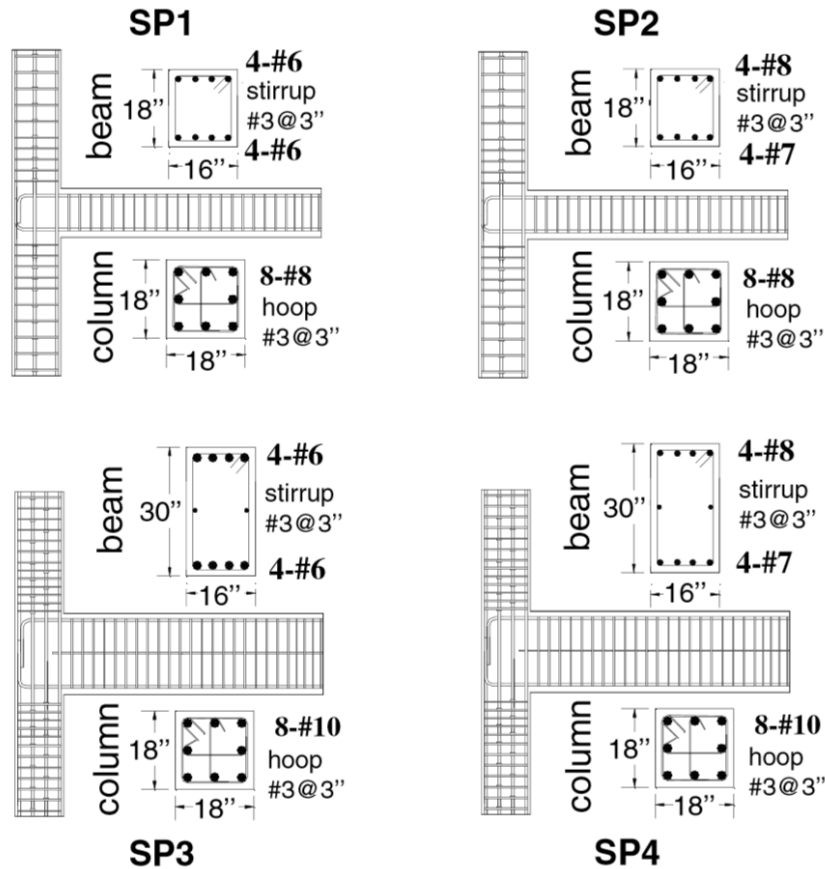


Figure 11: Corner joints layout - Park and Mosalam [41]

Park and Mosalam [41] found that the rotations θ_1 and θ_2 are insensitive to the joint aspect ratio and beam longitudinal reinforcement ratio, and they assigned them as $\theta_1 = 0.0025$ and $\theta_2 = 0.0050$. They found that θ_3 depends only on the joint aspect ratio and empirically fitted it as $\theta_3 = 0.0325 - 0.0125h_b/h_c$. The last point was determined to

be $\theta_4 = \theta_3 + 0.03$, by fitting the negative slope of the load displacement relation because the test measurements became unreliable after severe joint damage.

It is assumed that the derived interior and exterior joint parameters can be used for the roof interior and corner joints as well. Also, the derived joint rotations include rotations due to beam bottom bar slip. The joint parameters derived by Park and Mosalam [41] are summarized in Table 12.

Table 12: Joint model parameters -Park and Mosalam [41]

Joint Type	θ_1	λ_1	θ_2	λ_2	θ_3	λ_4	θ_4	Γ
Exterior	0.0025	0.65	0.005	0.9	$0.0325 - 0.0125(h_b/h_c)$	0.5	$\theta_c + 0.03$	1.00
Roof Exterior								0.66
Interior	0.01		1.67					
Roof Interior	0.005	1.00						

4. Elsouri and Harajli:

Elsouri and Harajli [3] studied the response of unreinforced wide beam-column elements. A 5-story reinforced concrete frame was designed to resist gravity loads only. The design parameters used were similar to typical older construction practice in Lebanon, where the structural system consists of a one-way ribbed slab with wide concealed beams. Columns were designed as wide elements and hidden within the infill walls. Material strength used was similar to the conventional practices and assumed as $f'_c = 20 \text{ MPa}$, $f_y = 420 \text{ MPa}$, and $f_{yt} = 280 \text{ MPa}$.

Four full scale unreinforced joints were constructed and are shown in Figure 12. The four specimens represent interior joints, exterior joints, and different beam-column

orientations. The ribbed slab has a thin concrete topping and is provided with minimum reinforcement. The slab is expected to crack prematurely in case of ground shaking and thus was not included in the experimental setup.

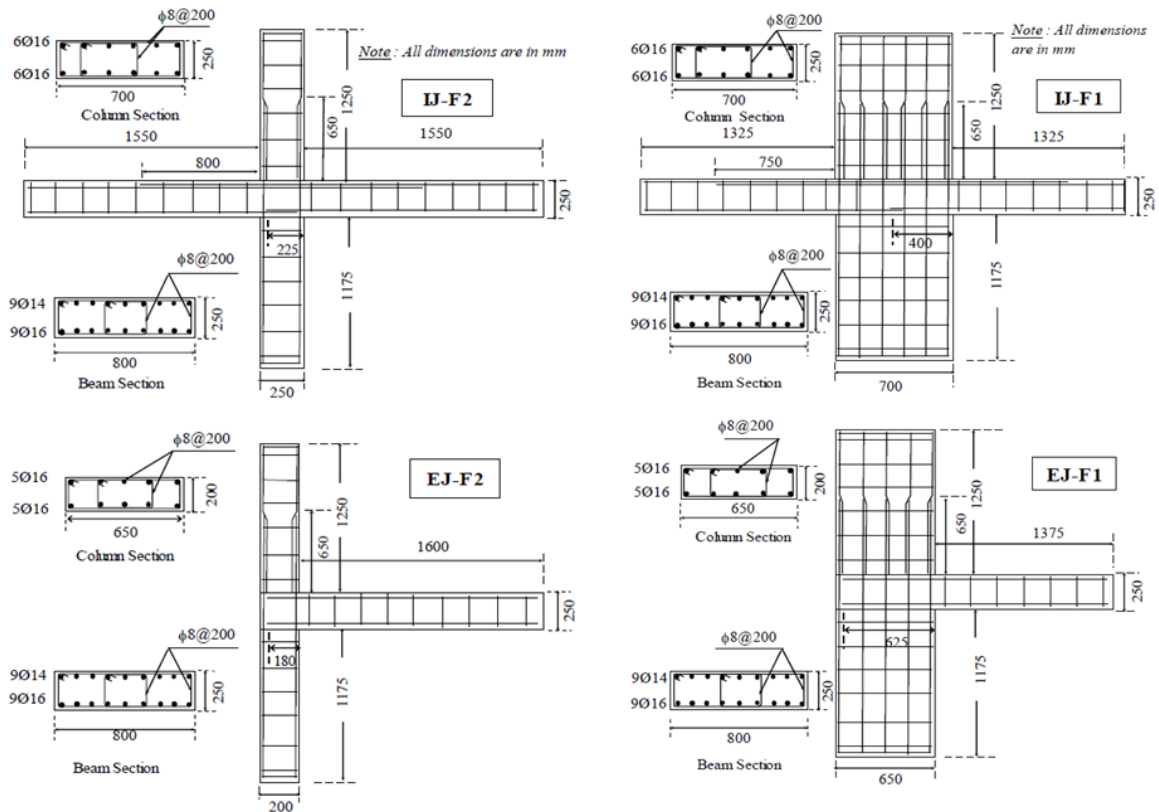


Figure 12: Wide beam-column element configurations - Elsouri and Harajli [3]

The behavior of specimens *IJ – F1*, *EJ – F1*, and *EJ – F2* was similar despite the differences in beam-column orientation and design parameters. The first flexural cracks appeared at the beam interface at drift ratios of 1.0%. Diagonal shear cracks developed at drift ratios between 1.0% – 1.5% indicating the onset of shear failure. At drift ratios of 1.75% – 2.0%, complete shear failure occurred and was followed by strength degradation to drift ratios between 4.0% – 4.5%.

Specimen *IJ – F2* was tested in two stages, cyclic displacements up to drift ratios of 4.5% drift ratios, which represents the drift capacity of the actuator, and half cyclic displacements up to drift ratios of 8.5%. The first flexural cracks appeared at the beam interface at drift ratios of 1.0%, followed by diagonal shear cracking appearance at ratios between 1.5% – 2.0%. Beyond a drift ratio of 4.5%, half cycles were applied, and the specimen resisted lateral loading until a drift ratio of 7.0%. Strength degradation was observed until a maximum drift ratio of 8.5% was reached. The results of the test are summarized in Table 13.

Table 13: Experimental joint rotation results - Elsouri and Harajli [3]

Joint ID	Joint Rotation (%)			
	Flexural Cracking at Beam Interface	Yielding	Ultimate	Residual
EJ-F1	1.0	1.0-1.5	1.75-2.0	4.0-4.5
IJ-F1	1.0	1.0-1.5	1.75-2.0	4.0-4.5
EJ-F2	1.0	1.0-1.5	1.75-2.0	4.0-4.5
IJ-F2	1.0	1.5-2.0	7.0*	8.5*

*: Rotational values resulting from half cycle displacements.

C. Proposed Joint Model:

As indicated above, joint models available in literature were not calibrated to wide beam-column elements and thus a new joint model is proposed. Following previous models, a hysteretic curve with pinching behavior is used to define the joint force-deformation relation. Moreover, four points identified as cracking, yielding, ultimate, and residual must be calibrated to define the backbone. Note that, similar to Park and Mosalam [41], cyclic strength and stiffness degradation are also ignored in the proposed model.

1. Cracking:

Cracking is defined by hair-like cracks that develop in the joint region.

Unfortunately, Elsouiri and Harajli [3] did not monitor the initiation of such cracks and thus the rotation and drift values were fitted from the backbone results. Cracking was identified by the first non-linearity and occurred for all joints at drifts of 0.005. The cracking moment, determined from Equation 1 and Table 9, did not fit well with the experimental results and thus was also chosen equal to the mean value of all cracking moments.

$$M_{cr} = 0.35M_n \quad (44)$$

$$\theta_1 = 0.005 \text{ (rads)} \quad (45)$$

where, M_{cr} is the cracking moment, M_n is the maximum joint moment, and θ_1 is the cracking rotation.

2. Yielding:

Yielding was identified as the development of diagonal shear cracks within the joint core. Such cracks developed for joints $EJ - F1$, $IJ - F1$, and $EJ - F2$ at drift ratios between 0.01 – 0.015 and for $IJ - F2$ at 0.015 – 0.02.

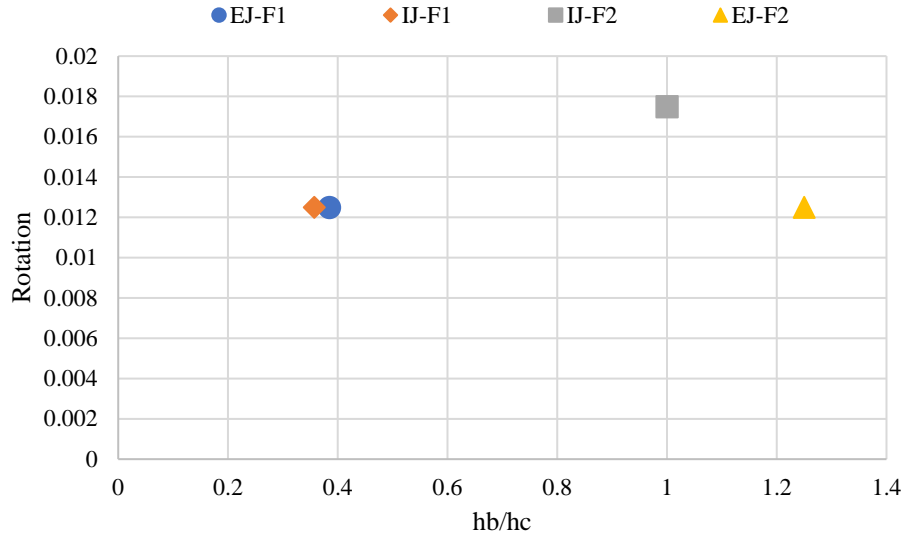


Figure 13: Yield rotation value versus beam to column aspect ratio

Therefore, the rotation at yielding seems to not be affected by the orientation of beams and columns in the exterior joints and we set $\theta_2 = 0.0125$. However, the rotation at yielding increases for interior joints with higher h_b/h_c ratio. A simple linear relation is fitted to the data points:

$$\theta_2 = 0.0078(h_b/h_c) + 0.0097 \quad (46)$$

3. Ultimate:

The ultimate point was determined from the experimental results. Joints $EJ - F1$, $IJ - F1$, and $EJ - F2$ had close ultimate drifts of 0.0176, 0.0189, and 0.0197, respectively. As expected, joint $IJ - F2$ had a higher drift value of 0.0386. These results are used to fit the ultimate rotation capacity.

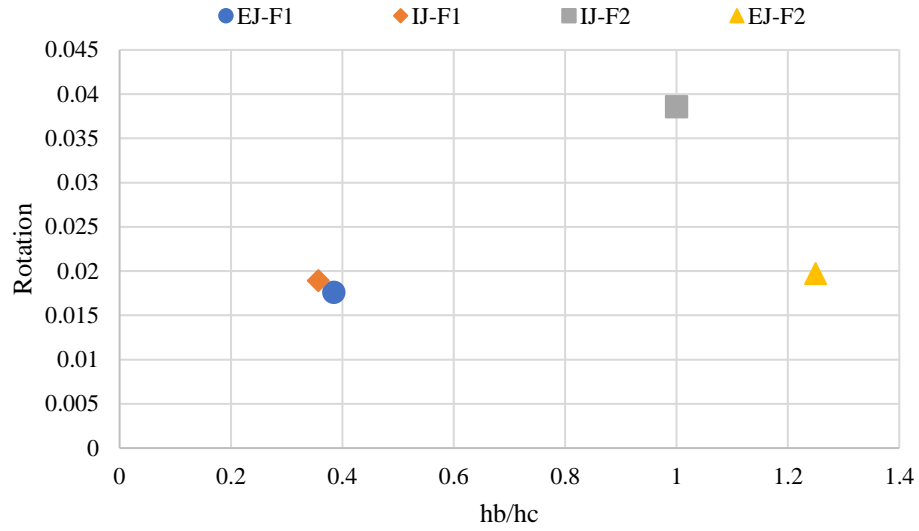


Figure 14: Ultimate rotation versus beam to column aspect ratio

As for yielding, the ultimate rotational value seems to not be affected by the beam to column aspect ratio in exterior joints, but increases with the increase of beam to column aspect ratio in interior joints. Similarly, linear regression is used to fit the rotation capacities. The following relations are identified for exterior joints,

$$\theta_3 = 0.0024(h_b/h_c) + 0.0167, \quad (47)$$

and interior joints,

$$\theta_3 = 0.0306(h_b/h_c) + 0.008. \quad (48)$$

4. Residual:

Residual rotation values were available for joints $EJ - F1$, $IJ - F1$, and $EJ - F2$ as strength degradation was greatly observed in these specimens. Following Park and Mosalam [41], and from experimental observation, the residual capacity is identified as:

$$\theta_4 = \theta_3 + 0.02 \quad (49)$$

Specimen *J1 – F2* did not reach its residual rotational capacity as the maximum drift that the actuator can withstand was reached. Due to the lack of data, the same residual drift ratio assumption is used.

Similar to the cracking moment, the residual moment is chosen as the mean value:

$$M_r = 0.4M_n \quad (50)$$

Note that the residual capacity is almost equal to the cracking moment, and this calibration is consistent with previously proposed joint models, which assign equal cracking and residual moments. The calibration results are shown in Tables 14 and 15.

Table 14: Proposed joint model rotation parameters

Joint Type	Cracking (θ_1)	Yield (θ_2)	Ultimate (θ_3)	Residual (θ_4)
Exterior	0.005	0.0125	$0.0024(h_b/h_c) + 0.0167$	$\theta_3 + 0.02$
Interior		$0.0075(h_b/h_c) + 0.0097$	$0.0306(h_b/h_c) + 0.008$	

Table 15: Proposed joint model moments

Backbone Point	Cracking	Yield	Ultimate (M_u)	Residual
Moment	$0.35M_u$	$M_{y,C}, \alpha M_{y,B}, M((\overline{\tau_{jh}})_{max})^*$	$M_{u,C}, \alpha M_{u,B}, M((\overline{\tau_{jh}})_{max})^*$	$0.4(M_u)$

*: Minimum

5. Calibrated vs Actual Response:

To verify the proposed backbone curve parameters, an OpenSees model of the exterior and interior joints is created. Similar to the methodology presented in Chapter 3, linear elastic elements with non-linear zero-length plastic hinges are used to represent the beam and column elements. In addition, joints are modeled with the scissors approach with rigid links and the proposed backbone parameters are assigned to the joint spring. An exterior joint assembly is shown in Figure 15.

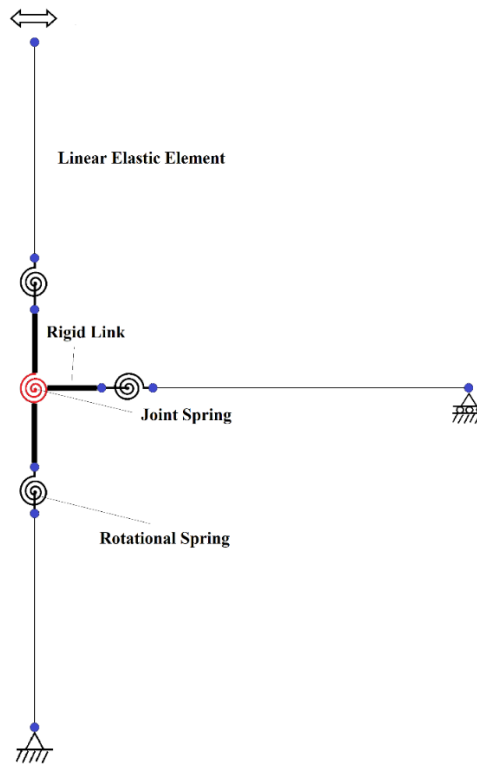


Figure 15: Exterior joint model for displacement control analysis

Displacement controlled analysis is used to apply the same displacement increments performed by Elsouiri and Harajli [3]. Hysteric pinching parameters are selected to best fit the hysteric response and are shown in Table 16.

Table 16: Proposed hysteric pinching parameters

Hysteric Parameter	$uForce$	$rForce$	$rDisp$
Exterior	-0.1	0.15	-0.1
Interior	-0.1	0.15	0.15

The simulated responses are compared to the experimental tests results of the four joints in Figure 16 to Figure 19.

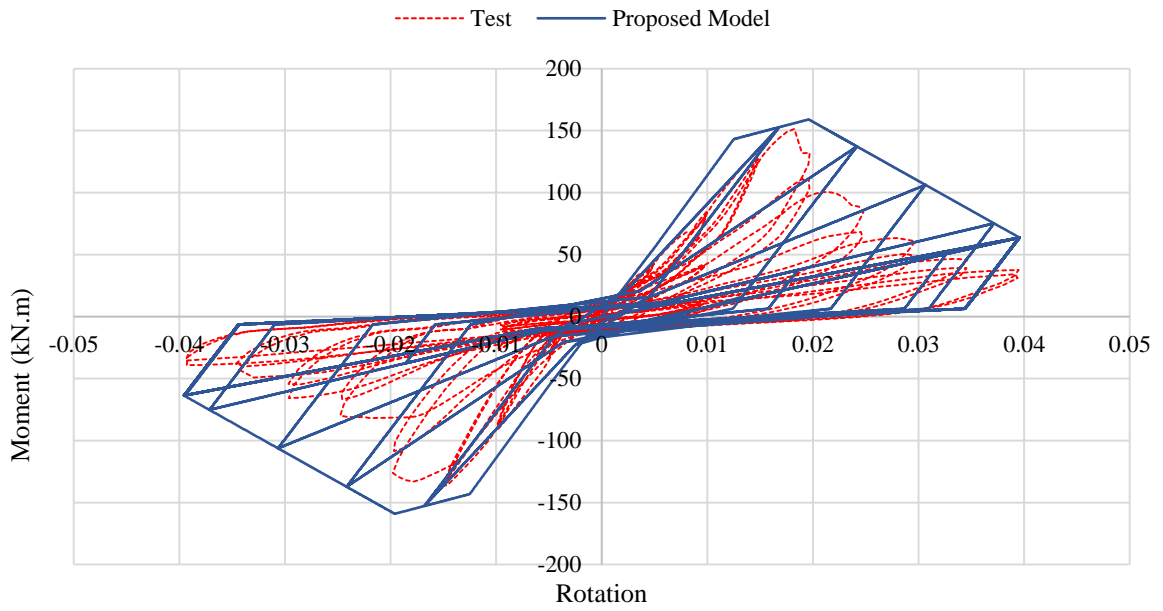


Figure 16: Calibrated vs actual response of Exterior Joint -Frame 1

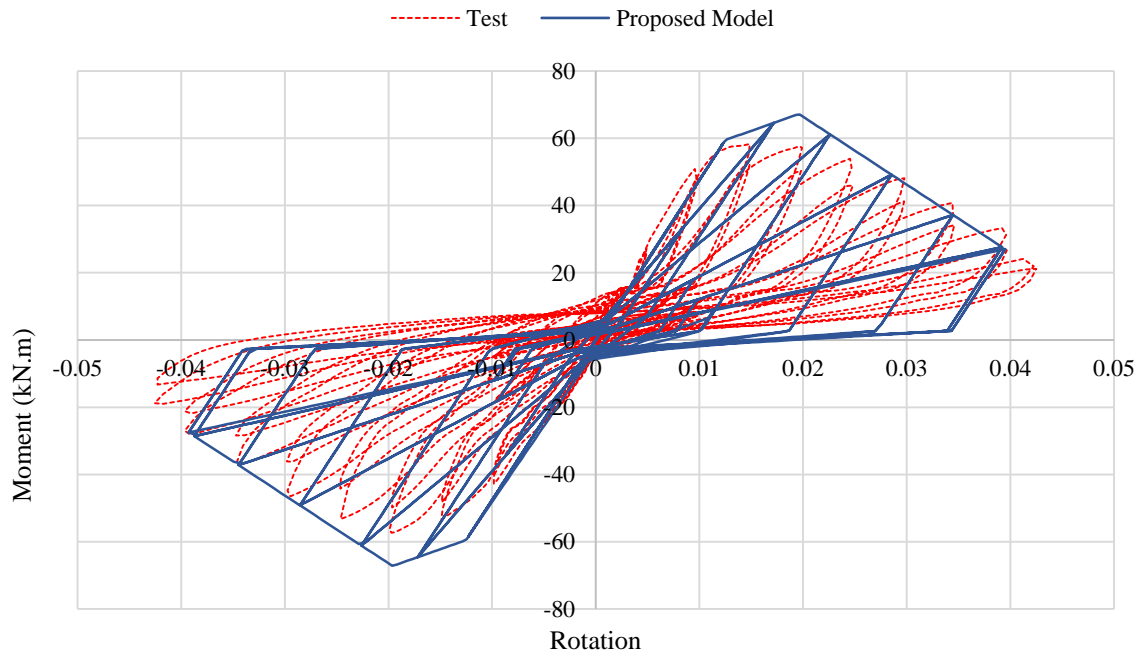


Figure 17: Calibrated vs actual response of Exterior Joint -Frame 2

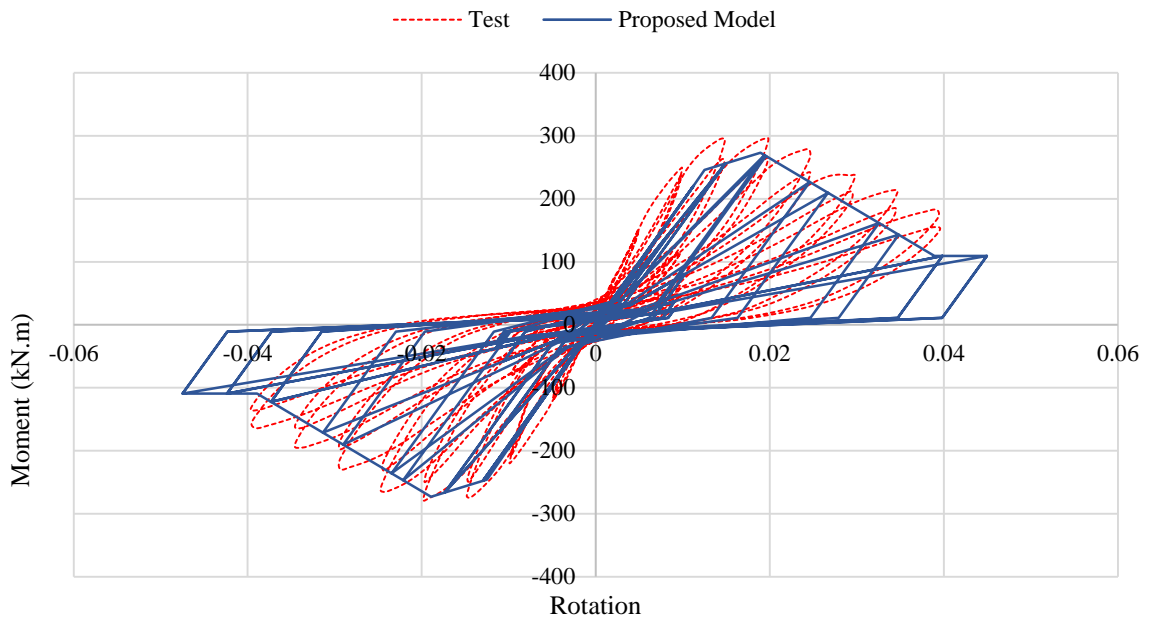


Figure 18: Calibrated vs actual response of Interior Joint -Frame 1

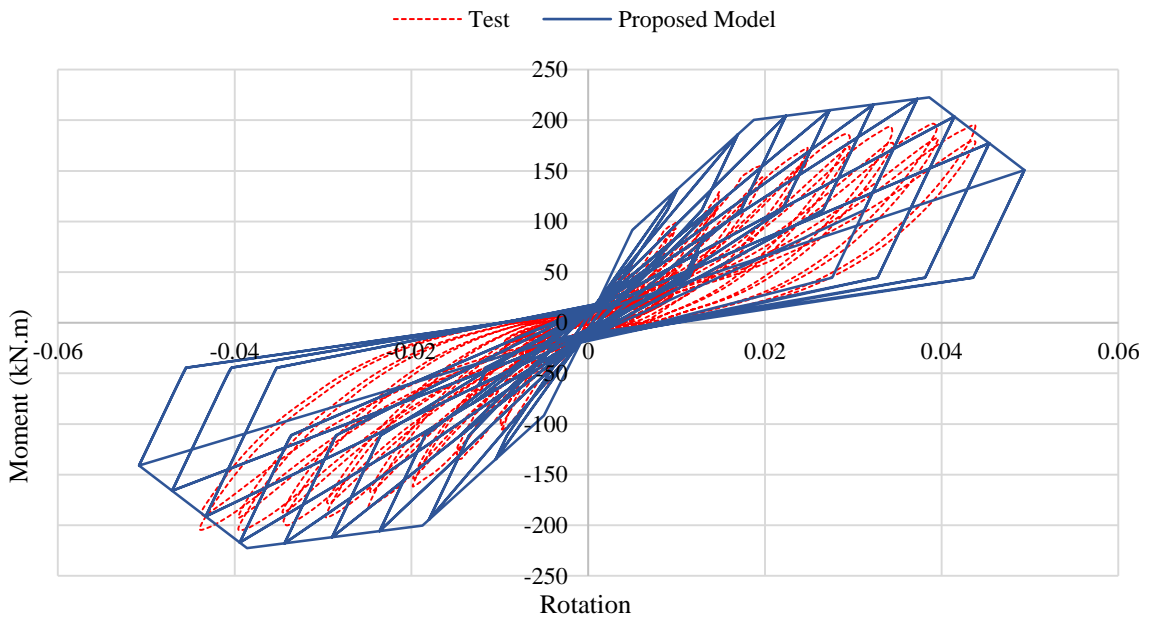


Figure 19: Calibrated vs actual response of Interior Joint -Frame 2

The figures show that the calibrated/proposed joint model is a good fit when compared to the actual response. The difference observed in the load values is due to differences in the joint shear capacity. Although the joint shear stress capacities reported by Elsouri and Harajli [3] were different from the ones estimated by ACI 318-08 [47], defined as 1.25 and $1.0 \sqrt{f'_c}$ (MPa) for interior joints and exterior joints respectively, these equations were reported to fit best with wide beam-column elements and thus are used in this study.

CHAPTER V
NONLINEAR STRUCTURAL ANALYSIS, FRAGILITY
ANALYSIS, AND COLLAPSE PERFORMANCE ASSESSMENT:
METHODOLOGY

A. Analytical Modeling

As stated above, non-linear 2D models are developed using OpenSees for the 4-, 8-, and 12-story buildings. For each building, one interior and one exterior frame are modeled, i.e., half the building.

The interior and exterior frames are modeled using the lumped plasticity approach and are connected by rigid links. Joints are modeled using the scissors approach with rigid links used to represent the finite size of the joint. Columns are fixed at the foundation and a P-Delta formulation is applied directly to the frame elements. The assembly of the 8-story building is shown in Figure 20.

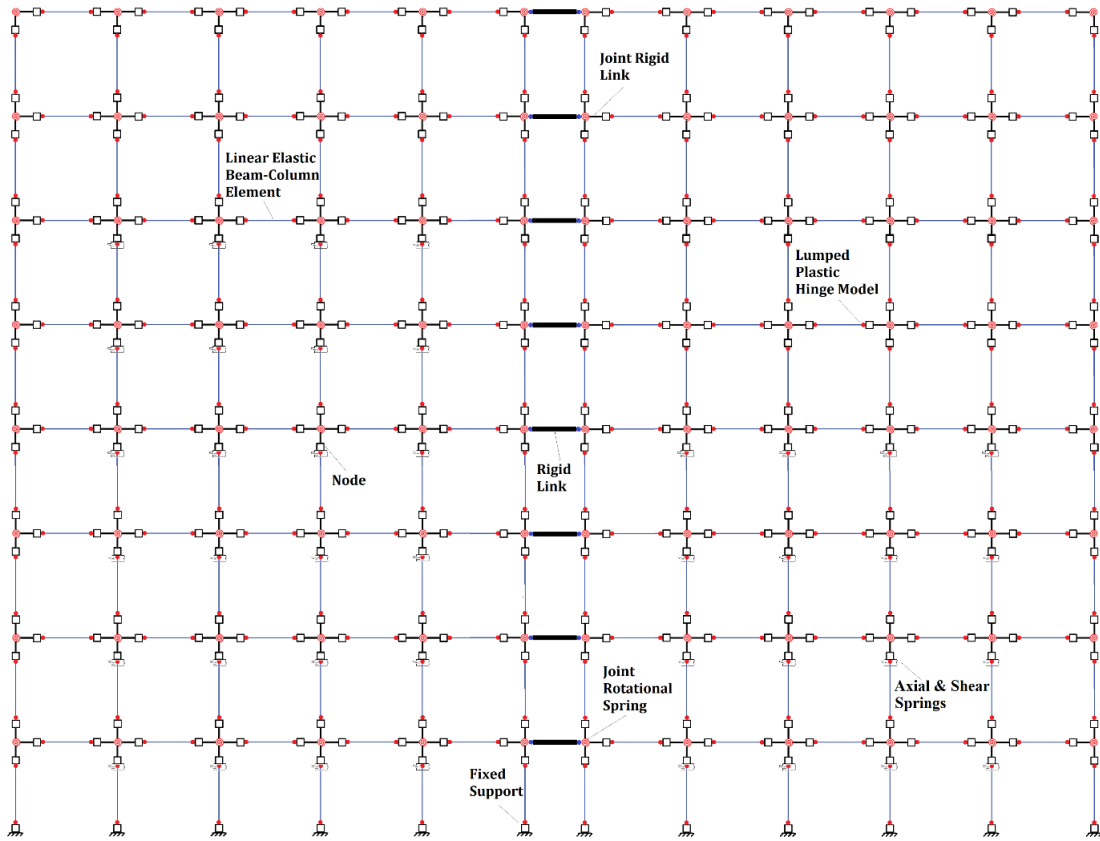


Figure 20: OpenSees model of the 8-story building

B. Non-Linear Pushover Analysis

Non-linear pushover analysis is conducted using the FEMA P-695 Methodology [17] and following ASCE 41 [22] non-linear static procedures. Forces applied at each level are in proportion to the fundamental mode shape and are distributed in proportion with the assigned seismic mass:

$$F_x \propto m_x \Phi_{1,x} \quad (51)$$

where F_x is the lateral force applied at level x , m_x is the seismic mass at level x and $\Phi_{1,x}$ is the ordinate of the fundamental mode at level x .

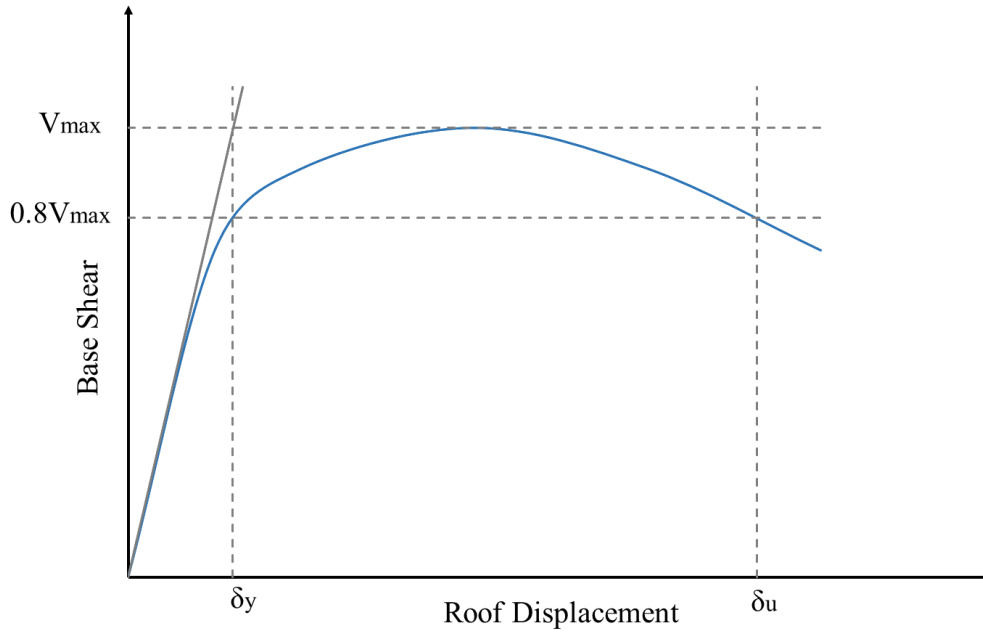


Figure 21: Idealized pushover curve of base shear versus roof displacement - FEMA P-695 methodology [17]

Pushover analysis is performed to validate the model and define the maximum base shear capacity, V_{max} , and the ultimate roof displacement, δ_u , which is defined to occur at the point of 20% strength loss; see Figure 21. Consequently, these parameters are used to calculate the overstrength factor, Ω , defined as:

$$\Omega = V_{max}/V, \quad (52)$$

where V is the design base shear calculated following ASCE 7-10 [21],

$$V = C_s W, \quad (53)$$

where C_s is the seismic response coefficient determined in accordance with ASCE 7-10 Section 12.8.1.1 and W is the effective seismic weight of half the building. To calculate C_s , the response modification factor, R , is taken as 3 for ordinary moment frames and the importance factor, I_e , is taken as 1 for residential buildings [17, 51].

The pushover parameters are also used to calculate period-based ductility defined as the ratio of ultimate roof drift displacement δ_u to the yield displacement δ_y :

$$\mu_T = \delta_u / \delta_y \quad (54)$$

where δ_y is the effective yield roof drift and is calculated as

$$\delta_y = C_o \frac{V_{max}}{W} \left[\frac{g}{4\pi^2} \right] (\max(T, T_1))^2 \quad (55)$$

where C_o relates the displacement of the SDOF corresponding to the fundamental mode to the roof displacement of the MDOF structure [22], V_{max}/W is the maximum base shear normalized by the weight of the modeled building, g is the gravitational constant, T is the code-calculated fundamental period, and T_1 is the fundamental period calculated from eigenvalue analysis.

C. Non-Linear Incremental Dynamic Analysis

Non-linear incremental dynamic analysis (IDA) is then conducted following the methodology proposed by Vamvatsikos and Cornell [18]. Due to the lack of strong recorded ground motions in the area, the FEMA P-695 Far-Field ground motion set that is composed of 22 pairs of horizontal records is used. The 5% damped spectral acceleration at the fundamental period $S_a(T)$ is selected as the IM following the FEMA P-695 [17] methodology for collapse assessment of buildings and because its scalable and generally found to be efficient [52].

First, each ground motion is normalized by a normalization factor, NM , to remove unwarranted variability between records due to inherent differences in magnitude, source type, distance to source, and site conditions. The normalization factors for the Far Field ground motion set are provided in FEMA P-695 [17]. Then, each ground motion is scaled by a scale factor, SF , to achieve a specified median spectral acceleration at the fundamental period of the analyzed building. As shown in Figure 22, each ground motion is scaled at specified increments of $S_a(T)$ until collapse is detected (or until difficulties in achieving convergence are encountered). Each point represents the result of one non-linear dynamic analysis to one ground motion scaled to one seismic intensity level. The IDA analysis is repeated for each of the 44 ground motions in the FEMA P-695 Far-Field ground motion set. This so-called multi-IDA (MIDA) results in 44 IDA curves for each building.

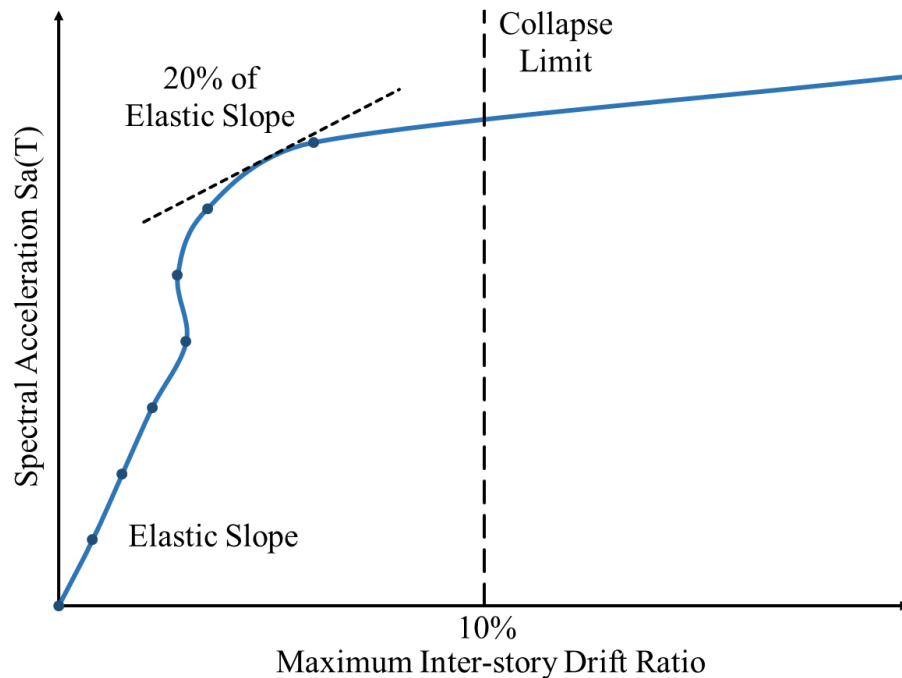


Figure 22: Incremental dynamic analysis - Vamvatsikos and Cornell [18]

Collapse due to a specified ground motion is identified either directly from the dynamic analysis results, or through post-processing. Seismically designed buildings tend to fail in a side-sway collapse mode, which occurs when the inter-story drift ratio in any story increases without bounds, defined by Vamvatsikos and Cornell [18] as dynamic instability. This collapse mode is defined to occur when the maximum inter-story drift ratio exceeds a specified threshold, for example 10%, or when the slope of the IDA curve reaches 20% of the elastic slope [18].

For non-ductile buildings, however, other modes of collapse should be considered. Following Sattar and Liel [14] and Baradaran Shoraka *et al.* [53], two collapse modes are considered for the buildings in this study: global lateral collapse and global gravity collapse. Global lateral collapse occurs when the shear capacity of a story degrades to less than 40% of the story's maximum capacity, computed as the summation of the maximum lateral strength of all columns in the story [14]. During time history analysis, the shear capacity of a story is traced by adding the time varying shear capacity of columns in that story. The column shear capacity is taken as the minimum shear values determined from equations (15) and (16). The selection of 40% of the maximum shear capacity is arbitrary and the collapse fragility results are not sensitive to this value [14]. Global gravity collapse (or axial failure) occurs when the axial demand in any story exceeds the axial capacity, calculated through equation (18). The axial demand is computed by adding the axial forces in a story from expected dead and live loads and is assumed constant throughout the analysis.

D. Fragility Analysis & Performance Evaluation

The results of the MIDA are used to fit a lognormal collapse fragility function which relates the ground motion intensity to the probability of collapse [54]. The fragility curve is defined by two parameters, the median collapse intensity, \hat{S}_{CT} , which represents a collapse probability of 50% and the logarithmic standard deviation of the collapse intensity, β_{RTR} , representing the dispersion in results due to record-to-record variability. Figure 23 shows an example of a collapse fragility curve.

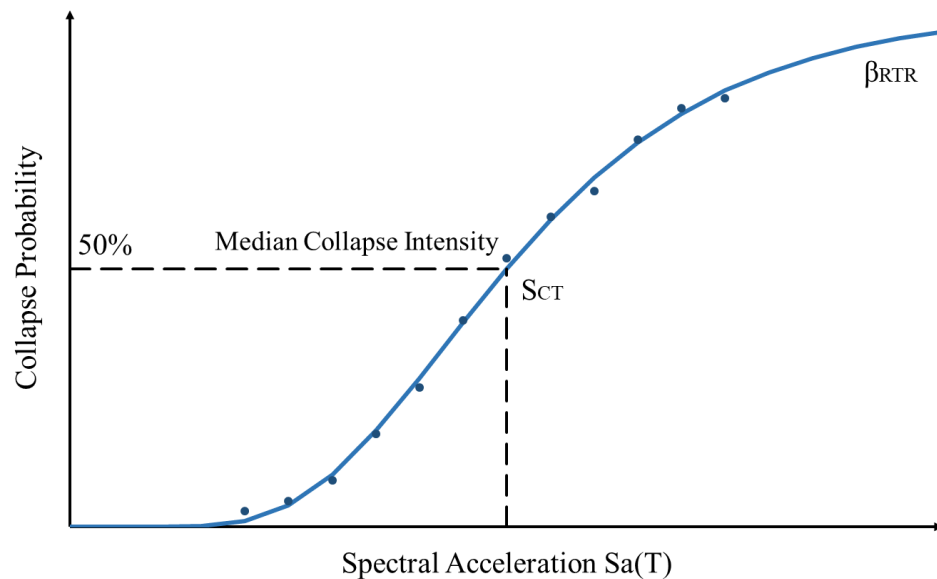


Figure 23: Collapse fragility curve - FEMA P-695 methodology [17]

It is important to include all significant sources of uncertainty that are expected to contribute in estimating the collapse capacity [17]. Main sources of uncertainty to be considered in the collapse assessment are:

- Record to Record Uncertainty (*RTR*), due to the variability of the building response due to the input ground motions used in the analysis.

- Design Requirements Uncertainty (*DR*), related to the quality of design requirements and the extent to which they prevent brittle failure.
- Test Data Uncertainty (*TD*), related to the reliability of test data used to define the structural system.
- Modeling Uncertainty (*MDL*), related to the extent to which the structural model utilizes design parameters to represent structural response and how well it captures collapse modes.

Following FEMA P-695 [17], quantitative values of uncertainty are assigned to design requirements, test data, and modeling uncertainties and are based on their respective quality ratings defined as: (A) Superior $\beta = 0.1$; (B) Good $\beta = 0.2$; (C) Fair $\beta = 0.35$; and (D) Poor $\beta = 0.5$. Total system uncertainty is determined by combining all types of uncertainties, which are assumed to be statistically independent. Therefore, the total lognormal standard deviation, β_{TOT} , accounting for the total uncertainty can be calculated as:

$$\beta_{TOT} = \sqrt{\beta_{RTR}^2 + \beta_{DR}^2 + \beta_{TD}^2 + \beta_{MDL}^2} \quad (56)$$

Accounting for the total system uncertainty flattens the fragility curve fitted from the results of the MIDA analysis, as observed in Figure 24.

The performance of each building is evaluated by calculating the probability of collapse at the MCE intensity, S_{MT} , taking into consideration the total uncertainty. FEMA P-695 [17] suggests a probability of collapse less than or equal to approximately 20% under the maximum considered earthquake as acceptable performance for any building

archetype (and less than or equal to approximately 10% on average across a performance group).

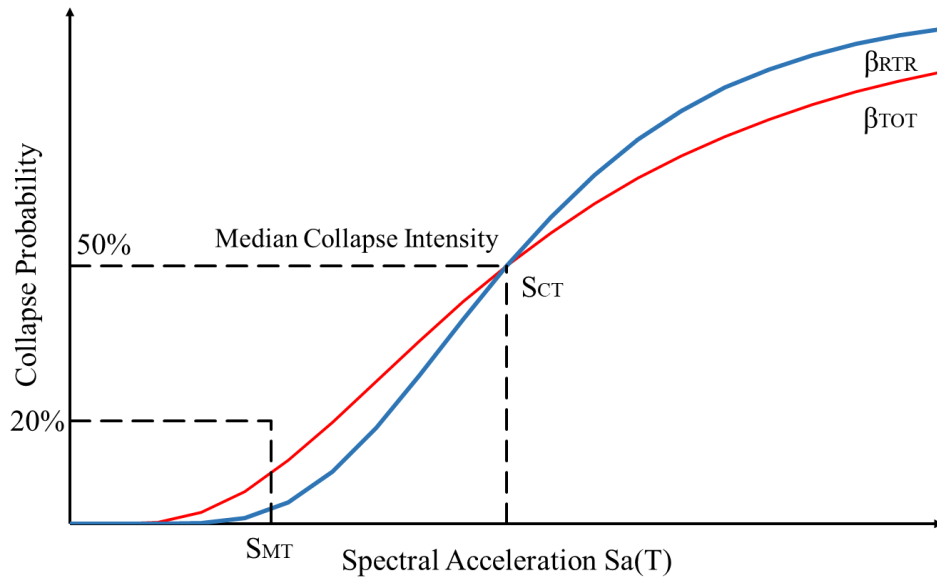


Figure 24: Collapse Fragility for RTR and Total Uncertainty - FEMA P-695 methodology [17]

CHAPTER VI
NONLINEAR STRUCTURAL ANALYSIS, FRAGILITY
ANALYSIS, AND COLLAPSE PERFORMANCE ASSESSMENT:
RESULTS

A. Seismic Hazard at the Site

To characterize the seismic hazard at the building site, results of a study by Huijer *et al.* [1] are used. They performed a probabilistic seismic hazard analysis of Lebanon and characterized the response spectrum of the maximum considered earthquake (MCE), which corresponds to a 2% probability of exceedance in 50 years. For Beirut, the mapped spectral acceleration coefficients are $S_s = 1.45g$ and $S_1 = 0.45g$ and the spectral intensities corresponding to the maximum considered earthquake (MCE) at a class D site are $S_{MS} = 1.45g$ at short periods and $S_{M1} = 0.675g$ at 1 s [1].

Following FEMA P-695 [17] and ASCE 7-10 [21], the fundamental period, T , for each building is calculated as follows:

$$T = C_u T_a = C_u C_t h_n^x, \quad (57)$$

where h_n is the height of the building, C_u is the coefficient for the upper period limit, and C_t and x are approximate period parameters. The fundamental period of all buildings along with spectral acceleration at the maximum considered earthquake, calculated as $S_{MT} = S_{M1}/T$ for this range of building periods, are shown in Table 17. The fundamental

periods calculated from eigenvalue analysis and denoted T_1 are also listed in Table 17 for reference, but the periods T calculated from Equation (57) are used to scale the ground motions in IDA and to calculate S_{MT} .

Table 17: Building height, fundamental periods, spectral intensity at MCE earthquake, and seismic weight

Building Model	Building Height h_n (m)	Code-calculated Fundamental Period T (sec)	Eigenvalue-based Fundamental Period T_1 (sec)	S_{MT} (g)	Seismic Weight W (KN)
4-Story Building	12.8	0.647	2.280	1.043	7207
8-Story Building	25.6	1.208	4.601	0.558	14558
12-Story Building	38.4	1.747	8.170	0.387	21837

B. Non-Linear Analysis Results

The methodology presented in the previous Chapter is applied to the buildings considered in this study. Figure 25 shows the pushover curves for the 4-, 8-, and 12-story buildings normalized by the effective seismic weight W of each building model (i.e., corresponding to half the building). Values of W are provided in Table 17.

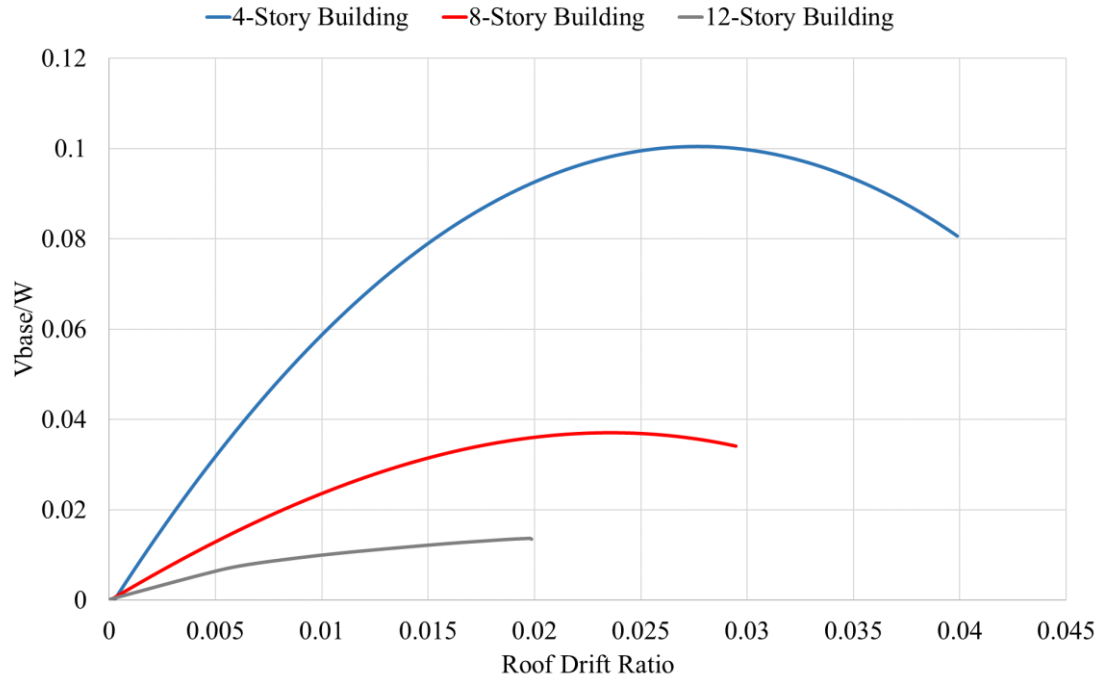


Figure 25: Pushover analysis results of 4-, 8-, and 12-story buildings

Table 18: Pushover analysis parameters of all buildings

Building Model	V (KN)	V_{max} (KN)	Ω	δ_y (m)	δ_u (m)	μ_T
4-Story Building	1660 (0.230W)	721 (0.100W)	0.44	$0.012h_4$	$0.04h_4$	3.1
8-Story Building	1810 (0.124W)	540 (0.037W)	0.30	$0.011h_8$	$0.03h_8$	2.7
12-Story Building	1880 (0.086W)	327 (0.015W)	0.18	$0.009h_{12}$	$0.02h_{12}$	2.2

Table 18 shows the results of the pushover analysis of the 4-, 8-, and 12-story buildings. Note that for the 8- and 12-story buildings, δ_u is defined as the maximum roof drift reached before the models stops converging. The results indicate that the ductility capacity of the buildings decreases as the building height increases. These results are expected due to the increased P-delta effect in taller buildings, which results in an increased strength loss and accelerated failure [6]. Table 18 also shows that the overstrength factor,

Ω , decreases with building height. As expected, all buildings have $\Omega < 1$ and thus do not satisfy seismic design strength requirements.

Following pushover analysis, incremental dynamic analysis is conducted using FEMA's Far Field ground motion set. Each ground motion is gradually scaled to specified values of $S_a(T)$, starting from $0.1g$, $0.05g$, and $0.0125g$ and up to maximum values of $2.0g$, $1.0g$, and $0.5g$ for the 4-, 8- and 12-story buildings, respectively. Each ground motion is scaled until collapse is identified or until convergence problems are encountered. The corresponding scale factors applied across all buildings and all records are all less than or equal to 8, which is less than the recommended maximum value of 10 [55].

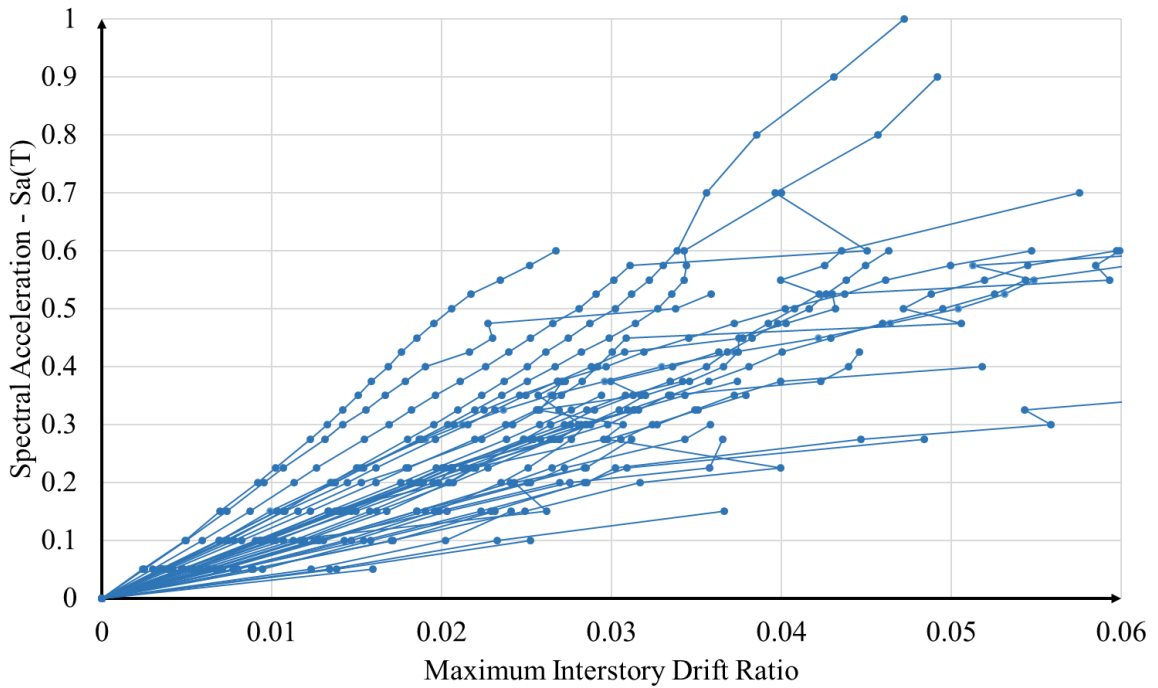


Figure 26: MIDA results of the 8-story building

Figure 26 shows the MIDA results of the 8-story building. Results for the 4- and 12- story buildings are presented in Appendix C. Evidence from analysis results indicate that the dominating mode of failure for all building is global lateral collapse. Median IDR values at collapse are 3.9%, 3.7%, and 3.4% for the 4-, 8-, and 12-story buildings respectively, well below the 10% limit typically set for ductile buildings.

The IDR values for one ground motion scaled to increasing values of $S_a(T)$ are shown in Figure 27 for the 8-story building. As expected, the building responds in the linear range at low spectral intensity values. However, as the intensity increases, exterior and corner joints start to yield. Then, the interior joints start to yield, and the exterior and corner joints begin reaching their ultimate capacities. At an intensity of $0.375g$, the IDR at the top story reaches a value of 4.25%, which reduces the shear capacity of the 8th story columns and causes global lateral collapse in this story. At this intensity, not only most of the exterior joints in the building have reached their ultimate capacities, but also the interior joints at the 7th and 8th floor. The failure of these joints explains the large observed IDR value. In addition, most of the interior joints at the 6th floor yield and thus a large IDR value is also observed at the 7th floor.

The increased drift in the top story causes both the shear and axial capacity of the top story columns to degrade. However, the initial axial load ratio is low in the top story columns, and the reduced axial capacity remains larger than the axial demand. On the other hand, because the building is not designed to resist lateral forces, the large drift decreases the shear capacity of the columns and causes global lateral collapse before global gravity collapse.

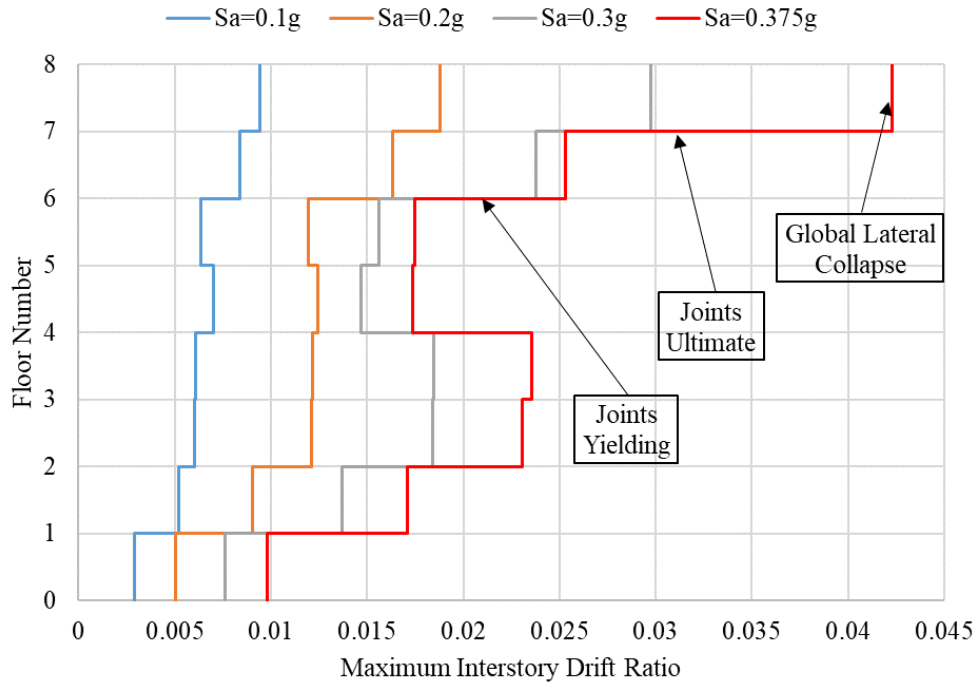


Figure 27: Maximum IDR at each floor for one ground motion scaled to different intensity levels

Damage analysis indicates a similar collapse mode for all ground motions for the 4-, 8-, and 12-story buildings. Joints, mainly the exterior and corner ones, fail prematurely and before beams and columns reach their ultimate capacities. The early failure of these joints is expected as they are confined by less frame elements and have smaller beams and columns framing into them. The failure of joints causes additional story drifts, which leads to a decrease in shear capacity and eventual global lateral collapse. Global lateral collapse occurs at floors 2 to 4, 3 to 8, and 5 to 12 for the 4-, 8-, and 12-story buildings respectively, with the top floor being the most frequent location.

The roof drift ratio (RDR) at which collapse occurs is recorded for each ground motion. The mean RDR values at global lateral collapse are 0.026, 0.017, and 0.007 for the 4-, 8-, and 12-story buildings, respectively, and they decrease as the building height

increases. For the 4- and 8-story buildings, these RDR values are consistent with the RDR values at which the corresponding pushover curves plotted in Figure 25 start having a negative slope indicating the initiation of static instability [25]. However, the difference in RDR values at the onset of lateral instability between the static pushover and dynamic analysis results is large for the 12-story building. This is mainly attributed to the higher mode effects in dynamic analysis, which are prominent for taller buildings.

The next step in the assessment process after estimating all collapse points is to fit the parameters of the lognormal fragility curve. The maximum likelihood method is used in this study because it does not require scaling of the ground motions all the way to the level at which they all cause collapse, thus reducing computational time and convergence problems [56].

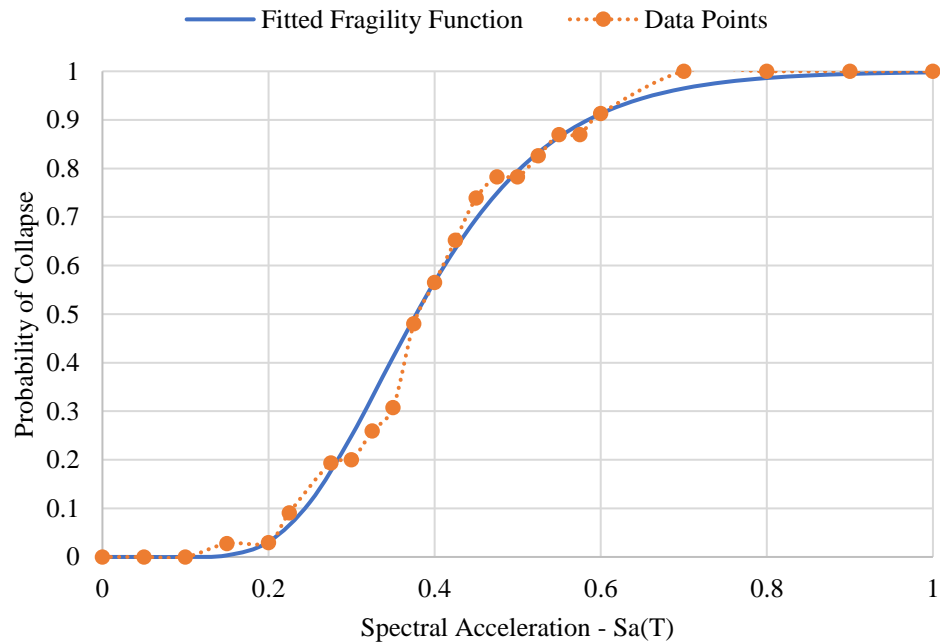


Figure 28: Empirical and fitted fragility function for the 8-story building

Figure 28 shows the plot of the empirical fragility function along with the fitted collapse fragility curve for the 8-story building. Similar plots are presented for 4- and 12-story buildings in Appendix C. The fragility parameters, namely \hat{S}_{CT} and β_{RTR} , are determined by maximizing the following log likelihood function:

$$\{\hat{\mu}, \hat{\beta}\} = \max \sum_{i=1}^m \left\{ \ln \binom{n_i}{z_i} + z_i \ln \phi \left(\frac{\ln x_i - \mu}{\beta} \right) + (n_i - z_i) \ln \left(1 - \phi \left(\frac{\ln x_i - \mu}{\beta} \right) \right) \right\}, \quad (58)$$

where μ and β are the median and standard deviation of $\ln S_a(T)$ at collapse, m is the total number of $S_a(T)$ intensity levels considered, $S_a(T) = x_i$ is the i th intensity level, $i = 1 \dots m$, $\phi(\cdot)$ is the normal cumulative distribution function, n_i is the number of ground motions used at the i th intensity level, and z_i is the number of ground motions that cause collapse at the i th intensity level. The fitted fragility parameters are obtained from $\hat{S}_{CT} = \exp \hat{\mu}$ and $\beta_{RTR} = \hat{\beta}$.

The information on the right-hand side of this formula is all readily available from the IDA results. This formulation does not require multiple observations at each S_a level of interest. A single value of collapse or non-collapse at each given S_a level is still sufficient for fitting (i.e., n_i can be equal to 1 in the above formulas).

Table 19: Fitted fragility curves parameters for the 4-, 8-, and 12-story buildings

Building Model	\hat{S}_{CT} (g)	β_{RTR}	β_{TOT}
4-Story Building	0.938	0.591	0.796
8-Story Building	0.378	0.341	0.633
12-Story Building	0.218	0.359	0.643

Table 19 lists the median collapse intensity and standard deviation for the 4-, 8-, and 12-story buildings. Comparison of the median collapse intensity with the MCE spectral intensity shows that all buildings have $\hat{S}_{CT} < S_{MT}$. Moreover, the performance of the 4-, 8-, and 12-story buildings is evaluated by calculating the probability of collapse under the MCE spectral intensity S_{MT} , and comparing it with the acceptable threshold value taken as 20% in this study.

Figure 29 shows the collapse probability of the 4-, 8-, and 12-story buildings at the MCE spectral intensity. Although the MCE spectral intensities are lower for taller buildings, the collapse probability increases with floor height, reaching a value of 0.57, 0.87, and 0.94 for the 4-, 8-, and 12-story buildings, respectively.

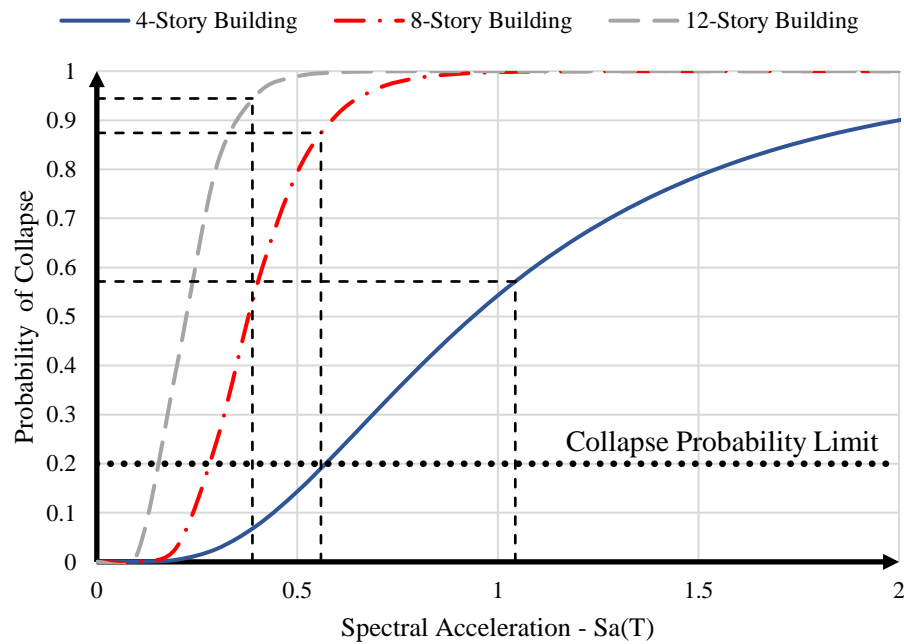


Figure 29: Fitted fragility curves for the 4-, 8-, and 12-story buildings and probability of collapse (horizontal lines) under MCE spectral intensity (vertical lines)

The higher collapse probability in taller buildings is mainly attributed to the increased P-delta effect, which leads to an increased strength loss and accelerated failure. In addition, all buildings greatly exceed the 0.2 collapse probability limit and thus fail the acceptance criteria. Table 20 lists the MCE spectral intensity, fitted fragility parameters, and collapse probability at the MCE spectral intensity, $P_{C,RTR}$, of the 4-, 8-, and 12-story buildings.

Table 20: MCE spectral intensity, fitted median and standard deviation, and collapse probability at MCE for the record to record (RTR) and total (TOT) uncertainty for the 4-, 8-, and 12-story buildings

Building Model	$S_{MT} (g)$	$\hat{S}_{CT} (g)$	β_{RTR}	$P_{C,RTR}$	β_{TOT}	$P_{C,TOT}$
4-Story Building	1.043	0.938	0.437	0.571	0.790	0.553
8-Story Building	0.558	0.378	0.341	0.874	0.633	0.731
12-Story Building	0.387	0.218	0.359	0.944	0.643	0.813

C. Performance Evaluation with Total Uncertainty

Next, additional sources of uncertainty are considered in the collapse assessment process. Following the recommendations of FEMA P-695 [17] for the performance evaluation of ordinary reinforced concrete frames. The ACI 318-95 gravity load design requirements, and not the most recent seismic provisions, are adopted to design the buildings considered in this study. This might result in the occurrence of unanticipated failure modes. Therefore, the design requirements are rated as Fair (C) and β_{DR} is set equal to 0.35. The test data consist of the PEER's Structural Performance Database [30], which includes 255 columns failing in flexure and flexure-shear collapse modes. Although the test data represent a wide range of design configurations and include monotonic and cyclic loading, such columns were not loaded to large deformations where strength loss occurs. In

addition, beams with attached slabs were not tested and only columns were used in the calibration process. Therefore, the quality of the test data is rated as Good (B) and β_{TD} is set equal to 0.2. Modeling uncertainty depends on capturing the true collapse behavior. Although the structural models include shear and axial springs, the models are calibrated to capture shear failure only after flexural yielding occurs. Therefore, and as the shear model is part of ongoing work and requires more data [14], the model quality is rated as Fair (C) and β_{MDL} is set equal to 0.35. The total uncertainty, β_{TOT} , is calculated using equation (56) and the results are shown in Table 19.

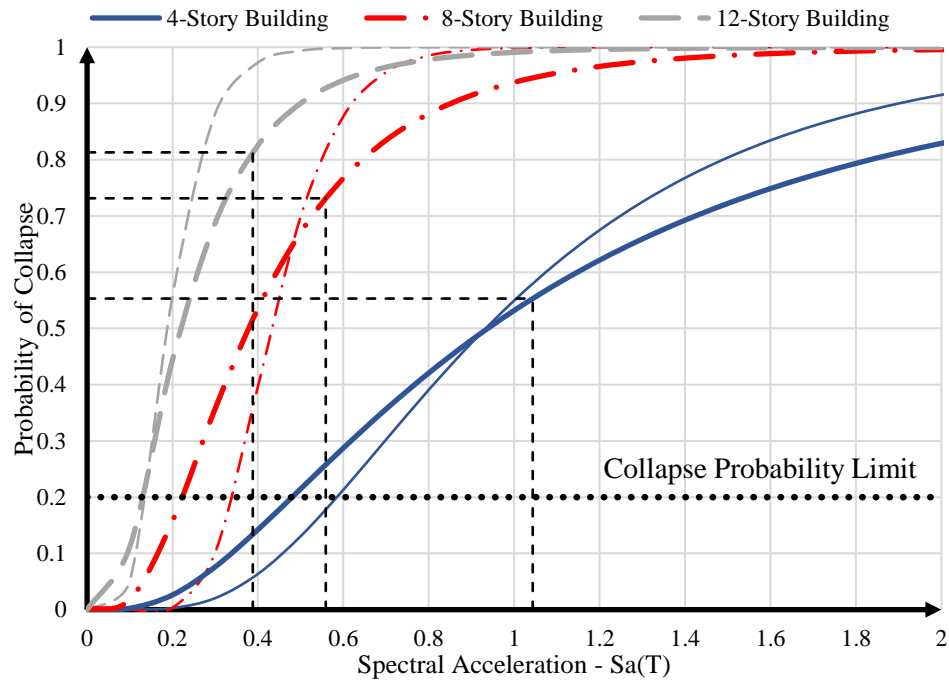


Figure 30: Fitted fragility curves under record to record (thin lines) and total uncertainty (thick lines) for the 4-, 8-, and 12-story buildings and probability of collapse accounting for total uncertainty (horizontal lines) under MCE spectral intensity (vertical lines)

The lognormal collapse fragility curves that account for the total uncertainty are calculated using \hat{S}_{CT} and β_{TOT} for all three buildings. They are plotted in Figure 30 along

with the fragility curves that only account for record-to-record variability. Moreover, the collapse probabilities at the MCE spectral intensity and accounting for the total uncertainty, $P_{C,TOT}$, are listed in Table 20. It can be observed from Figure 30 that the added uncertainty results in a flattening out of the fragility curves, which now show higher probabilities of collapse at intensities below \hat{S}_{CT} and lower probabilities of collapse at intensities above \hat{S}_{CT} . As noted earlier, $S_{MT} > \hat{S}_{CT}$ for the buildings considered in this study. Therefore, when total uncertainty is accounted for, the probability of collapse under the MCE spectral intensity decreases for all three buildings, as can be noted in Table 20, but it remains above the allowable threshold of 0.2.

D. Individual Frame Analysis

In this study, the exterior and interior frames have distinct characteristics. Therefore, both frames are modeled and are combined with rigid links. In fact, the exterior frame has its four interior columns oriented along the longitudinal direction of the frame and its exterior columns oriented in the transverse direction, while all six columns of the interior frame are oriented in the transverse direction. Therefore, the exterior frame is stiffer than the interior frame, and is expected to attract more forces and to fail prematurely due to lack of ductility. As for the interior frame, it has a larger tributary area compared to the exterior frame, but its columns are also larger such that the axial load ratio $P/A_g f'_c$ is mostly consistent between the exterior and interior frames of each building. And while the interior frame is not expected to attract as much lateral forces as the exterior frame, it does

undergo similar lateral displacements. Consequently, the lack of ductility of the interior frame is expected to also contribute to building collapse.

Next, we check whether modeling a single frame is representative and can be used to evaluate the collapse performance of the building, and if so, which one. To do so, each of the interior and exterior frames of the 8-story building is modeled independently. The modeling approach and assumptions explained in the previous chapters are followed. Expected gravity loads, based on the tributary area, are applied directly to each frame. The seismic mass is assigned based on the relative stiffness of the individual frames, calculated by pushover analysis and forcing both frames to the same drift. The results show that the exterior frame of the 8-story building has an initial stiffness that is 1.2 times that of the interior frame. Therefore, to model each frame individually, the seismic weight assigned to the exterior frame is 1.2 times that assigned to the interior frame, such that the exterior frame resists 20% more lateral forces than the interior one. The seismic weight assignments are presented in Table 21.

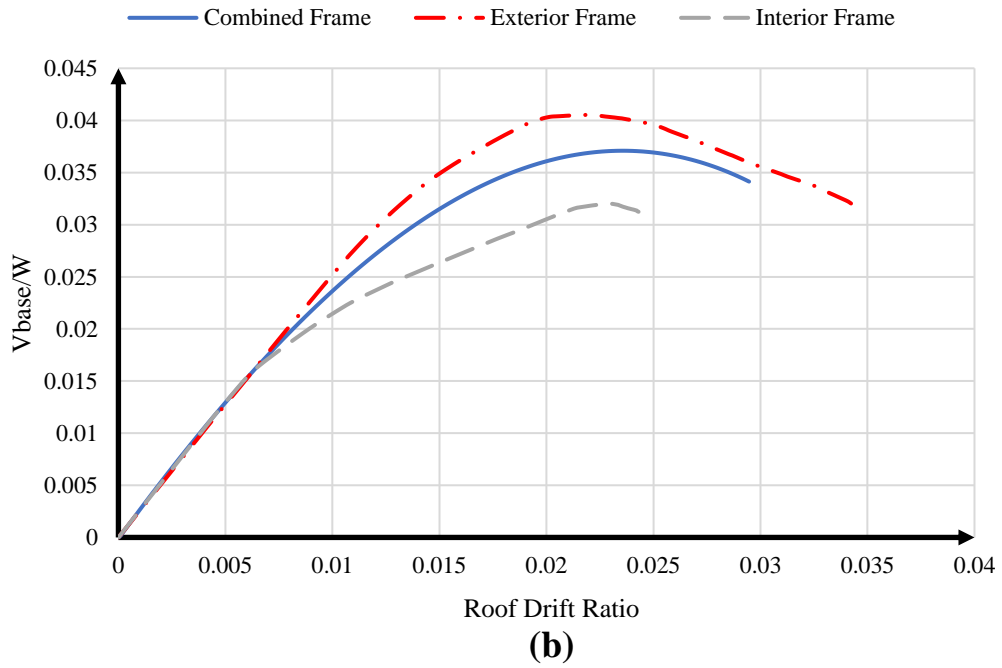
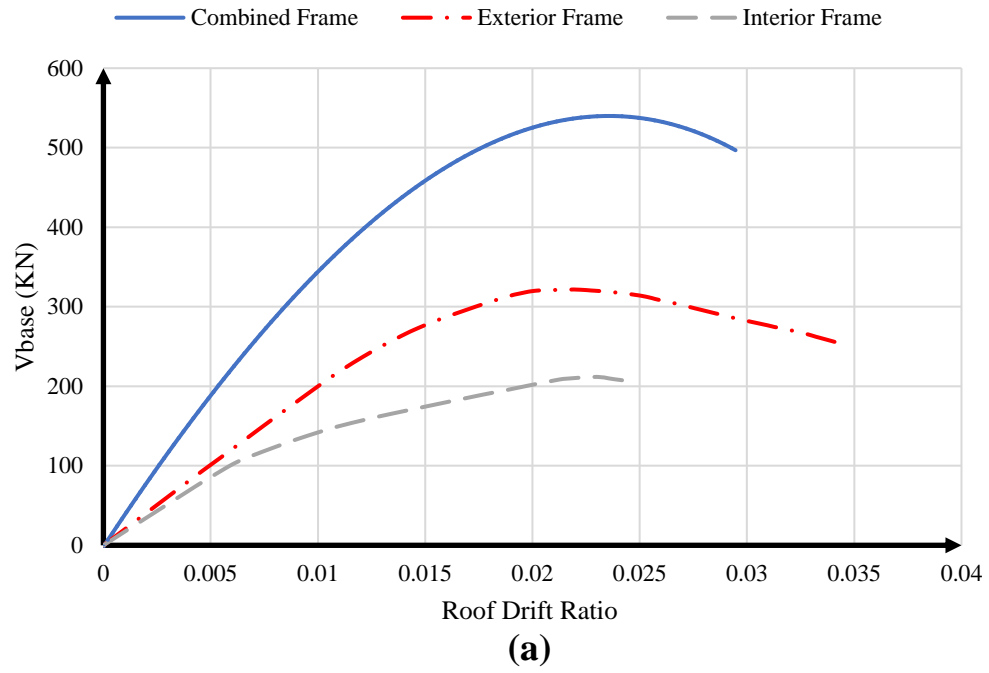


Figure 31: Pushover analysis of the individual and combined frame models of the 8-story building: (a) un-normalized; (b) normalized by their seismic weight.

Figure 31(a) shows the pushover curves of the exterior, interior, and combined frame, while Figure 31(b) shows the same curves, but each normalized by the seismic weight of its corresponding frame. Moreover, the pushover parameters are presented in Table 21. The results indicate that the exterior frame has the highest ductility capacity and the interior has the lowest. The normalized pushover curve of the combined frame falls between those of the individual frames, but slightly closer to the exterior frame, both in terms of strength and ductility.

Table 21: Pushover analysis parameters of individual and combined frame models of the 8-story building

Building Model	Seismic Weight W (KN)	V (KN)	V_{max} (KN)	Ω	$\delta_y(m)$	$\delta_u(m)$	μ_T
8- Combined	14558	1810 (0.12W)	540 (0.037W)	0.30	0.011 h_8	0.030 h_8	2.72
8- Exterior	7935	984 (0.12W)	321 (0.040W)	0.32	0.012 h_8	0.034 h_8	2.83
8- Interior	6614	820 (0.12W)	211 (0.032W)	0.25	0.009 h_8	0.025 h_8	2.50

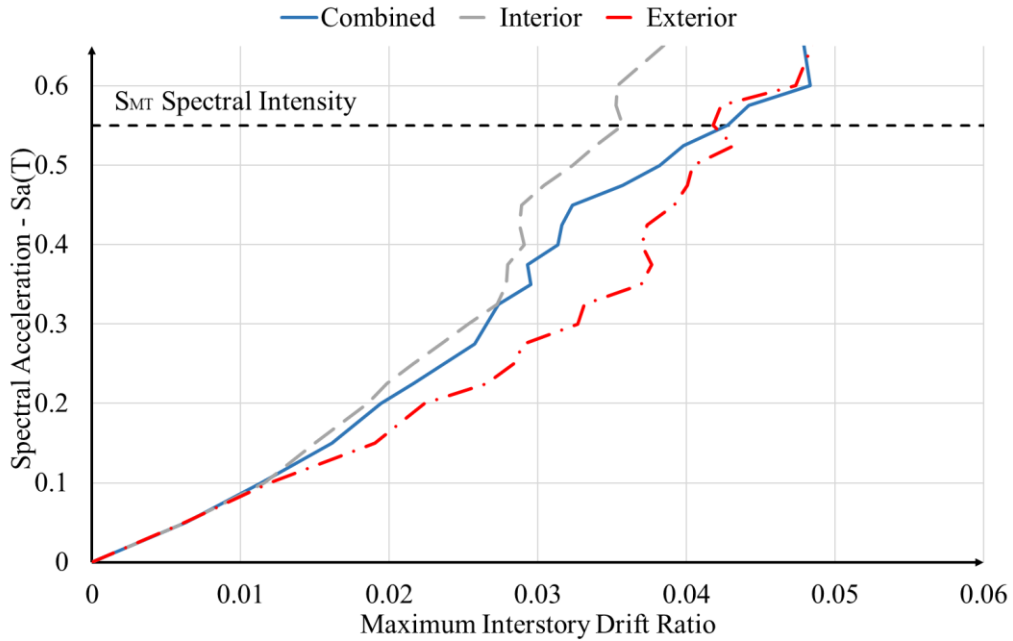


Figure 32: Median MIDA curves for the combined, exterior, and interior frame models of the 8-story building

Next, MIDA analysis is conducted for each frame using similar values of $S_a(T)$. The median MIDA curves are shown in Figure 32. The results show that at spectral intensity levels above $0.1g$, the exterior frame has larger median IDR values compared to the interior one. The median IDR value of the combined frame model falls between those of the interior and exterior frame. At lower intensity levels, the drifts of the combined frame are closer to those of the interior frame. This is mainly attributed to the interaction between the 2 frames and the restraint that the interior frame provides. However, at higher intensity levels, the drifts of the combined frame are closer to those of the exterior frame, with almost equal median IDR value at the MCE spectral intensity. This is mainly attributed to the interior frame sustaining damage at higher intensity values and thus no longer restraining the large IDR values caused by the exterior frame. As a result, the combined frame follows the response of the exterior frame and large IDR values are observed.

Figure 33 shows the maximum IDR values of the individual and combined frames for one ground motion at $S_a(T) = 0.3g$, the collapse spectral intensity of the exterior frame. All three frames show similar IDR values at the lower floors. However, the interior frame shows lower drift values compared to the exterior and combined frames at upper levels. In addition, the combined frame IDR trend follows that of the exterior frame.

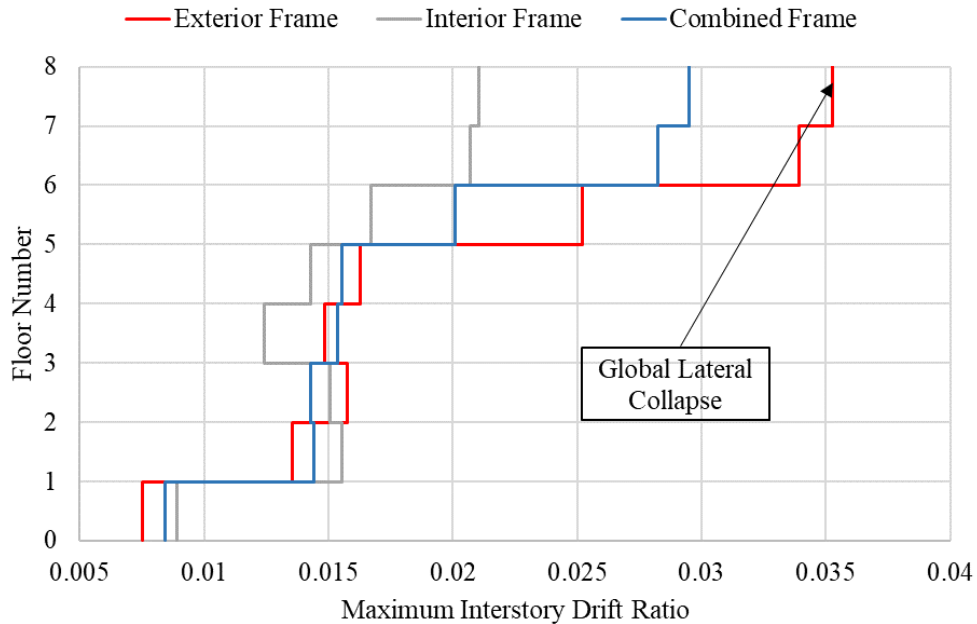


Figure 33: Maximum IDR ratio for the combined, exterior, and interior frame models of the 8-story building for one ground motion at the exterior frame collapse $S_a(T)=0.3g$

Global lateral collapse occurs at the top story of the exterior frame due to the excessive drifts caused by the joints on the 7th and 8th floor reaching their ultimate capacities. The exterior frame of the combined model shows a damage pattern that is similar to that of the individual exterior frame. At the same spectral intensity, however, the interior frame shows lower IDR values and has not reached collapse. This is because only the exterior and corner joints have yielded or failed, while no damage is observed in the interior joints. On the other hand, at the same intensity, all the exterior joints of the interior frame of the combined model have reached their ultimate capacities and its interior joints have yielded. This indicates that the interior frame of the combined model shows more damage than the individual interior frame.

A similar collapse mode is observed for the individual and combined frames for all ground motions, with global lateral collapse occurring and most frequently in the top story. Median IDR values at collapse are 3.7%, 3.8%, and 3.5% for the combined, exterior, and interior frames respectively. The large IDR values observed in the exterior frame is mainly attributed two factors. First, the exterior frame has higher initial stiffness and thus attracts larger forces compared to the interior frame. Also, the exterior frame has smaller beam and column sections and thus weaker joints. The large forces in addition to the weaker joints lead to larger drift values and eventual collapse at lower intensity values.

The maximum likelihood method is used to fit the fragility curves of the three frame models, which are shown in Figure 34. The results indicate that the interior frame has a lower probability of collapse than the exterior frame at all intensity levels. Moreover, and similar to the MIDA results, at low intensities, the combined frame follows the trend of the interior frame. However, as the earthquake intensity increases, the probability of collapse of the combined frame tends towards that of the exterior frame. The fitted fragility parameters along with the collapse probabilities under record-to-record and total uncertainty are shown in Table 22.

Table 22: MCE spectral intensity, fitted median and standard deviation, and collapse probability for the record to record (RTR) and total (TOT) uncertainty for combined and individual frames

Building Model	$S_{MT} (g)$	$\hat{S}_{CT} (g)$	β_{RTR}	$P_{C,RTR}$	β_{TOT}	$P_{C,TOT}$
8- Combined	0.558	0.378	0.341	0.88	0.633	0.73
8- Exterior	0.558	0.335	0.437	0.88	0.690	0.77
8- Interior	0.558	0.415	0.359	0.79	0.643	0.67

Based on the results presented in this section, it seems that the choice of whether to model the exterior or interior frame to represent the whole building in the longitudinal direction depends on the performance objective. The differences in characteristics between the two frames result in interaction effects that affects the total response of the building. For the collapse assessment of the 8-story building considered in this study, modeling the exterior frame provides a representative but slightly conservative alternative to modeling both frames. Nonetheless, further study is needed to confirm that this applies to other buildings with a similar layout.

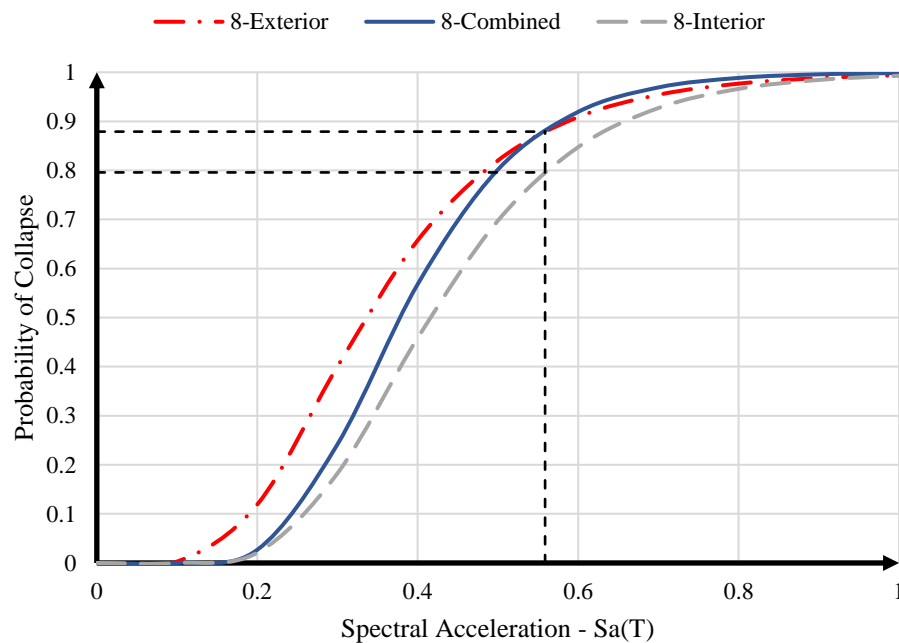


Figure 34: Fitted collapse fragility curves for the exterior, interior, and combined frames

CHAPTER VII

DAMAGE ASSESSMENT AND RETROFITTING

RECOMMENDATIONS

A. Collapse Mechanisms of the Studied Non-Ductile Reinforced Concrete Buildings

Analysis results from the previous chapter indicate that older RC buildings in Beirut are highly vulnerable to collapse at the MCE intensity. Moreover, the collapse mechanisms of the 4-, 8-, and 12-story buildings are similar. Joints, mainly the exterior and corner ones, yield then fail before the beam and column elements framing into them reach their ultimate flexural strength. These results agree with the experimental tests of Elsouiri and Harajli [3]. The yielding and failure of the joints leads to increased story drifts and decreases the shear and axial capacity of the columns, which are designed to resist gravitational loads only, leading to global lateral collapse.

Figure 35 shows the damage patterns of the 4-story building for one ground motion scaled to an intensity that causes collapse. For this ground motion and spectral intensity, shear collapse occurs in the top story. Also, most of the damage is concentrated in the exterior frame because it attracts most of the lateral forces due to its larger stiffness. In addition, the exterior columns of the interior frame show more damage than the interior columns. This can be attributed to the fact that exterior joints are less confined and weaker than interior joints that have the same dimensions. Similar results are observed for the other ground motions at their collapse intensity.

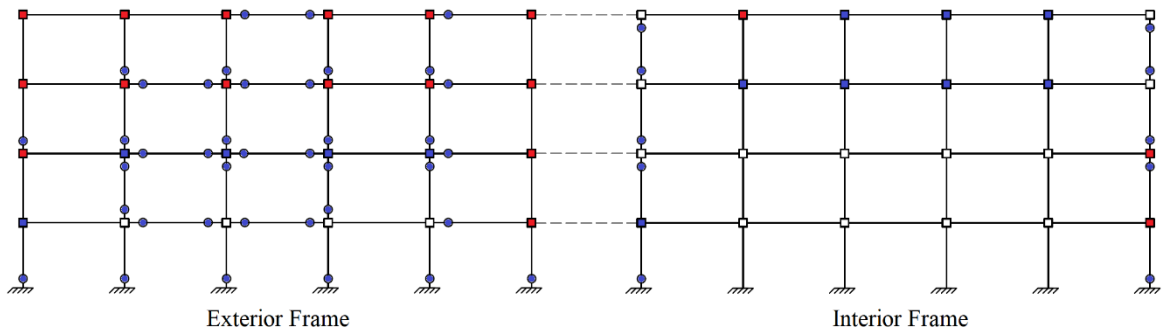


Figure 35: Damage Patterns in the 4-story building at collapse – Yield (Blue) & Ultimate (Red)

Figure 36 and Figure 37 show the damage patterns at collapse of the 8- and 12-story buildings, respectively. These figures indicate that, in both cases, the exterior frame is damaged more than the interior frame, and that damage is concentrated in the upper floors. However, the interior frame of the 8- and 12-story buildings sustain more damage than that of the 4-story building. This can be attributed to the fact that the interior frame in the 8- and 12-story buildings contributes more significantly to lateral resistance than in the 4-story building. In fact, the stiffness of the exterior frame is only 1.2 and 1.1 times that of the interior frame in the 8- and 12-story buildings, versus 1.4 in the 4-story building.

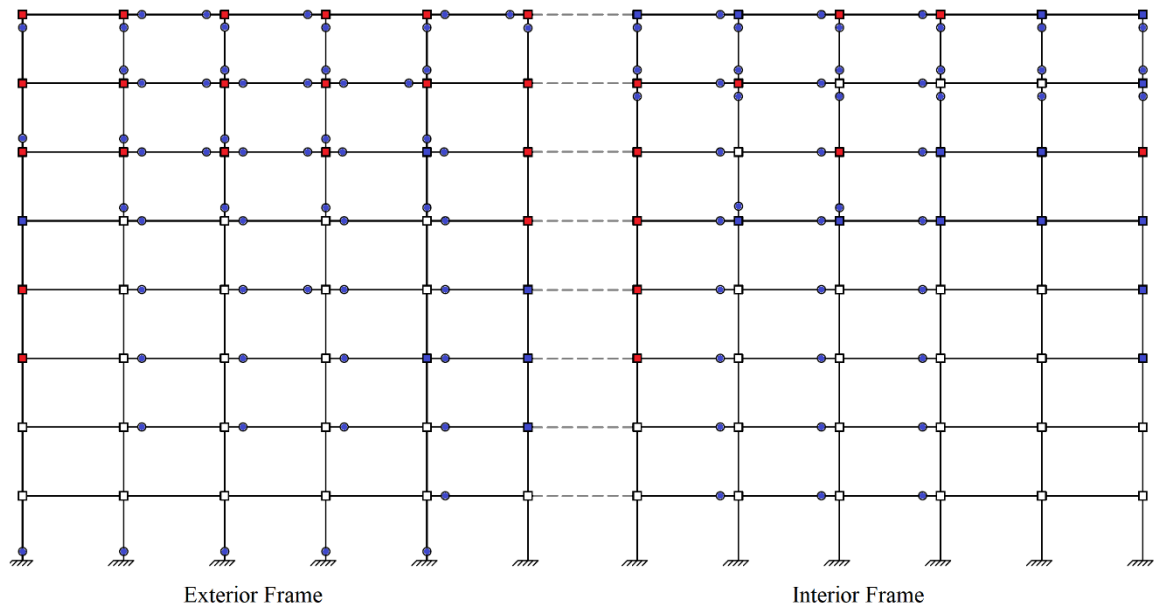


Figure 36: Damage patterns in the 8-story building at collapse – Yield (Blue) & Ultimate (Red)

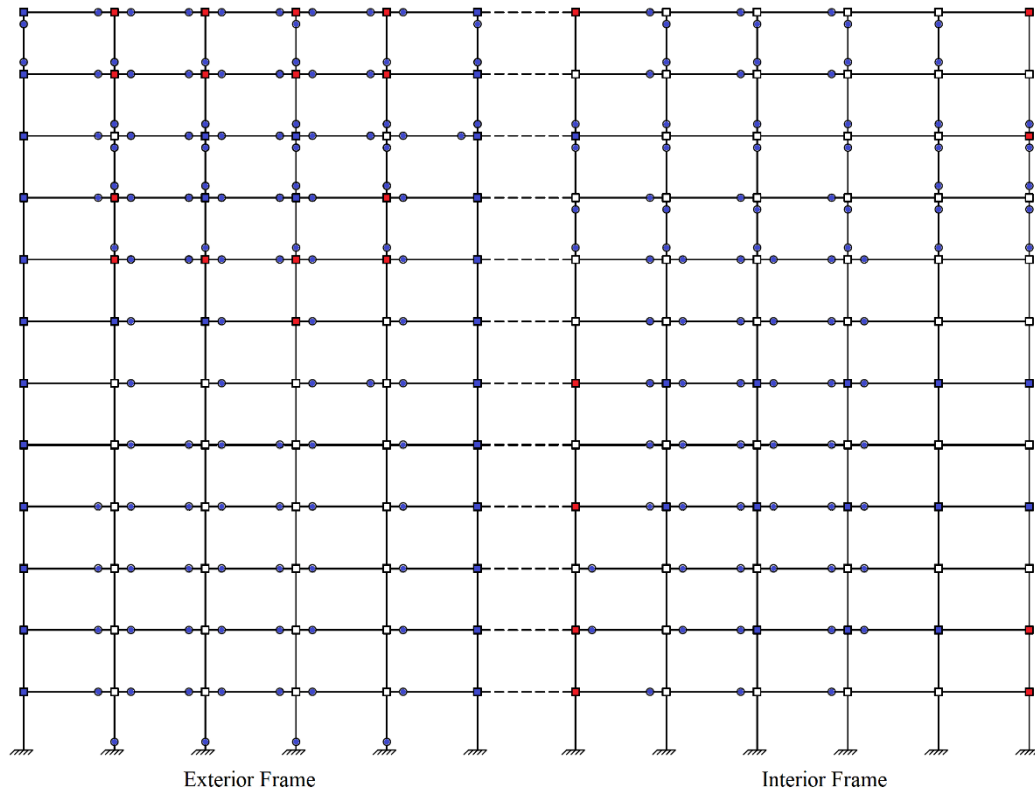


Figure 37: Damage patterns in the 12-story building at collapse – Yield (Blue) & Ultimate (Red)

B. Retrofitting Recommendations

Rehabilitation and retrofitting can play a crucial role in mitigating the collapse risk of the studied buildings. Various retrofitting methods that have been used in practice can be used to enhance the performance and mitigate the seismic hazard posed by non-ductile RC buildings. They include the use of fiber reinforced concrete polymers, constructing new shear walls, and reinforced concrete jacketing [57]. The retrofitting strategy should relate to the seismic deficiencies of such buildings.

Concrete jacketing of the columns, whereby columns are encased by new concrete and reinforcement, is recommended for the studied buildings because it increases the strength, stiffness, and ductility of the jacketed elements. This retrofitting method is appealing because it can remedy some of the problems arising from the poor seismic detailing of older RC buildings, such as inadequate lap splices, weak beam-column joints, and the large aspect ratio of beam and column elements [57].

Retrofits should be used at locations that undergo significant damage and that contribute most to the collapse of the building. Therefore, for the 4-story building, all the columns of the exterior frame along with the exterior columns of the interior frame should be jacketed, as illustrated in Figure 38. The jackets should be used along all the building height.

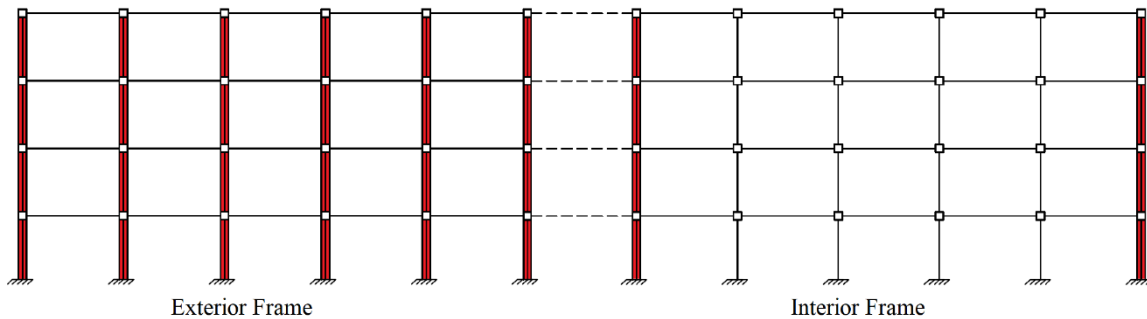


Figure 38: Recommended jacketing locations for the 4-story building

Recommended locations of retrofit for the 8-story building are the exterior columns of the exterior and interior frames, as illustrated in Figure 39. Retrofitting of these exterior columns is expected to delay the failure of their joints. As a result, columns that are susceptible to shear failure, specifically those with high V_p/V_n ratios, could become of main

concern and thus should also be retrofitted. Therefore, the interior columns of the exterior frame over the first four floors should be retrofitted.

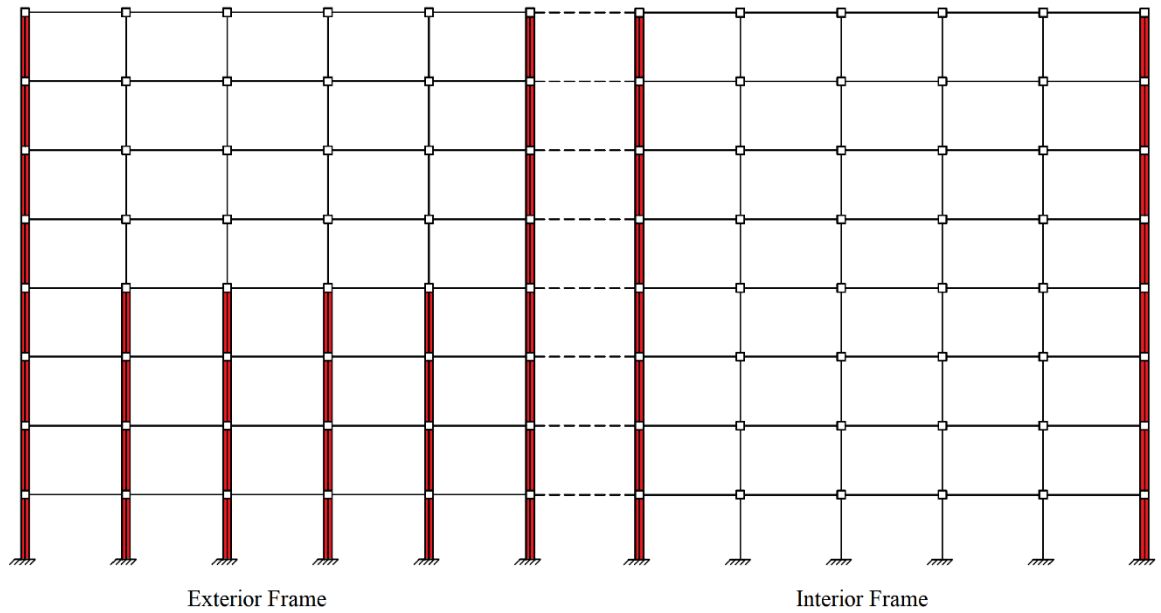


Figure 39: Recommended jacketing locations for the 8-story building

For the 12-story building, the exterior columns of the interior and exterior frames are jacketed, as illustrated in Figure 40. Similarly, columns that are likely to fail in shear should be retrofitted. Therefore, the columns in the first 8 floors of the exterior frame and the first 4 floors of the interior frame are retrofitted.

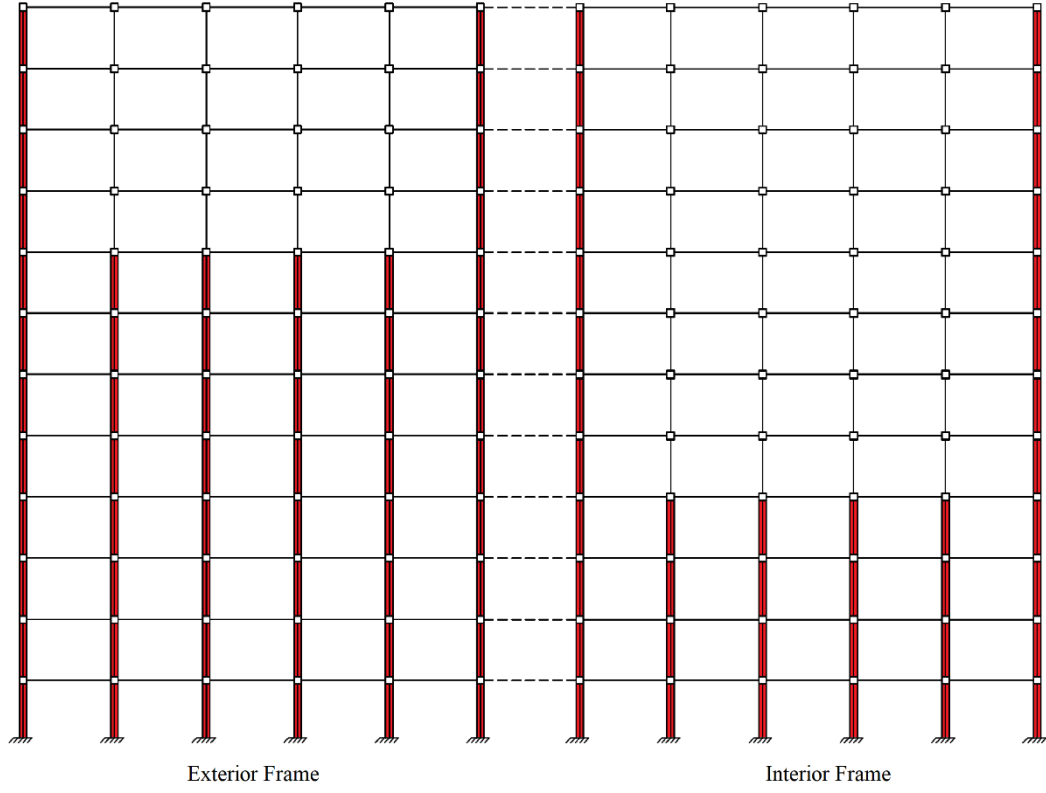


Figure 40: Recommended jacketing locations for the 12-story building

CHAPTER VIII

SUMMARY, CONCLUSIONS, AND RECOMMENDATIONS

A. Summary and Conclusions:

Reinforced concrete buildings constructed in Beirut prior to 2005 lack some important features of good seismic design and impose a significant hazard to life safety. The main objective of this study is to assess the seismic performance of these buildings using the Federal Emergency Management Agency (FEMA) P-695 methodology [17]. To attain this objective, three representative gravity-load designed reinforced concrete buildings that have the same floor plan layout but different number of floors (4, 8 and 12) are designed, their responses to seismic loads are computed and analyzed, and their collapse fragility functions are derived.

First, the three reinforced concrete buildings are designed to resist gravity loads only, following ACI 318-95 [19]. Then, 2D non-linear models of the studied structures are developed with OpenSees in the longitudinal direction only, representing both the exterior and interior frames. The buildings are modeled using the lumped plasticity approach, whereby non-linear concentrated springs are used to represent the various force-deformation relations of the elements. Existing models [7, 29] are used to model the flexural, shear and axial springs of the beam and column elements. To model the response of the joints, the scissors approach proposed by Alath [39] is used. It consists of a single rotational spring located at the center of the joint, with rigid links representing the finite

size of the joint. The joint spring force-deformation relation is typically defined by parameters calibrated to experimental data and that describe the backbone curve and the hysteretic pinching behavior (e.g., [42]). However, such empirical joint models have not been developed for joints having a high aspect ratio, which are typical of the studied buildings. Therefore, new relations are developed in this study to predict the parameters of the joint model for unreinforced wide beam-column joints, by fitting to previous experimental data on similar joint types [3].

After developing the non-linear models, pushover analysis is conducted for each building. Results indicate that, as expected, the buildings do not satisfy seismic design requirements and that the ductility capacity decreases with building height. Incremental dynamic analysis is then conducted using the FEMA P-695 far-field ground motion set, and collapse fragility curves are derived. The probability of collapse at the MCE intensity increases with building height; it is 55, 73, and 81% for the 4-, 8- and 12-story buildings, respectively, when all sources of uncertainty are accounted for. Furthermore, these collapse probabilities largely exceed the allowable limit of 20% set by FEMA P-695 for individual buildings.

Moreover, the progression of damage and the development of the collapse mechanism is tracked for all buildings and ground motions as the ground motion intensity increases. The results indicate that the joints, which are weak and fail before the beams and columns that they connect reach their ultimate capacities, contribute most to the collapse of the studied buildings. The failure of the joints, especially at the top stories, induces large

IDR values, which in turn reduce the shear capacity of the columns in the top stories and result in a global lateral collapse.

In addition, for the 8-story building, the exterior and interior frames are modeled and analyzed separately, and their results are compared with those of the combined frame model. The comparison indicates that the combined frame follows the trend of the interior frame at low spectral intensities. However, at high spectral intensities, the combined frame tends toward the exterior frame, and the collapse probability of the exterior and combined frames at the MCE spectral intensity is similar. Consequently, for the seismic collapse assessment of the 8-story building considered in this study, modeling the exterior frame seems to be sufficient and representative of the total response. Nonetheless, further study is needed to confirm that this applies to other buildings with a similar layout.

Finally, the collapse mechanisms of the 4-, 8-, and 12-story buildings are examined in more detail. The results show that, while for the 4-story building damage is concentrated mostly in the external frame, the damage is spread more uniformly between the exterior and interior frames in the taller buildings. Based on the observed collapse mechanisms, retrofitting schemes are recommended.

B. Limitations and Recommendation for Future Work:

This study has a number of limitations that can be used to offer recommendations for future work, identified as follows:

- The available shear and axial spring models, which are used in this study, are not able to identify collapse during the analysis. Column shear and axial collapse are checked through post-processing. Namely, the shear limit curve proposed by Sezen and Moehle [34] is not included in the shear spring definition.
- The new predictive relations developed in this study for the model parameters of unreinforced wide beam-column joints are based on a limited set of experimental data. More experimental data is necessary to improve the fitting of the model, to better constrain the predictive relations, and to better understand the effects of the joint location and the relative orientation of the beams and columns framing into the joint. In addition, the data may be used to derive a new shear strength equation that better predicts the strength of wide unreinforced beam-column joints.
- Not all the ground motions used are scaled to reach the collapse point. This is mainly attributed to the high computational time and resources required. In addition, difficulties with convergence are encountered, especially with the 12-story building, which is not able to reach large intensity measures due to the complexity of its model. The parameters of the fragility functions are derived based on the available points and using fitting techniques that optimize the results.
- The building is modeled, and its collapse performance is assessed in the longitudinal direction only. However, the performance of the building in the transverse direction, where the structural system is composed of a ribbed slab supported on columns, may be of concern. The building can be modeled in the other direction as well, or a 3-dimensional model of the building may be developed.

- The building models account for the heavy mass of the masonry infill walls, but not for their stiffness. Due to the lack of a lateral force resisting system, such as a shear wall or a moment resisting frame, the infill walls are expected to resist some of the lateral forces and affect the seismic performance of the building. In addition, existing buildings tend to lack of infill walls on the ground floor, which might lead to a soft-story mechanism.
- This study does not assess the performance of the buildings after the implementation of the recommended retrofits. The recommended concrete column jackets should be properly designed and modeled. The analysis performed in this study should be repeated on the retrofitted building, the collapse performance assessed, and the improvement quantified.
- To evaluate whether a mitigating action such as retrofitting is worthwhile, a cost-benefit analysis can be performed, starting from the results of the fragility analysis obtained in this study. The cost-benefit ratio is the cost of building replacement or repair divided by the benefits of improved seismic performance, such as saved lives or reduced building downtime. A cost-benefit ratio that is less than unity indicates that a mitigation action is cost effective. Results of the cost-benefit analysis can be used to help stakeholders and owners determine whether or not to replace or repair non-ductile RC buildings.

BIBLIOGRAPHY

1. Huijjer, C., M. Harajli, and S. Sadek, *Re-evaluation and updating of the seismic hazard of Lebanon*. Journal of Seismology, 2015. **20**(1): p. 233-250.
2. El-Khoury, N.R. and M.H. Harajli, *Seismic Risk Assessment of Existing Building Structures in Lebanon*. 1997.
3. Elsouiri, A. and M. Harajli, *Behavior of Reinforced Concrete Wide Concealed-Beam/Narrow-Column Joints under Lateral Earthquake Loading*. Structural Journal, 2013. **110**: p. 205-215.
4. Celik, O.C. and B.R. Ellingwood, *Modeling Beam-Column Joints in Fragility Assessment of Gravity Load Designed Reinforced Concrete Frames*. Journal of Earthquake Engineering, 2008. **12**(3): p. 357-381.
5. De Risi, M.T., P. Ricci, and G. Verderame. *Influence of joint response in the assessment of seismic performance of existing reinforced concrete frames*. in *COMPADYN 2015, 5th ECCOMAS Thematic Conference on Computational Methods in Structural Dynamics and Earthquake Engineering*. 2015.
6. Galanis, P.H. and J.P. Moehle, *Development of collapse indicators for risk assessment of older-type reinforced concrete buildings*. Earthquake Spectra, 2015. **31**(4): p. 1991-2006.
7. Elwood, K.J., *Modelling failures in existing reinforced concrete columns*. Canadian Journal of Civil Engineering, 2004. **31**(5): p. 846-859.
8. Sattar, S. and A.B. Liel, *Seismic Performance of Nonductile Reinforced Concrete Frames with Masonry Infill Walls—II: Collapse Assessment*. Earthquake Spectra, 2016. **32**(2): p. 819-842.
9. Baradaran Shoraka, M., *Collapse assessment of concrete buildings: an application to non-ductile reinforced concrete moment frames*. 2013, University of British Columbia.
10. Baradaran Shoraka, M. and K. Elwood, *Mechanical model for non ductile reinforced concrete columns*. Journal of Earthquake Engineering, 2013. **17**(7): p. 937-957.
11. Suwal, A., *Evaluation of modeling parameters in ASCE 41-13 for the nonlinear static and dynamic analysis of an RC building*. 2015: The University of Texas at San Antonio.
12. Salameh, C., et al., *Seismic response of Beirut (Lebanon) buildings: instrumental results from ambient vibrations*. Bulletin of Earthquake Engineering, 2016. **14**(10): p. 2705-2730.
13. McKenna, F., G.L. Fenves, and M.H. Scott, *Open system for earthquake engineering simulation*. University of California, Berkeley, CA, 2000.
14. Sattar, S. and A.B. Liel, *Collapse indicators for existing nonductile concrete frame buildings with varying column and frame characteristics*. Engineering Structures, 2017. **152**: p. 188-201.

15. Deierlein, G.G., A.M. Reinhorn, and M.R. Willford, *Nonlinear structural analysis for seismic design*. NEHRP seismic design technical brief, 2010. **4**: p. 1-36.
16. Haselton, C.B., A.B. Liel, and G.G. Deierlein, *Simulating structural collapse due to earthquakes: model idealization, model calibration, and numerical solution algorithms*. Computational Methods in Structural Dynamics and Earthquake Engineering (COMPDYN), 2009.
17. Council, A.T., *Quantification of building seismic performance factors*. 2009: US Department of Homeland Security, FEMA.
18. Vamvatsikos, D. and C.A. Cornell, *Incremental dynamic analysis*. Earthquake Engineering & Structural Dynamics, 2002. **31**(3): p. 491-514.
19. Committee, A.C.I., *Building code requirements for structural concrete : (ACI 318-95) ; and commentary (ACI 318R-95)*. 1995: Farmington Hills, MI : American Concrete Institute, [1995] ©1995.
20. DeBock, D.J., et al., *Importance of seismic design accidental torsion requirements for building collapse capacity*. Earthquake Engineering & Structural Dynamics, 2014. **43**(6): p. 831-850.
21. American Society of Civil Engineers (ASCE), *Minimum design loads for buildings and other structures, ASCE/SEI 7-10*. 2010, ASCE/SEI 7-10.
22. American Society of Civil Engineers (ASCE), *Seismic Evaluation and Retrofit of Existing Buildings, ASCE41-13*. 2014.
23. Haselton, C., et al., *An Assessment to Benchmark the Seismic Performance of a Code-Conforming Reinforced-Concrete Moment-Frame Building*. Pacific Earthquake Engineering Research Center, 2008(2007/1).
24. Fardis, M.N., et al., *Seismic design of concrete buildings to Eurocode 8*. 2015.
25. Galanis, P., *Probabilistic Methods to Identify Seismically Hazardous Older-Type Concrete Frame Buildings*. 2014, UC Berkeley.
26. ASCE, *Seismic rehabilitation of existing buildings*. 2007, ASCE Reston, VA.
27. Ibarra, L.F. and H. Krawinkler, *Global collapse of frame structures under seismic excitations*. 2005.
28. Ibarra, L.F., R.A. Medina, and H. Krawinkler, *Hysteretic models that incorporate strength and stiffness deterioration*. Earthquake engineering & structural dynamics, 2005. **34**(12): p. 1489-1511.
29. B. Haselton, C., et al., *Calibration of Model to Simulate Response of Reinforced Concrete Beam-Columns to Collapse*. ACI Structural Journal, 2016. **113**(6).
30. Berry, M., M. Parrish, and M. Eberhard, *PEER Structural Performance Database, User's Manual (Version 1.0)*. University of California, Berkeley, 2004.
31. Panagiotakos, T.B. and M.N. Fardis, *Deformations of reinforced concrete members at yielding and ultimate*. Structural Journal, 2001. **98**(2): p. 135-148.
32. B. Haselton, C., et al., *Beam-column element model calibrated for predicting flexural response leading to global collapse of RC frame buildings*. 2008, Pacific Earthquake Engineering Research Center: Berkeley, Calif. :.
33. Elwood, K.J. and J.P. Moehle, *Drift capacity of reinforced concrete columns with light transverse reinforcement*. Earthquake Spectra, 2005. **21**(1): p. 71-89.
34. Sezen, H. and J.P. Moehle, *Shear strength model for lightly reinforced concrete columns*. Journal of Structural Engineering, 2004. **130**(11): p. 1692-1703.

35. Elwood, K.J., *Shake table tests and analytical studies on the gravity load collapse of reinforced concrete frames*. 2004.
36. Elwood, K.J. and J.P. Moehle, *Axial capacity model for shear-damaged columns*. ACI Structural Journal-American Concrete Institute, 2005. **102**(4): p. 578-587.
37. Nakamura, T. and M. Yoshimura, *Gravity load collapse of reinforced concrete columns with brittle failure modes*. Journal of Asian Architecture and Building Engineering, 2002. **1**(1): p. 21-27.
38. Kakavand, M.R.A., *Limit state material manual*. 2007, School of Civil Engineering. Tehran, Iran: University of Tehran.
39. Alath, S., *Modeling inelastic shear deformation in reinforced concrete beam-column joints*. 1995.
40. Ellingwood, B.R., O.C. Celik, and K. Kinali, *Fragility assessment of building structural systems in Mid-America*. Earthquake Engineering & Structural Dynamics, 2007. **36**(13): p. 1935-1952.
41. Park, S. and K. Mosalam, *Simulation of Reinforced Concrete Frames with Nonductile Beam-Column Joints*. Earthquake Spectra, 2013. **29**: p. 233-257.
42. Lowes, L.N. and A. Altoontash, *Modeling reinforced-concrete beam-column joints subjected to cyclic loading*. Journal of Structural Engineering, 2003. **129**(12): p. 1686-1697.
43. Elwood, K.J. and J.P. Moehle, *Dynamic collapse analysis for a reinforced concrete frame sustaining shear and axial failures*. Earthquake Engineering & Structural Dynamics, 2008. **37**(7): p. 991-1012.
44. Li, B. and S.A. Kulkarni, *Seismic behavior of reinforced concrete exterior wide beam-column joints*. Journal of structural engineering, 2009. **136**(1): p. 26-36.
45. Quintero-Febres, C.G. and J.K. Wight, *Experimental study of reinforced concrete interior wide beam-column connections subjected to lateral loading*. Structural Journal, 2001. **98**(4): p. 572-582.
46. LaFave, J.M. and J.K. Wight, *Reinforced concrete exterior wide beam-column-slab connections subjected to lateral earthquake loading*. Structural Journal, 1999. **96**(4): p. 577-585.
47. Committee, A. and I.O.f. Standardization. *Building code requirements for structural concrete (ACI 318-08) and commentary*. 2008. American Concrete Institute.
48. Uzumeri, S. *Strength and ductility of cast-in-place beam-column joints*. in *From the American Concrete Institute Annual Convention, Symposium on Reinforced Concrete Structures in Seismic Zones, San Francisco, 1974*. 1977.
49. Hoffman, G., et al., *Gravity-load-designed reinforced concrete buildings: Seismic evaluation of existing construction and detailing strategies for improved seismic resistance*. 1992.
50. Jeon, J.S., A. Shafieezadeh, and R. DesRoches, *Statistical models for shear strength of RC beam-column joints using machine-learning techniques*. Earthquake Engineering & Structural Dynamics, 2014. **43**(14): p. 2075-2095.
51. ASCE, *Minimum Design Loads for Buildings and Other Structures*. Minimum Design Loads for Buildings and Other Structures. 2010.
52. Shome, N., et al., *Earthquake, Records and Nonlinear MDOF Responses*. Vol. 14. 1998. 469-500.

53. Baradaran Shoraka, M., T. Yang, and K. Elwood, *Seismic loss estimation of non-ductile reinforced concrete buildings*. Earthquake Engineering & Structural Dynamics, 2013. **42**(2): p. 297-310.
54. Ibarra, L. *Collapse assessment of deteriorating SDOF systems*. in *Proc. 12th European Conference on Earthquake Engineering, 2002*. 2002.
55. Luco, N. and C.A. Cornell, *Structure-specific scalar intensity measures for near-source and ordinary earthquake ground motions*. Earthquake Spectra, 2007. **23**(2): p. 357-392.
56. Baker, J.W., *Efficient analytical fragility function fitting using dynamic structural analysis*. Earthquake Spectra, 2015. **31**(1): p. 579-599.
57. Liel, A.B. and G.G. Deierlein, *Assessing the collapse risk of California's existing reinforced concrete frame structures: metrics for seismic safety decisions*. Vol. 69. 2008.

APPENDIX A

DESCRIPTION AND DESIGN OF THE BUILDINGS

This section describes the design details of the 4-, 8-, and 12-story reinforced concrete buildings assessed in this study. The design is based on the hypothetical buildings previously developed by El-Khoury and Harajli [2]. Using a similar floor plan and section dimensions, detailed design using ACI 318-95 provisions are developed for all buildings.

A. Design Assumptions:

The structural system represents a 24 cm thick one-way ribbed slab with 150 mm wide ribs spaced at 550 mm. Beams are hidden within the slab and span in the longitudinal direction. Columns span at 5 and 4.5 m in the long and short directions respectively, and the floor height is taken as 3.2 m for all buildings.

1. Applied Loads:

Loads applied represent typical construction practices in Lebanon and are identified as:

- Slab self-weight = 4.1 kN/m^2
- Super imposed dead load = 3.5 kN/m^2
- Live load = 2 kN/m^2

The buildings are designed to resist the ultimate gravity load combination of ACI 318-95 [19] defined as $1.4DL + 1.7LL$. Loads are distributed over the exterior and interior frame based on the tributary area, and are calculated as follows:

- Ultimate Load: $W_u = 1.4DL + 1.7LL = 1.4(3.5 + 4.1) + 1.7(2.0) = 14.04 \text{ KN/m}^2$
- Distributed Total Load for Exterior Frame: $W_{u,E} = [14.04] * 2.25 = 31.59 \text{ KN/m}$
- Distributed Total Load for Interior Frame: $W_{u,I} = [14.04] * 4.50 = 63.18 \text{ KN/m}$

2. Material Properties:

Materials used in design are based on common practices in Lebanon, the nominal concrete and steel material strength are:

- Concrete Compressive Strength: $f'_c = 17.6 \text{ MPa}$
- Steel Reinforcement Yield Strength: $f_y = 420 \text{ MPa}$

3. Design and Strength Requirements:

The buildings are designed to resist gravity loads only, without including lateral forces. Column reinforcements for the 4 and 12-story buildings are shown in Table 23 and Table 24.

Table 23: Column Reinforcement for the 4-Story Building

Exterior Columns of Edge Frame							
Floor	Depth (mm)	Width (mm)	P_u (KN)	Main Reinf.	ρ (%)	Shear Reinf. (mm)	ρ_{sh} (%)
1	200	600	372	8T16	1.33	4T8@200	0.17
2	200	600	279	8T16	1.33	4T8@200	0.17
3	200	600	186	8T16	1.33	4T8@200	0.17
4	200	600	93	8T16	1.33	4T8@200	0.17
Interior Columns of Edge Frame							
Floor	Depth (mm)	Width (mm)	P_u (KN)	Main Reinf.	ρ (%)	Shear Reinf. (mm)	ρ_{sh} (%)
1	700	200	735	8T16	1.14	2T8@200	0.25
2	700	200	551	8T16	1.14	2T8@200	0.25
3	700	200	367	8T16	1.14	2T8@200	0.25
4	700	200	183	8T16	1.14	2T8@200	0.25

Exterior Columns of Interior Frame							
Floor	Depth (mm)	Width (mm)	P_u (KN)	Main Reinf.	ρ (%)	Shear Reinf. (mm)	ρ_{sh} (%)
1	200	700	738	8T16	1.14	4T8@200	0.14
2	200	700	551	8T16	1.14	4T8@200	0.14
3	200	700	367	8T16	1.14	4T8@200	0.14
4	200	700	183	8T16	1.14	4T8@200	0.14
Interior Columns of Interior Frame							
Floor	Depth (mm)	Width (mm)	P_u (KN)	Main Reinf.	ρ (%)	Shear Reinf. (mm)	ρ_{sh} (%)
1	250	700	1425	8T20	1.42	4T8@200	0.14
2	250	700	1068	8T20	1.42	4T8@200	0.14
3	250	700	712	8T20	1.42	4T8@200	0.14
4	250	700	356	8T20	1.42	4T8@200	0.14

Table 24: Column Reinforcement for the 12-Story Building

Exterior Columns of Edge Frame							
Floor	Depth (mm)	Width (mm)	P_u (KN)	Main Reinf.	ρ (%)	Shear Reinf. (mm)	ρ_{sh} (%)
1	200	700	1123	8T22	2.21	4T8@200	0.14
2	200	700	1029	8T22	2.21	4T8@200	0.14
3	200	700	935	8T22	2.21	4T8@200	0.14
4	200	700	842	8T22	2.21	4T8@200	0.14
5	200	700	748	8T20	1.77	4T8@200	0.14
6	200	700	654	8T20	1.77	4T8@200	0.14
7	200	700	560	8T20	1.77	4T8@200	0.14
8	200	700	467	8T20	1.77	4T8@200	0.14
9	200	600	373	8T16	1.33	4T8@200	0.17
10	200	600	280	8T16	1.33	4T8@200	0.17
11	200	600	186	8T16	1.33	4T8@200	0.17
12	200	600	93	8T16	1.33	4T8@200	0.17
Interior Columns of Edge Frame							
Floor	Depth (mm)	Width (mm)	P_u (KN)	Main Reinf.	ρ (%)	Shear Reinf. (mm)	ρ_{sh} (%)
1	800	250	2658	12T22	2.32	4T8@250	0.2
2	800	250	2436	12T22	2.32	4T8@250	0.2
3	800	250	2213	12T22	2.32	4T8@200	0.2
4	800	250	1991	12T22	2.32	4T8@200	0.2
5	800	200	1768	8T22	1.94	4T8@200	0.25

6	800	200	1547	8T22	1.94	4T8@200	0.25
7	800	200	1326	8T22	1.94	4T8@200	0.25
8	800	200	1104	8T22	1.94	4T8@200	0.25
9	700	200	883	8T16	1.14	4T8@200	0.25
10	700	200	662	8T16	1.14	4T8@200	0.25
11	700	200	441	8T16	1.14	4T8@200	0.25
12	700	200	221	8T16	1.14	4T8@200	0.25
Exterior Columns of Interior Frame							
Floor	Depth (mm)	Width (mm)	P_u (KN)	Main Reinf.	ρ (%)	Shear Reinf. (mm)	ρ_{sh} (%)
1	250	800	2658	12T22	2.32	4T8@200	0.12
2	250	800	2436	12T22	2.32	4T8@200	0.12
3	250	800	2213	12T22	2.32	4T8@200	0.12
4	250	800	1991	12T22	2.32	4T8@200	0.12
5	200	800	1768	8T22	1.94	4T8@200	0.12
6	200	800	1547	8T22	1.94	4T8@200	0.12
7	200	800	1326	8T22	1.94	4T8@200	0.12
8	200	800	1104	8T22	1.94	4T8@200	0.12
9	200	700	883	8T16	1.14	4T8@200	0.14
10	200	700	662	8T16	1.14	4T8@200	0.14
11	200	700	441	8T16	1.14	4T8@200	0.14
12	200	700	221	8T16	1.14	4T8@200	0.14
Interior Columns of Interior Frame							
Floor	Depth (mm)	Width (mm)	P_u (KN)	Main Reinf.	ρ (%)	Shear Reinf. (mm)	ρ_{sh} (%)
1	400	1000	5172	22T22	2.13	6T8@250	0.12
2	400	1000	4738	22T22	2.13	6T8@250	0.12
3	400	1000	4304	22T22	2.13	6T8@250	0.12
4	400	1000	3870	22T22	2.13	6T8@250	0.12
5	300	1000	3435	12T22	1.55	6T8@250	0.12
6	300	1000	3004	12T22	1.55	6T8@250	0.12
7	300	1000	2573	12T22	1.55	6T8@250	0.12
8	300	1000	2141	12T22	1.55	6T8@250	0.12
9	250	700	1710	8T20	1.42	4T8@200	0.14
10	250	700	1283	8T20	1.42	4T8@200	0.14
11	250	700	855	8T20	1.42	4T8@200	0.14
12	250	700	428	8T20	1.42	4T8@200	0.14

APPENDIX B

BUILDINGS MODEL PARAMETERS

This section presents the modeling parameters used to define rotational, shear, and axial springs in column elements of the 4 and 12 story buildings and are shown in Table 25 to Table 28.

Table 25: 4-Story Building Exterior Frame Column Modeling Parameters

Shear/Axial Springs									
Floor	Type	$P/A_g f'_c$	M_y (KN.m)	V_p/V_n	EI_{stf}/EI_g	Δ_s/L	Δ_a/L		
1	Interior	0.20	322	0.76	0.42	0.018	0.061		
2	Interior	0.15	291	0.72	0.36	0.020	0.068		
Flexural Springs									
Floor	Type	$P/A_g f'_c$	M_y (KN.m)	V_p/V_n	EI_{stf}/EI_g	M_c/M_y	$\theta_{cap,pl}$ (rad)	θ_{pc} (rad)	λ
1	Exterior	0.12	59	0.41	0.57	1.13	0.037	0.072	9
2	Exterior	0.09	54	0.39	0.51	1.13	0.039	0.047	9
3	Exterior	0.06	50	0.36	0.44	1.13	0.042	0.055	10
	Interior	0.10	261	0.67	0.35	1.13	0.065	0.1	81
4	Exterior	0.03	45	0.33	0.37	1.13	0.044	0.061	10
	Interior	0.05	229	0.62	0.35	1.13	0.072	0.1	87

Table 26: 4-Story Building Interior Frame Column Modeling Parameters

Flexural Springs									
Floor	Type	$P/A_g f'_c$	M_y (KN.m)	V_p/V_n	EI_{stf}/EI_g	M_c/M_y	$\theta_{cap,pl}$	θ_{pc}	λ
1	Exterior	0.19	74	0.48	0.71	1.13	0.031	0.027	8
	Interior	0.30	136	0.59	0.8	1.13	0.025	0.018	12
2	Exterior	0.14	66	0.44	0.61	1.13	0.034	0.034	8
	Interior	0.22	134	0.61	0.7	1.13	0.029	0.024	15
3	Exterior	0.09	58	0.4	0.51	1.13	0.037	0.041	9
	Interior	0.15	123	0.59	0.57	1.13	0.033	0.033	16
4	Exterior	0.04	49	0.35	0.41	1.13	0.04	0.05	10
	Interior	0.07	103	0.52	0.42	1.13	0.035	0.045	18

Table 27: 12-Story Building Exterior Frame Column Modeling Parameters

Shear/Axial Springs									
Floor	Type	$P/A_g f'_c$	M_y (KN.m)	V_p/V_n	EI_{stf}/EI_g	Δ_s/L	Δ_a/L		
1	Interior	0.43	818	0.86	0.63	0.009	0.0543		
2	Interior	0.39	822	0.88	0.59	0.0103	0.0566		
3	Interior	0.35	826	0.9	0.56	0.0117	0.0591		
4	Interior	0.32	831	0.93	0.52	0.0092	0.0618		
5	Interior	0.35	603	0.73	0.55	0.0124	0.0649		
6	Interior	0.31	606	0.75	0.51	0.0141	0.0681		
7	Interior	0.26	611	0.77	0.47	0.0158	0.0717		
8	Interior	0.22	605	0.78	0.42	0.0176	0.0757		
Flexural Springs									
Floor	Type	$P/A_g f'_c$	M_y (KN.m)	V_p/V_n	EI_{stf}/EI_g	M_c/M_y	$\theta_{cap,pl}$	θ_{pc}	λ
1	Exterior	0.32	89	0.56	0.8	1.13	0.0244	0.0163	6
2	Exterior	0.30	89	0.56	0.8	1.13	0.0256	0.0183	6
3	Exterior	0.27	88	0.57	0.8	1.13	0.027	0.0204	7
4	Exterior	0.24	88	0.57	0.8	1.13	0.0284	0.0228	7
5	Exterior	0.21	83	0.54	0.75	1.13	0.0298	0.0255	7
6	Exterior	0.19	82	0.55	0.7	1.13	0.0314	0.0285	8
7	Exterior	0.16	82	0.55	0.65	1.13	0.033	0.0318	8
8	Exterior	0.13	82	0.56	0.59	1.13	0.0347	0.0355	8
9	Exterior	0.12	58	0.42	0.57	1.13	0.0377	0.0422	9
	Interior	0.20	322	0.5	0.42	1.13	0.0546	0.0897	70
10	Exterior	0.09	54	0.39	0.51	1.13	0.0399	0.0473	9
	Interior	0.15	291	0.47	0.36	1.13	0.06	0.1	75
11	Exterior	0.06	49	0.36	0.44	1.13	0.0423	0.0543	10
	Interior	0.10	260	0.43	0.35	1.13	0.0658	0.1	81
12	Exterior	0.03	44	0.33	0.37	1.13	0.0448	0.0616	10
	Interior	0.05	228	0.39	0.35	1.13	0.0722	0.1	87

Table 28: 12-Story Building Interior Frame Column Modeling Parameters

Shear/Axial Springs							
Floor	Type	$P/A_g f'_c$	M_y (KN.m)	V_p/V_n	EI_{stf}/EI_g	Δ_s/L	Δ_a/L
1	Exterior	0.42	183	0.72	0.8	0.0175	0.0235
	Interior	0.41	677	0.97	0.8	0.0148	0.025
2	Exterior	0.38	183	0.73	0.8	0.0185	0.0251
	Interior	0.37	378	0.99	0.77	0.0159	0.0267
3	Exterior	0.35	183	0.74	0.8	0.0195	0.0271

	Interior	0.34	680	1.02	0.73	0.017	0.0288		
4	Exterior	0.31	183	0.75	0.8	0.0212	0.0293		
	Interior	0.30	681	1.04	0.68	0.0181	0.0311		
5	Interior	0.36	307	0.74	0.8	0.0182	0.0265		
6	Interior	0.32	306	0.76	0.78	0.0195	0.0293		
7	Interior	0.26	305	0.78	0.71	0.0208	0.0327		
8	Interior	0.22	304	0.8	0.64	0.022	0.037		
Flexural Springs									
Floor	Type	$P/A_g f'_c$	M_y (KN.m)	V_p/V_n	EI_{stf}/EI_g	M_c/M_y	$\theta_{cap,pl}$	θ_{pc}	λ
5	Exterior	0.34	98	0.58	0.8	1.13	0.022	0.014	6
6	Exterior	0.30	97	0.59	0.8	1.13	0.024	0.016	6
7	Exterior	0.25	97	0.59	0.8	1.13	0.026	0.019	7
8	Exterior	0.21	96	0.6	0.75	1.13	0.028	0.023	7
9	Exterior	0.19	74	0.48	0.71	1.13	0.031	0.028	8
	Interior	0.30	134	0.59	0.8	1.13	0.026	0.018	13
10	Exterior	0.14	66	0.44	0.61	1.13	0.029	0.025	8
	Interior	0.22	134	0.61	0.7	1.13	0.029	0.025	15
11	Exterior	0.09	58	0.4	0.51	1.13	0.037	0.041	9
	Interior	0.15	123	0.59	0.57	1.13	0.034	0.033	16
12	Exterior	0.05	49	0.35	0.41	1.13	0.041	0.05	10
	Interior	0.07	103	0.52	0.42	1.13	0.039	0.045	18

APPENDIX C

STRUCTURAL ANALYSIS RESULTS

This section presents the MIDA curves for the 4-story building, 8-exterior frame, 8-interior frame, and 12-story building, shown in Figure 41 to Figure 44. The results of the empirical and fitted fragility curves are also shown in Figure 45 to Figure 48.

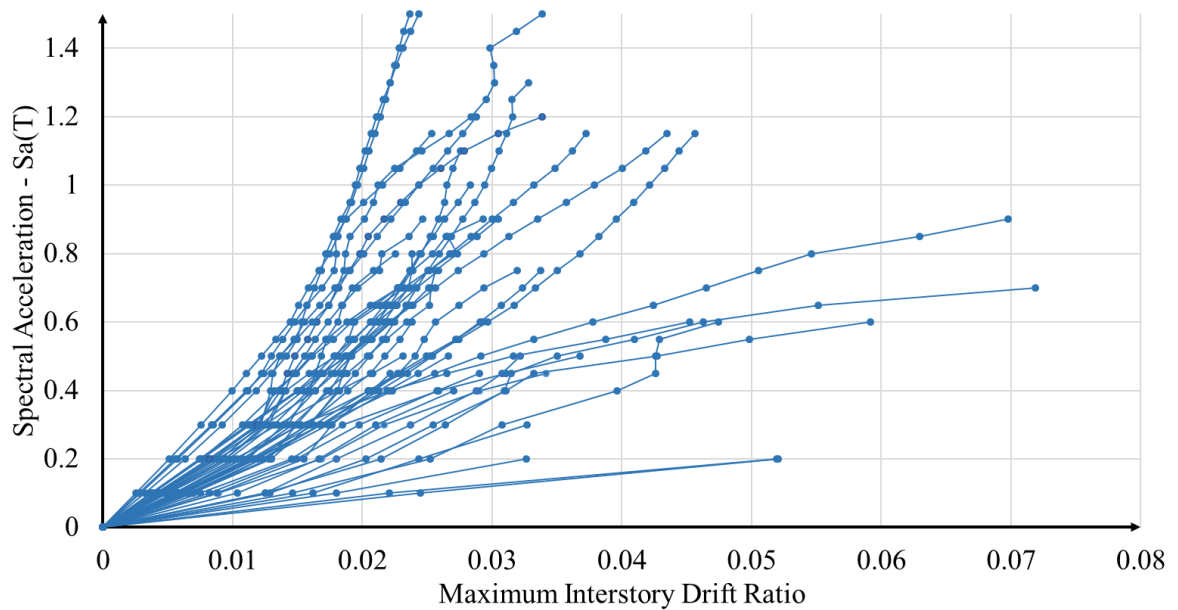


Figure 41: MIDA results of the 4-story building

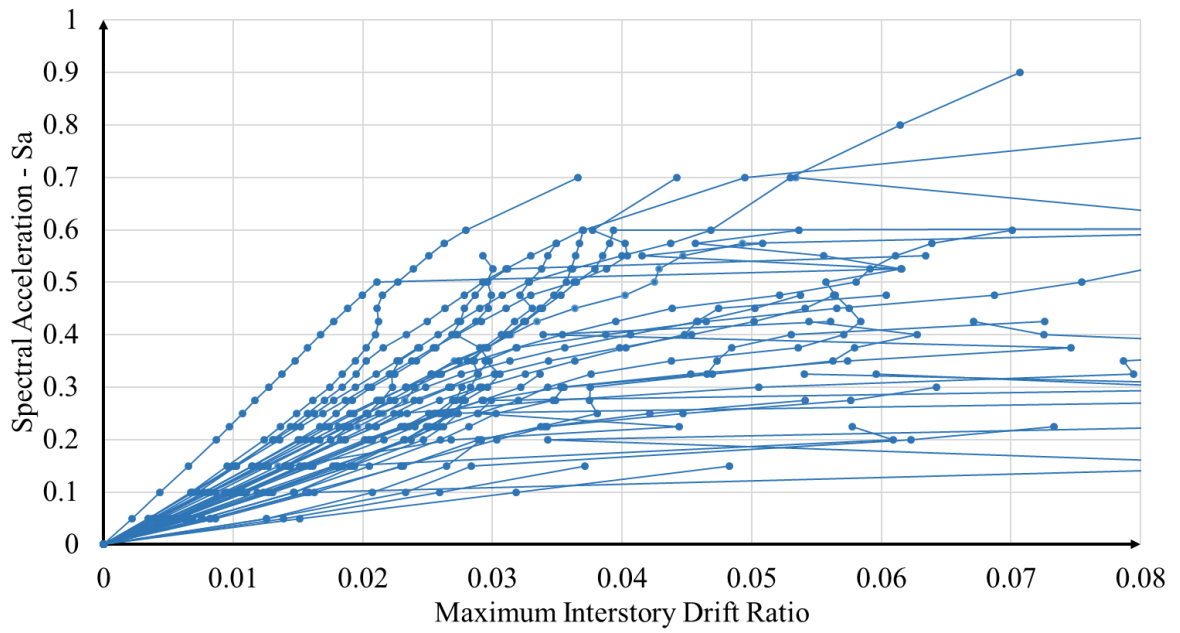


Figure 42: MIDA results of the 8-story exterior frame

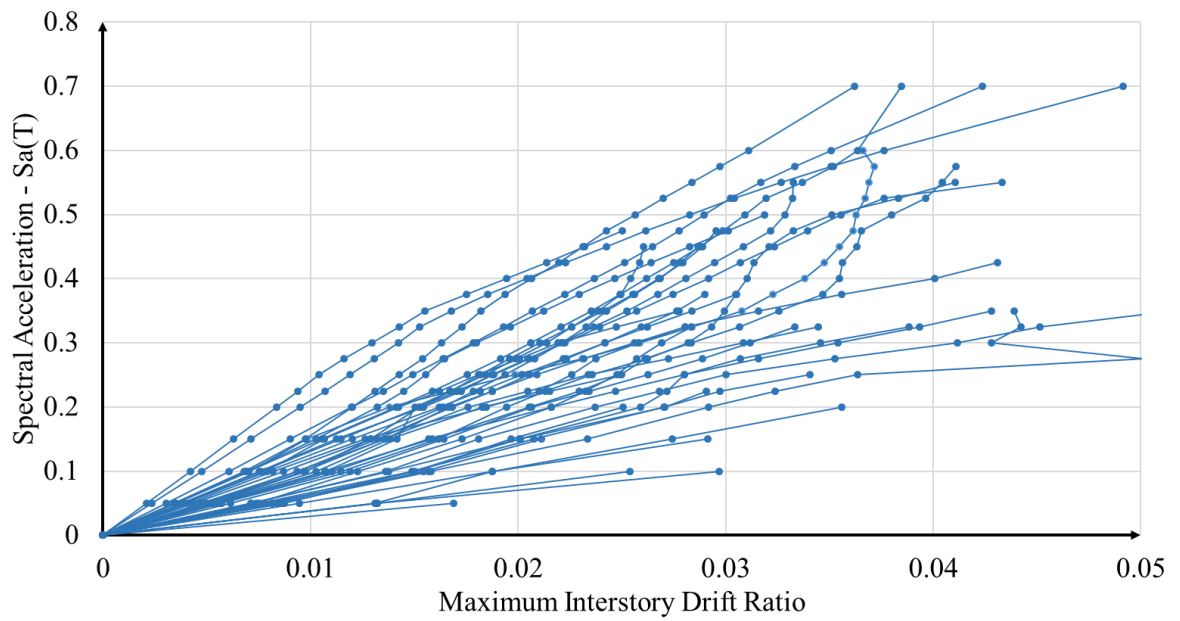


Figure 43: MIDA results of the 8-story interior frame

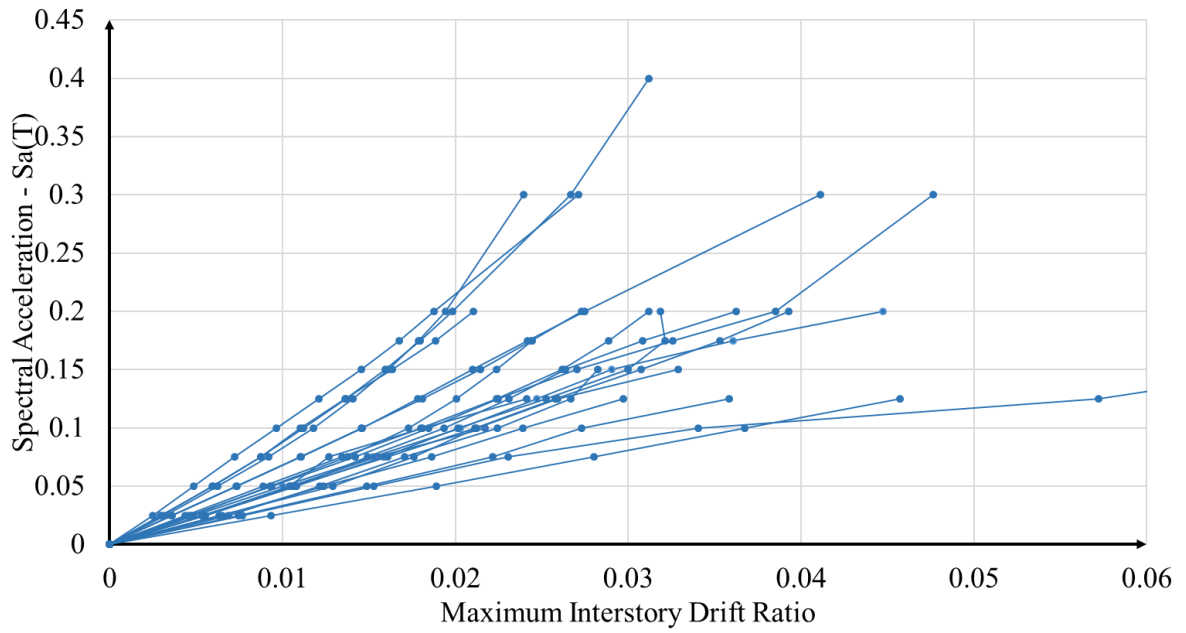


Figure 44: MIDA results of the 12-story building

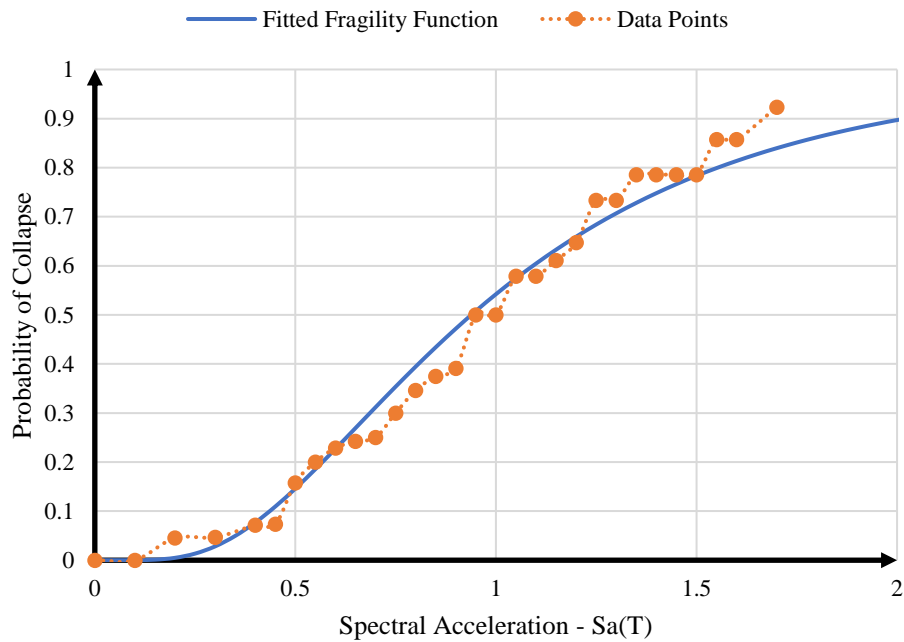


Figure 45: Empirical and fitted fragility function for the 4-story building

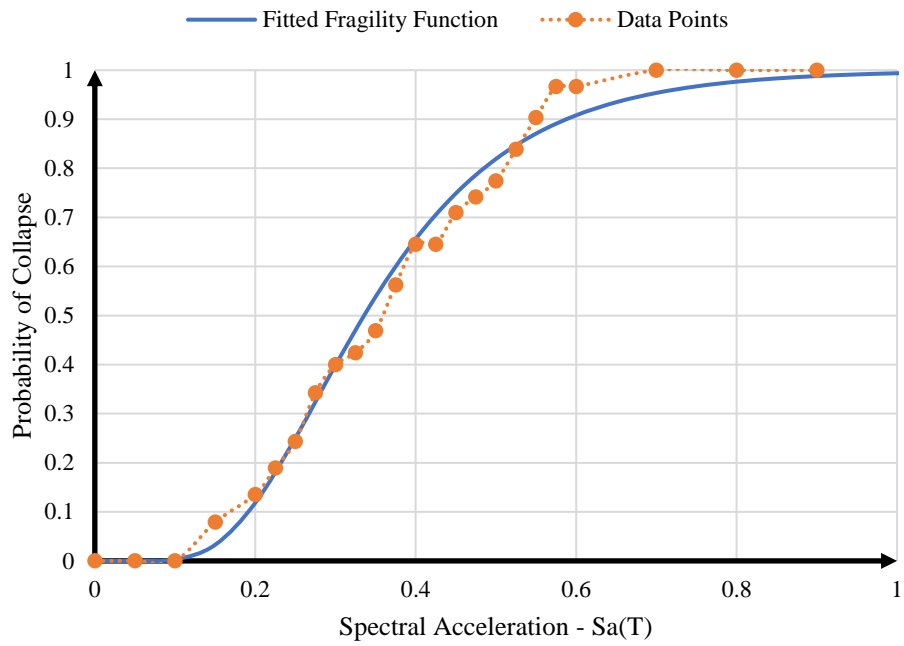


Figure 46: Empirical and fitted fragility function for the 8-story exterior frame

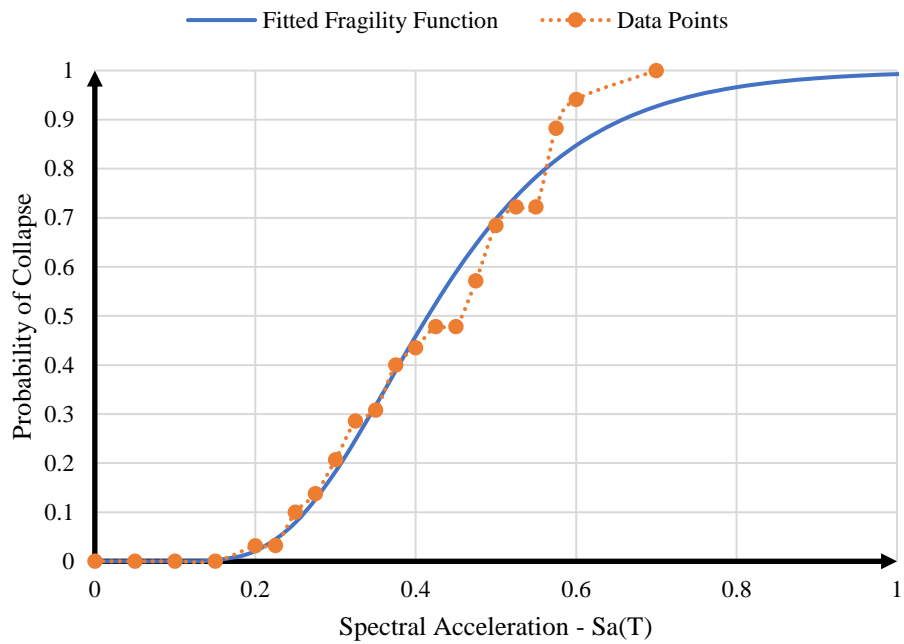


Figure 47: Empirical and fitted fragility function for the 8-story interior frame

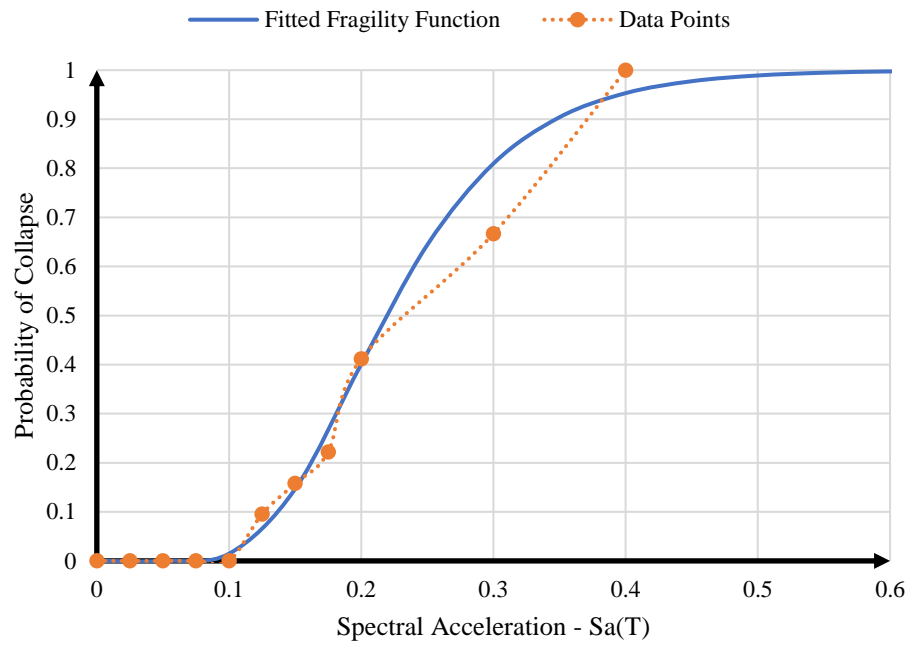


Figure 48: Empirical and fitted fragility function for the 12-story building